

The Pennsylvania State University
The Graduate School
Department of Engineering Science and Mechanics

**PREPARATION, CHARACTERIZATION AND POST-DEPOSITION MODIFICATION
OF PULSED-DC MAGNETRON SPUTTERED VANADIUM OXIDE THIN FILMS
FOR MICROBOLOMETER APPLICATIONS**

A Dissertation in
Engineering Science and Mechanics
by
Chandrasekaran Venkatasubramanian

© 2010 Chandrasekaran Venkatasubramanian

Submitted in Partial Fulfillment
of the Requirements
for the Degree of

Doctor of Philosophy

December 2010

The thesis of Chandrasekaran Venkatasubramanian was reviewed and approved* by the following:

S. Ashok
Professor of Engineering Science
Dissertation Co-Advisor
Co-Chair of Committee

Mark W. Horn
Associate Professor of Engineering Science and Mechanics
Dissertation Co-Advisor
Co-Chair of Committee

Michael T. Lanagan
Professor of Engineering Science and Mechanics

Thomas N. Jackson
Robert E. Kirby Chair Professor of Electrical Engineering

Judith A. Todd
P. B. Breneman Department Head
Head of the Department of Engineering Science and Mechanics

*Signatures are on file in the Graduate School

ABSTRACT

Vanadium Oxide (VO_x) thin films have been at the heart of uncooled microbolometers for several years, however very little is known about their structure and material properties. Also, process control remains an issue because the films are formed under oxygen-starved conditions resulting in films with “x” less than 2.0 in VO_x . Hence it is desirable to optimize the film deposition conditions so as to obtain the required properties (high temperature coefficient of resistance [TCR], low resistivity and low noise) for the microbolometer application. In this work, the parameter space for pulsed-dc magnetron sputtering was explored to arrive at optimum deposition conditions. A metallic vanadium target was used in a reactive environment under different Ar/O_2 ratios. The gas flow rates and oxygen partial pressures were varied systematically, and the corresponding changes in the cathode (target) current were monitored. The cathode current was found to exhibit a hysteresis behavior between forward and reverse directions for changes in the oxygen percentage as well as the total flow rate. The width and position of the hysteresis curve depended on the relative values of the gas flow rates and the oxygen partial pressures. Films were deposited along various points in the hysteresis curve, and their structural and electrical properties were evaluated. The resistivity and the TCR of the films were also found to exhibit a hysteretic behavior similar to that of the cathode current. The film microstructure changed from columnar at low flow rates to multi-grained features at higher flow rates. Also, the TCR of the films exhibited a linear relation with log of resistivity – the higher the resistivity, the higher the TCR.

The current read-out circuitry for VO_x microbolometer arrays requires a material with high TCR but low resistivity. Post-deposition modification was investigated to see if the combination of resistivity and TCR could be improved from the as-deposited properties. The sputtered films were annealed in inert (nitrogen) and oxidizing (oxygen) atmospheres at four

different temperatures for varying time periods. Depending on the exact annealing conditions, several orders of magnitude change in resistance and significant variations in TCR were observed. Optimal results were obtained for 300 °C anneal in nitrogen atmosphere. Ion implantation was also tried out to further enhance the trade-off between resistivity and TCR. Two species - Hydrogen (active) and Helium (inert) were implanted, which caused both the TCR and resistivity to go up. Subsequent anneal in nitrogen dropped the resistivity significantly, without changing the TCR much. This resulted in up to 40% improvement in TCR, for any given resistivity, as compared to the as-deposited films. In summary, magnetron sputtering, in combination with post-deposition process, can produce VO_x thin films comparable to or better than those used by industry. In addition, cathode current during deposition is a helpful processing metric to produce low resistivity, high TCR films.

TABLE OF CONTENTS

List of Figures	vii
List of Tables	xi
Acknowledgement	xii
 Chapter 1 Introduction	 1
1.1 Infrared Detectors	2
1.1.1 Photon Detectors	2
1.1.2 Thermal detectors	4
1.1.2.1 Microbolometers	4
1.2 Summary of Literature on VO _x Microbolometer Materials	7
1.3 Thesis Outline	14
 Chapter 2 Experimental Procedure	 16
2.1. Sputtering	16
2.1.1 Deposition system	19
2.1.2 Film deposition procedure	21
2.2 Annealing	22
2.3 Ion Implantation	23
2.4 Electrical Characterization	25
2.5 Profilometry	27
2.6 X-ray Diffraction	27
2.7 Scanning Electron Microscopy	28
2.8 Atomic Force Microscopy	28
2.9 Raman Spectroscopy	29
 Chapter 3 Pulsed-dc sputtering of vanadium oxide	 30
3.1 Process hysteresis characteristics:	30
3.2 Structural Properties:	35
3.3 Electrical Characterization:	42
3.4 Application of the Meyer-Neldel Rule:	46
3.5 Summary	50
 Chapter 4 Post-deposition processing: Annealing	 54
4.1 Oxygen Annealing	54
4.1.1 Electrical Properties	54
4.1.2 Structural Properties	57
4.2 Nitrogen Annealing	64
4.2.1 Electrical Properties	64
4.2.2 Structural Properties	66
4.3 Low-Temperature I-V characteristics	79

4.4 Theoretical model.....	83
4.5 Summary	85
Chapter 5 Post-deposition processing: Ion Implantation	88
5.1 Results and Discussion.....	89
Chapter 6 Conclusion.....	103
Future work	105
REFERENCES	109

LIST OF FIGURES

Figure 1-1: Electromagnetic radiation spectra from a black body at different temperatures...	1
Figure 1-2: A single pixel from a microbolometer array [].	5
Figure 1-3: Phase diagram of vanadium-oxygen system []	8
Figure 2-1: Various waveforms used for sputtering.	18
Figure 2-2: Kurt J. Lesker CMS-18 Sputtering system.	19
Figure 2-3: Schematic representation of the sputtering chamber.....	20
Figure 2-4: Pulse profile used for depositing VO _x films.....	21
Figure 2-5: Picture of the tube furnace used for annealing experiments.	23
Figure 2-6: TRIM ion ranges for H ⁺ implanted into 200 nm VO ₂ film on Si substrate with an energy of 10 keV.	24
Figure 2-7: Schematic of the strip electrodes used for resistance measurements.	26
Figure 2-8: Typical current-voltage curves obtained for VO _x thin films at different temperatures.	26
Figure 2-9: Graph showing calculation of TCR.....	27
Figure 3-1: Variation of cathode current as a function of (a) oxygen percentage (b) total oxygen flow in the chamber.....	32
Figure 3-2: Variation of cathode current as a function of (a) total gas flow (b) total oxygen flow in the chamber.....	34
Figure 3-3: Deposition rate as a function of total gas flow rate at 5% O ₂	36
Figure 3-4: X-ray diffraction patterns of films deposited at (a) 5% O ₂ and different flow rates (b) 18sccm flow and different oxygen percentages.	37
Figure 3-5: Cross-sectional FESEM images of samples deposited with 5% O ₂ at different flow rates - (a) 31 sccm (b) 65 sccm (c) 90 sccm.	38
Figure 3-6: Cross-sectional FESEM images of samples deposited at 18 sccm flow with different oxygen percentages - (a) 5% (b) 12% (c) 15%.....	39
Figure 3-7: Raman spectra of samples deposited at a constant flow rate of 18 sccm in the (a) forward and (b) reverse legs of the hysteresis curve shown in Fig. 3-1. Features denoted by the * are artifacts due to the subtraction of a Si reference spectrum.	40

Figure 3-8: Raman spectra of samples deposited at a constant oxygen percentage of 5% along the (a) forward and (b) reverse parts of the hysteresis curve shown in Fig. 3-2)...	41
Figure 3-9: Resistivity of the films as a function of O ₂ % and total flow rate.....	43
Figure 3-10: TCR of the films as a function of O ₂ % and total flow rate.	44
Figure 3-11: Dependence of resistivity on cathode current.	46
Figure 3-12: Schematic of density of states in mobility gap of an amorphous semiconductor.	48
Figure 3-13: Meyer- Neldel relation for samples deposited at [a] fixed oxygen percentage (5%); [b] fixed total flow rate (18 sccm).	49
Figure 3-14: Relationship between TCR and resistivity of as-deposited films.....	51
Figure 3-15: Plot of resistivity as a function of 1/T.....	52
Figure 3-16: Comparison of TCR and resistivity of pulsed dc magnetron sputtered films to data published by Wood [6] and Radford [10].....	53
Figure 4-1: Resistivity and TCR values as a function of annealing temperature for films annealed in oxygen atmosphere. The resistivity drops for the 200 and 300 °C anneals, but starts to increase after the 400 and 500 °C anneals. The data points corresponding to 400 °C anneal of the 7.5% sample are not clearly visible as they overlap with the 500 °C ones.	56
Figure 4-2: Comparison of the TCR of oxygen annealed films with as-deposited films.....	57
Figure 4-3: XRD spectra of the samples deposited at 5% and 7.5% O ₂ and annealed in oxygen ambient. Peaks corresponding to higher oxides of vanadium become prominent for the 400 and 500 °C anneals.....	58
Figure 4-4: Cross-sectional FESEM images of the film deposited at 5% O ₂ after annealing for 30 min at various temperatures in oxygen atmosphere. We can clearly see the plate-like structure of V ₂ O ₅ formed after annealing at 400 and 500 °C.....	59
Figure 4-5: AFM images of samples annealed in oxygen at the indicated temperatures.....	60
Figure 4-6: Raman spectra of 5% and 7.5% O ₂ deposited films as a function of annealing temperature in an oxygen atmosphere. Note the drastic change in the spectra beginning at 300 °C, correlating with the observed drop in resistivity.....	62
Figure 4-7: Summary of changes in electrical properties as a result of annealing in oxygen at various temperatures.....	63
Figure 4-8: Resistivity and TCR values as a function of annealing temperature for films annealed in a nitrogen atmosphere. The film resistivity decreased monotonically with increasing annealing temperatures, but the TCR still remained reasonably high.	65

Figure 4-9: Summary of resistivity vs TCR for nitrogen annealed samples.....	66
Figure 4-10: X-ray diffraction spectra of films annealed in nitrogen.	67
Figure 4-11: Cross-sectional SEM images of the sample deposited at 5% O ₂ and annealed in nitrogen atmosphere.....	68
Figure 4-12: AFM images of the sample deposited at 5% O ₂ and annealed in nitrogen atmosphere at the indicated temperatures.	69
Figure 4-13: Raman spectra of 5% and 7.5% O ₂ films as a function of annealing temperature in a nitrogen atmosphere. The as-deposited, 200 °C, and 300 °C samples exhibit broad amorphous VO _x features. At 400 °C, the spectrum develops sharper feature characteristics of crystalline VO ₂	70
Figure 4-14: Selected area diffraction pattern of the film deposited at 5 mT pressure, 5% O ₂ and annealed in nitrogen at 300 °C.	72
Figure 4-15: Comparison of the selected area diffraction pattern of the as-deposited film and the film annealed at 300 °C.	73
Figure 4-16: Dark-field image of the annealed sample showing micro-twins.	74
Figure 4-17: Comparison of the dark-field images of as-deposited and annealed sample.	75
Figure 4-18: Comparison of EELS of the 5% O ₂ sample before and after annealing in nitrogen at 300 °C.....	76
Figure 4-19: Comparison of EELS of amorphous and nano-crystalline regions. The relative positions of the O K edge indicates that the amorphous phase is richer in oxygen than the nano-crystalline phase.	77
Figure 4-20: Variation of resistivity as a function of temperature for three samples deposited at 5, 7.5 and 10% oxygen at a flow rate of 18 sccm.	80
Figure 4-21: Plot of log dE versus log T between T _c and 30 K.	81
Figure 4-22: Resistivity versus temperature behavior of annealed samples.	82
Figure 4-23: Resistivity of annealed samples as a function of (1/T) ^{1/2}	83
Figure 4-24: Proposed structure model for vanadium oxide thin films.	84
Figure 4-25: Comparison of TCR and resistivity values for annealed and as-sputtered films. Clearly the annealed films have a better TCR at any given resistivity.	85
Figure 4-26: Comparison of TCR and resistivity of VO _x films before and after annealing in nitrogen for 30 min.	86
Figure 4-27: Comparison of TCR and resistivity of annealed samples to published results. ..	87

Figure 5-1: Target displacements due to implantation of H^+ in VO_x	89
Figure 5-2: Effect of implantation on the TCR and resistivity of VO_x films deposited under different conditions. Both the TCR and resistivity of the films go up after implantation.	91
Figure 5-3: Resistivity and TCR values as a function of annealing temperature for a film deposited at 5 mTorr pressure and 5% O_2 and implanted with (a) $H^+ 10^{13}$ atoms/cm ² (b) $H^+ 10^{15}$ atoms/cm ² (c) $He^+ 10^{14}$ atoms/cm ² and (d) $He^+ 10^{15}$ atoms/cm ²	94
Figure 5-4: Comparison of X-ray diffraction spectra of samples as deposited, after implantation and after annealing in nitrogen.....	95
Figure 5-5: Cross-sectional SEM images of the (a) after implantation, (b) after implant + anneal at 200 °C, and (c) after implant + anneal at 300 °C.	96
Figure 5-6: Variation of resistivity and TCR of a sample deposited with 5% O_2 at 200 °C after implantation with H^+/He^+ and annealing at various temperatures.	97
Figure 5-7: Variation of resistivity and TCR of a sample deposited at 7.5% O_2 after implantation with H^+/He^+ and annealing at various temperatures. We can clearly see the difference in behavior between the H^+ and He^+ implanted samples after the 300 °C anneal.	99
Figure 5-8: Variation of resistivity and TCR of a sample deposited at 15% O_2 after implantation with H^+/He^+ and annealing at various temperatures. Here again the difference in behavior between the H^+ and He^+ implanted samples after 300 °C anneal is observed.	100
Figure 5-9: XRD spectra of sample deposited at 7.5% after implantation with H^+/He^+ and after subsequent annealing. No significant difference between the H^+ and He^+ implanted samples.....	101
Figure 5-10: TCR values as a function of resistivity for the as-sputtered films, annealed films and the implanted/annealed films.	102
Figure 5-11: Comparison of TCR and resistivity of implanted and annealed samples with the industrial ion beam samples.	102

LIST OF TABLES

Table 1-1: Transition temperatures of various vanadium oxide Magneli phases.	9
Table 4-1: Comparison of RBS data of the 5% O ₂ as-deposited sample and the 300 °C annealed sample.	78

ACKNOWLEDGEMENTS

I would like to take this opportunity to thank several people who have helped me through the course of my Ph.D. First and foremost, I express my sincere gratitude to my advisors Dr. S. Ashok and Dr. Mark W. Horn for their invaluable guidance, support and encouragement, that helped me achieve this goal. I would also like to thank my committee members, Dr. Thomas Jackson and Dr. Michael T. Lanagan for their valuable inputs and suggestions.

Thanks also extended to Dr. S. S. N. Bharadwaja for assistance with data analysis, Dr. Orlando M. Cabarcos for help with obtaining and analyzing Raman results, Sean Pursel for the great cross-sectional FESEM images, and Dr. Jing Li for TEM analysis. I am also thankful to the other group members, Nick Fieldhouse, Kerry Wells, Bryan Gauntt, Hitesh Basantani, Myung-Yoon Lee, Mike Motyka, and Dr. Nik Podraza for their assistance during various experimental works.

The support extended by my family and friends deserves a special mention. Their motivation and encouragement helped me remain in the highest of spirits at all times and successfully complete this program,

Research was sponsored by the U.S. Army Research Office and U.S. Army Research Laboratory and was accomplished under Cooperative Agreement Number W911NF-0-2-0026.

Chapter 1

Introduction

There are many ways by which a person can see in the dark. Most low cost systems rely on low-light image intensifiers in the visible range. However, infrared (IR) cameras help us to see in the dark, things that are not visible to the naked eye or conventional low-light cameras. All hot objects are known to emit radiation, and Plank's law describes quantitatively the temperature-dependent emission spectrum of an idealized object, viz., a black body. Fig. 1-1 shows the typical spectrum of black body radiation. It can be seen that the wavelength of the radiation emitted by objects around room temperature lies outside the visible range (0.4 to 0.7 μm), and hence they cannot be seen without the aid of external light. IR imaging devices, on the other hand, make use of this IR radiation (3 – 5 μm and 8 – 14 μm) to form images.

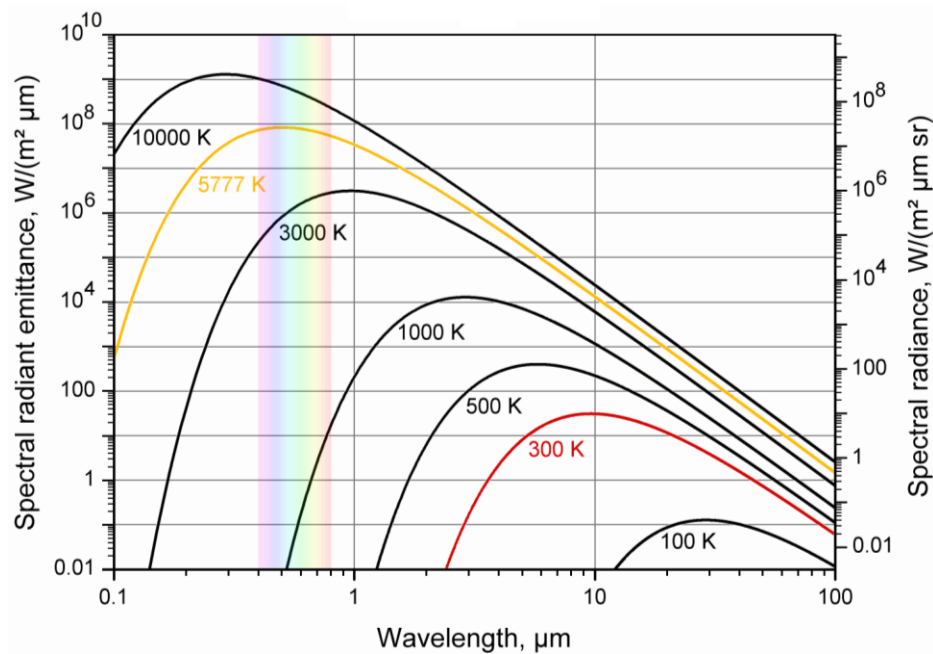


Figure 1-1: Electromagnetic radiation spectra from a black body at different temperatures
[Source: <http://cosmictimes.gsfc.nasa.gov/teachers/guide/1965/guide/murmur.html>].

Interest in night vision cameras began around the Second World War to track anti-air-missile seekers. Then during the Vietnam War, the United States military services initiated the development of IR systems that could provide imagery arising from thermal emission of terrain vehicles, buildings, and people [1]. As the technology began to develop over the next few decades, commercial interest also grew. Currently such devices are of great importance not only for the military, but also for space applications, search and rescue missions, and even heat leakage monitoring. These devices are also being used as a driving aid during night and foggy conditions, for security surveillance, and for biomedical applications including detection of tumors and analysis of blood flow [1, 2].

1.1 Infrared Detectors

An infrared detector is a device capable of converting the incident invisible electromagnetic radiation signal into an electrical signal that in turn can be used to form an image. Based on their mechanisms of operation, infrared detectors can be broadly classified into two types: Photon detectors and thermal detectors [3, 4]. In photon detectors, the incident radiation is absorbed by the material through direct interaction with the electrons while thermal detectors make use of the heat associated with the radiation. Another major difference is that IR photon detectors need to be cooled down to cryogenic temperatures in order to get good sensitivity whereas thermal detectors can operate uncooled at room temperature.

1.1.1 Photon Detectors

In photon detectors, the incoming photons interact with the electrons of the material and causes changes to the electronic energy distribution. This leads to changes in the electrical

signal-output which is detected and used to form the image [4]. Depending on the nature of interaction, photon detectors can be sub-classified further into four types – intrinsic detectors, extrinsic detectors, photodiode detectors, and quantum well detectors [3]. In an intrinsic detector, if the incident photon energy is greater than the band gap of the material, it generates an electron-hole pair, which changes the conductivity of the material. In an extrinsic detector, the photon excites either an electron or a hole from their respective donor/acceptor energy levels, again resulting in a change in the electrical conductivity. In a photodiode detector, a p-n junction or a Schottky barrier (a rectifying metal-semiconductor contact) is used. If the energy of the incident photon is greater than the bandgap of the semiconductor or the Schottky barrier height, it will cause the photo-excited electrons to jump over the barrier and contribute to a photocurrent. In quantum well detectors, the energy threshold for detection is controlled by the physical dimensions of a semiconductor heterostructure. In all these cases, the fundamental requirement is that the energy of the incident photon should be greater than the forbidden energy gap / ionization energy / Schottky barrier height. For infrared radiation in the 8 – 14 μm range, this energy comes out to be 0.09 eV. This gap is small, leading to a large number of thermally excited carriers at room temperature. This makes it practically impossible to detect the photo-excited carriers; these detectors must be cooled down to cryogenic temperatures to reduce the thermal generation – recombination noise and be able to detect the photon-induced changes [1- 4]. This leads to an increase in their manufacturing and operating costs. But once cooled down to cryogenic temperatures, they can have excellent signal-to-noise performance and very fast response. Hence they are mainly used in places where high performance is required and cost is not a big issue.

1.1.2 Thermal detectors

Thermal detectors, unlike photodetectors, operate by sensing the change in temperature caused by the incident radiation. The change in temperature causes a change in some measureable property of the material, which is monitored and correlated back to form the image. The most commonly used thermal detectors are the resistive bolometer, the pyroelectric detector and the thermopile. A microbolometer changes its resistance, a pyroelectric material exhibits electrical polarization, while a thermopile generates a voltage across its junction. The main advantage of thermal detectors is that they can operate at room temperature without any cryogenic cooling. Additionally, they can function over a wide spectral range.

A resistive bolometer changes its electrical resistance as its temperature rises due to the absorption of electromagnetic radiation. The detector material can either be a metal or a semiconductor. A metal bolometer has a positive temperature coefficient of resistance of about $0.3 - 0.4 \% K^{-1}$ while a thermistor bolometer has a negative temperature coefficient of up to $-4 \% K^{-1}$. Metals commonly used as detectors include nickel and platinum. Typical thermistor materials are α -Si, Si-Ge and oxides of metals such as nickel, manganese, cobalt and vanadium [5].

1.1.2.1 Microbolometers

Early bolometers elements were very large in size ($\geq 1 \text{ mm}$) and hence impractical for use in two-dimensional arrays with a large number of sensors. In the 1980s, Honeywell came up with a prototype sensor consisting of mechanical bridge-like structures, $\sim 100 \mu\text{m}$ square and $1 \mu\text{m}$ thick, known as the microbolometer. Several of these microbolometers were constructed as a

two-dimensional focal plane array to realize the first uncooled IR-camera. Each pixel of the array contains a single microbolometer.

Fig. 1-2 shows the basic bridge structure of the microbolometer fabricated by Honeywell. The thermally sensitive detector material is encapsulated in the $0.5\ \mu\text{m}$ thick Si_3N_4 bridge suspended above the underlying silicon substrate. A thin-film metal reflector layer is deposited on the underlying substrate to reflect any unabsorbed radiation back to the detector. The vacuum gap is adjusted so as to produce a quarter wave resonant cavity between the substrate and the bridge in order to maximize absorption of the incoming infrared radiation. The bridge is supported by two narrow legs of Si_3N_4 which provide excellent thermal isolation. A $\sim 500\ \text{\AA}$ thick Ni-Cr conductive film is encapsulated within the silicon nitride legs in order to provide electrical connection between the microbolometer and the read out integrated circuitry (ROIC).

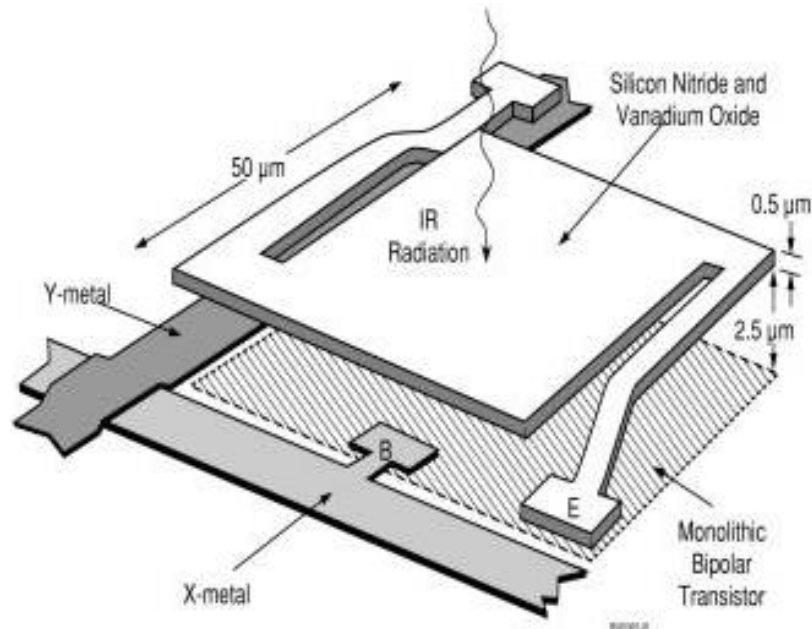


Figure 1-2: A single pixel from a microbolometer array [6].

The principal figure of merit for an uncooled microbolometer is noise equivalent temperature difference (NETD). It is a measure of the smallest temperature difference detectable by a bolometer and is given by [3]

$$NETD = \frac{4F^2 V_N}{\tau_o A_D \mathcal{R} (\Delta P / \Delta T)_{\lambda_1 - \lambda_2}} \quad (1.1)$$

where $F = 1/(2\sin\theta)$, θ is the angle which the marginal ray from the optics makes with the optical axis at the focal point of the image, V_N is the total noise voltage over the array readout electrical bandwidth, τ_o is the transmittance of the optics, A_D is the area of the pixel, \mathcal{R} is the responsivity, and $\left(\frac{\Delta P}{\Delta T}\right)_{\lambda_1 - \lambda_2}$ is the change with respect to temperature of the power per unit area emitted by a blackbody at temperature T measured within the spectral bandwidth between λ_1 and λ_2 .

We can see that the only material parameters that can be tailored easily are responsivity (\mathcal{R}) and noise (V_N). For optimal bolometer performance, we want the NETD to be as small as possible. For this, we need to have low noise and high responsivity. Responsivity is defined as the ratio of the electrical signal output to the incident power and is given by [3]

$$\mathcal{R} = \frac{\beta \eta i_b \alpha R}{G \sqrt{1 + \omega^2 \tau_T^2}} \quad (1.2)$$

where α is TCR, β is fill factor, η is absorptance, i_b is bias current, R is resistance, G is thermal conductance of the suspended structure, ω is the angular modulation frequency of the incident radiation, and τ_T is the thermal response time of the bolometer. For high responsivity, the material must have high TCR and a high resistivity. But the resistivity is limited by other operating parameters of the read out circuitry such as the power and bias currents.

Noise refers to any fluctuations in the output signal that are not caused by the image source. There are four sources of noise in bolometers: Johnson noise, 1/f power law noise, temperature fluctuation noise, and background fluctuation noise. Johnson noise ($V_{N,J}$) arises due

to the random thermal motion of free electrons in a resistor while $1/f$ noise ($V_{N, 1/f}$) is due to trapping/detrapping of charge carriers in states far off from the Fermi level, and is frequency dependent. The statistical nature of the heat interchange between the detector material and its surroundings gives rise to the temperature fluctuation noise ($V_{N, TF}$) and the background fluctuation noise ($V_{N, BF}$) is caused by fluctuations in the absorbed power due to the quasi-random arrival of the photons. Since all these noises are uncorrelated, the total noise is given by the square root of the sum of the squares of these four noises [3].

$$\overline{V_{N,Tot}^2} = \overline{V_{N,J}^2} + \overline{V_{N,1/f}^2} + \overline{V_{N,TF}^2} + \overline{V_{N,BF}^2} \quad (1.3)$$

Temperature fluctuation noise and background fluctuation noise are inherent properties of the microbolometer and are independent of the sensor material. Hence Johnson noise and $1/f$ noise are the only ones of interest from the materials stand point. At low frequencies, the $1/f$ noise dominates while at higher frequencies it falls below the Johnson noise limit [3].

Hence for optimal performance of the microbolometer, we need to have a material with a high TCR, low resistivity and low $1/f$ noise.

1.2 Summary of Literature on VO_x Microbolometer Materials

The prominent materials currently used as the active temperature sensing layer in microbolometers are vanadium oxide [7], amorphous silicon [8] and polycrystalline SiGe [9]. Among these, the preferred commercial choice is vanadium oxide (VO_x with $x \sim 1.8$) which has a relatively high TCR and reasonably low resistivity [10]. Other advantages include low temperature processing and compatibility with the current CMOS fabrication technology. Although VO_x films meet most of the necessary criteria for use in this application, little is understood about their structure, role of defects or conduction mechanisms. Despite this lack of fundamental understanding, the entire MEMS device has been engineered to high levels of

sophistication. With a better understanding of the underlying conduction, one could strive for systematic improvement in TCR or stability in combination with low 1/f noise, and thus greatly enhance the commercial impact.

Vanadium is a metal with variable valences, including +2, +3, +4 and +5, and hence forming a large number of oxides such as VO, V₂O₃, VO₂ and V₂O₅ [11]. In addition, it also forms the so called Magneli phases, defined by the general stoichiometric formula [12]

$$V_nO_{2n-1} = V_2O_3 + (n-2)VO_2 \quad (1.4)$$

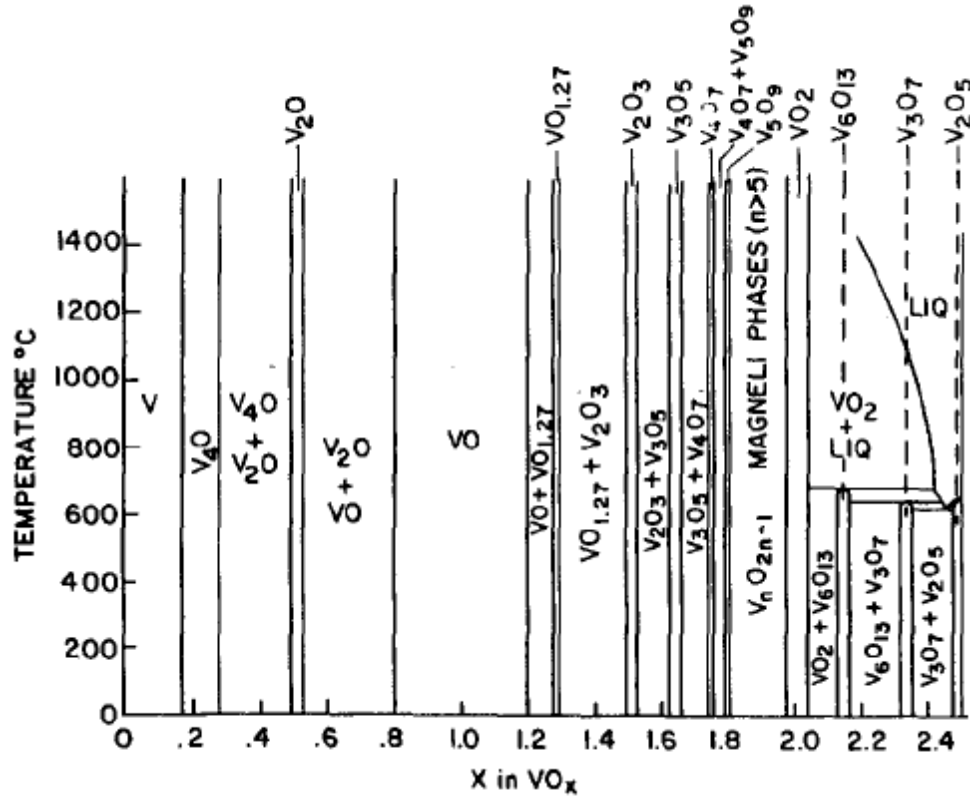


Figure 1-3: Phase diagram of vanadium-oxygen system [13]

These Magneli phases take an intermediary position between V₂O₃ and VO₂ and exist with a mixture of +3 and +4 valence states. They exhibit closely related crystal structures and

have very narrow stability ranges as seen in the VO_x phase diagram in Fig. 1-3. Hence fabricating vanadium oxide thin films with a single stable phase is extremely difficult.

Also, many of these vanadium oxide phases exhibit metal-insulator transitions (MIT) at certain temperatures, whereby they change from one crystal structure to another, resulting in drastic changes in resistivity. For example, VO_2 undergoes a transition from a semiconductor with monoclinic symmetric structure to a metal with a tetragonal rutile structure at 67°C , resulting in a resistance change of over four orders of magnitude [14, 15]. In addition, this change also exhibits a hysteresis behavior, making it very difficult to use in microbolometers [16]. Some of the other phases of vanadium oxide undergo this change outside our temperature of interest and hence could be made use of. Table 1-1 below lists the transition temperatures for the different Magneli phases [12].

Table 1-1: Transition temperatures of various vanadium oxide Magneli phases.

Compound $\text{V}_n\text{O}_{2n-1}$	Formal V 3d charge	MIT Temperature (K)
V_2O_3	2	168
V_3O_5	$5/3 \approx 1.67$	430
V_4O_7	$6/4 \approx 2$	250
V_5O_9	$7/5 \approx 1.4$	135
V_6O_{11}	$8/6 \approx 1.33$	170
V_7O_{13}	$9/7 \approx 1.29$	Metallic
V_8O_{15}	$10/8 \approx 1.25$	70
V_9O_{17}	$11/9 \approx 1.22$	-
VO_2	1	340

Taking these features into account, several different phases of vanadium oxide have been used for microbolometer application. Even VO_2 , in spite of the hysteresis behavior, has been shown to be a feasible material, provided appropriate models are incorporated into the data processing steps to account for this transition [16, 17].

Researchers started studying the properties of the different phases of vanadium oxide as early as 1972. Banus et al determined the lattice parameters and densities of polycrystalline VO_x samples as a function 'x'. They also measured the resistivities and the activation energies, along with other properties such as Seebeck coefficient and magnetic susceptibility [18]. Based on this, and other references, Goodenough proposed a density of states model for different 'x' values based on the cation – cation separation distance, and explained the transformation in the conduction mechanism as x changes from below 1 to above 1 [19].

Several techniques have been used to fabricate vanadium oxide thin films. These include dc magnetron sputtering [20, 21, 22, 23], rf sputtering [13, 24, 25, 26, 27], ion beam sputtering [28, 29, 30], e-beam evaporation [31], molecular beam epitaxy [32], sol-gel processing [33] and pulsed laser techniques [34].

Fuls et al of Bell Laboratories were the first ones to report on the deposition of vanadium oxide thin films, in 1967. They used dc reactive sputtering in an argon-oxygen gas mixture with a substrate temperature of 400 °C. X-ray and electron diffraction confirmed the presence of polycrystalline VO_2 with a grain size of over 100 Å [20]. This work was followed by Rozgonyi and Hensler who studied the interrelation between the substrate material, film structure and electrical performance. It was found that films deposited on amorphous substrates such as glass and glazed ceramic were polycrystalline with small grains. Sapphire substrates produced highly textured films while films on rutile substrates were epitaxial. But still, in all substrates, the conductivity ratio between the semi-conductor and metallic phases were almost the same [21].

Kusano et al later investigated different substrate temperatures and oxygen partial pressures under which various vanadium oxide phases such as V_2O_5 , V_3O_7 , V_4O_9 and V_6O_{13} grow [22].

Griffiths and Eastwood examined the effects of oxygen partial pressure and substrate temperature on the stoichiometry and structure of rf sputtered vanadium oxide films. They observed that while vanadium and VO phases were crystalline at all substrate temperatures, the higher oxide phases were amorphous at lower temperatures. Also, the VO lattice was able to accommodate a wide range of stoichiometry over $VO_{0.8} - VO_{1.2}$, and the lattice spacing increased with increase in the oxygen content [13]. Benmoussa et al deposited polycrystalline vanadium pentoxide films by rf sputtering from a V_2O_5 target in a gas mixture of argon and oxygen. The deposited films were polycrystalline and had planar spacing greater than that of bulk V_2O_5 . Also that planar spacing increased with increasing O_2 content of the sputtering gas [25]. When Lourenco et al did a similar study sputtering from a metallic vanadium target, they found that the films were either amorphous or small grained (< 5 nm). There were also considerable amounts of hydrogen present in the films, and the oxidation state of vanadium varied between that of V_6O_{13} and V_2O_5 , as measured by Rutherford backscattering spectrometry (RBS) and forward recoil spectrometry (FRS) [26].

In 1985, Chain deposited vanadium oxide thin films by ion-beam sputtering, and found that there was a strong correlation between the substrate temperature and the film microstructure. Films deposited below 435°C appeared with a dense array of poorly defined grains with size of $0.1 - 0.3\ \mu\text{m}$, and XRD results indicated the presence of the VO_2 phase admixed with another phase identified as $VO_{1.27}$. At temperatures between 505°C and 570°C , the deposited films consisted mainly of oriented, columnar grains of VO_2 , $0.3 - 1\ \mu\text{m}$ in size. At substrate temperatures above 585°C , the films consisted of large, well-defined grains ($1 - 2\ \mu\text{m}$) of VO_2 [28]. These results were consistent with Thornton's structure zone model [35]. In another series of experiments, Chain observed that as the oxygen fraction of the sputtering gas is increased, the

crystallography evolves from a FCC vanadium oxide to a mixed oxide phase containing VO_2 in which there is a degree of preferential grain orientation. Further increase in oxygen content above 25% leads to a mixed oxide phase containing V_2O_5 with a structure of long, randomly oriented grains [29].

Though a lot of work has been reported on the fabrication and general properties of the different vanadium oxides, the literature on the use of vanadium oxide in bolometers has been limited due to the early classification of the material by the US Army. The first literature published on using vanadium oxide as the bolometer material was in 1988 by Wood et al at Honeywell Inc. [36]. Wood and Stelzer later revealed that 500 Å thick mixed vanadium oxide (VO_x) films had no phase transitions near room temperature but still had a TCR of up to $-3\% \text{K}^{-1}$ [37, 6]. In 1993, Jerominek et al [38] showed that dc sputtered stoichiometric V_2O_5 films exhibited a TCR of up to 4% and hence could be used for bolometric applications.

Chung et al obtained polycrystalline V_2O_5 by room temperature d.c. reactive sputtering followed by 400 °C thermal anneal. The as-deposited film had a resistance of 95 $\text{k}\Omega$ with a TCR of $-1.8\% \text{K}^{-1}$, which after annealing became 703 $\text{k}\Omega$ with a TCR of $-2.4\% \text{K}^{-1}$ [39]. Yong Hee Han et al used alternative layers of V_2O_5 and V and subsequently annealed it in oxygen to get a mixed phase with resistivity of 0.1 ohm-cm and TCR of over $-2\% \text{K}^{-1}$ [40]. Chen et al deposited vanadium oxide on SiO_2 buffer layers by dc magnetron sputtering. The films exhibited a lamellar structure with the size of the lamellas ranging from 60 to 300 nm. XRD revealed that the film contained a mixture of VO_2 , V_2O_3 and V_6O_{13} phases [41]. Lv and co-workers deposited vanadium oxide films on glass substrates using facing dc targets. They obtained a film with high TCR and also high resistance. They followed it up with vacuum annealing to achieve a better trade-off. XPS studies revealed that V_2O_5 broke down into lower oxides of vanadium while AFM imaging showed that the grains became fine and compact. But the TCR and resistivity values they report ($-4.4\% \text{K}^{-1}$ at 20 $\text{k}\Omega/\text{square}$) seem to be inconsistent with the rest of the literature [42].

Wang et al. deposited polycrystalline VO_x thin films on to Si substrates by ion beam sputtering. The films had a sheet resistivity of $50 \text{ K}\Omega/\text{square}$ and XRD spectra indicated that they primarily consisted of V_2O_5 and VO_2 . But still they had a fairly linear log (resistivity) versus temperature relation with a TCR of -2.1 \%K^{-1} . The grains were found to be compact and ultra-fine ($\leq 50 \text{ nm}$) and the surface was very smooth. They tried to reduce the resistance by annealing in argon at $400 \text{ }^\circ\text{C}$, but the films deoxidized to VO_2 and the log (resistivity) versus temperature became non-linear, making them not suitable for bolometers [30].

Another group in China led by Wang et al. deposited vanadium oxide thin films on Si_3N_4 coated Si substrates by ion beam sputtering at $200 \text{ }^\circ\text{C}$. They found that the electrical properties of the deposited film had had a huge dependence on oxygen partial pressure and ion beam parameters. Their best film had a sheet resistance of $32 \text{ k}\Omega/\text{square}$ with a TCR of -2.5 \%K^{-1} [43].

A group in Netherlands reported on the structural and electrical properties of epitaxial VO_x films. They grew the films by molecular beam epitaxy on MgO substrates, which has a 3% lattice mismatch with respect to cubic rocksalt VO. They calculated the lattice constants of the deposited films from diffraction data and found the perpendicular lattice constant to decrease with x . They also measured resistivity and activation energy as a function of x in VO_x , and found that the values were higher than those for bulk samples, possibly because of the strain induced into the thin films. And at low temperatures, conductivity exhibited Mott's variable range hopping behavior for a wide range of x values [44, 32].

Rajendra Kumar et al. used pulsed laser deposition to deposit vanadium oxide films. By varying the laser power, they were able to deposit films with different structural and electrical properties. The optimal film for bolometer application was obtained using 1.4 J/cm^2 laser power and resulted in a TCR of -2.8 \%K^{-1} [34].

There was even an attempt made to add tungsten and form vanadium-tungsten oxide with improved properties. Y-H. Han et al. co-sputtered vanadium and tungsten metals by rf sputtering,

and then oxidized it at 300 °C in an oxygen ambient. The resultant V-W-O films had good properties for tungsten concentrations up to 10%. Best result was obtained for $V_{0.95}W_{0.05}O_x$ annealed for 90 min and it had a TCR of $-4.1\%K^{-1}$ [45].

Currently the most commonly used industrial technique is reactive ion-beam sputter deposition. But the rationale from the literature is not clear since this process generally is thought to have low deposition yields with respect to conventional sputtering and has more complex equipment requirements. Hence an alternative deposition technique, pulsed-dc reactive sputtering, which has been found to offer a high deposition rate for oxide thin films [46], was explored as a potential alternative for deposition of VO_x films. In 2006, Penn State was awarded a multidisciplinary university research initiative (MURI) sponsored by the Army Research Office (ARO) entitled, “Monolithic Silicon Microbolometer Materials for Uncooled Infrared Detectors”. Investigation of pulsed-dc magnetron sputtered vanadium oxide thin films started almost a year prior to this award. Since then, there have been several publications on VO_x discussing the film processing parameters, electrical properties, microstructure, and transport behavior [47, 48, 49, 50, 51, 52, 53, 54, 55, 56]. This thesis is an extension of the ongoing work at Penn State on vanadium oxide as the imaging layer in microbolometers used in uncooled infrared focal plane arrays.

1.3 Thesis Outline

This thesis explores the use of pulsed dc magnetron sputtering as a potential improvement over ion beam sputtering in the manufacturing of thin VO_x films for microbolometers. Several aspects of the process were examined.

- 1) Explore the parameter space of pulsed-dc reactive sputtering for VO_x films and optimize the conditions for the properties required by a microbolometer. Reactive sputtering in

general presents hurdles for reproducible processing. Industry currently uses material that has a very low resistivity. The deposition process for this type of material was evaluated and optimized with respect to target oxidation often associated with reactive sputtering from a metal target. Cathode current was monitored as a function of oxygen percentage and flow rate and film properties were correlated to this metric.

- 2) Once reproducible films were obtained, the focus of this thesis research was on post-deposition processing for optimization of the key microbolometer metrics.
 - i. Annealing – Annealing aids in redistribution of atoms, grain growth, and/or modification of film stoichiometry depending on the temperature and the ambient. Films were annealed in both oxygen (oxidizing) as well as nitrogen (inert) atmospheres at various temperatures, and the changes in the properties were evaluated.
 - ii. Ion Implantation – Ion implantation is an extensively used tool in the semiconductor industry for doping as well as passivation of defect states for controlling device properties. It can also cause amorphization of the film as well as introduce point and extended defects. Two species – hydrogen and helium – were chosen for implantation. Hydrogen is an active species well known for passivating defects in a wide variety of electronic materials. Helium (an inert species) was chosen mainly to distinguish between the effects arising from bombardment on the film and the passivating influence of hydrogen. The implanted films were also subsequently annealed in a nitrogen atmosphere to study the effects of redistribution of the implanted species and/or defects.

Chapter 2

Experimental Procedure

This chapter explains in detail the film deposition procedure for pulsed dc reactive sputtering of vanadium oxide thin films. It discusses the basics of the sputtering process and the reasons for choosing the pulsed dc waveform. It also details the post-deposition processing procedures and the various characterization techniques used for evaluating the electrical and structural properties of these thin films.

2.1. Sputtering

Sputtering is a physical vapor deposition process wherein atoms are ejected, or sputtered, from a solid target material by bombardment of inert or reactive energetic ions and subsequent momentum transfer, and deposited onto the substrate material to form a thin film. In conventional dc sputtering, a negative potential is applied to the target (cathode) while the substrate is held at neutral or ground potential. This potential difference creates an electric field which causes the electrons to accelerate and collide with the sputter gas molecules, leading to ionization. Usually, the sputter gas is argon, but is not limited to it. Other gases such as krypton, xenon, neon, helium and nitrogen can also be used. The ionized sputtering gas forms the plasma and is at a slightly higher potential than the rest of the chamber which is at ground potential (~10V). The electric field causes the positive ions to accelerate towards the target, bombard it and sputter off the target material. These sputtered atoms/ions move through the plasma and deposit on the substrate, creating a thin film.

This entire process will self-sustain as long as the target is an electrical conductor and chemically inactive in the plasma environment. However, if the target material to be sputtered is an insulator, accumulation of Ar^+ ions occurs on the target surface, and this will lead to repulsion of further incoming Ar^+ ions. As a result, the sputtering yield decreases and can cause arcing that can damage power supplies as well as film surface and/or microstructures. The common alternative in such cases is to use an rf source which provides alternative positive and negative voltages to the target at radio frequency (13.56 MHz). The positive half cycle expels the positive charge from the target surface, thereby presenting a neutral surface for the next negative half cycle. But unfortunately, rf sputtering is a very slow deposition rate process comparatively with high power losses and does not allow much control over the energy of the sputtered material.

Pulsed-DC sputtering can be seen as an intermediate between dc and rf sputtering, wherein a short positive or zero potential interspersed between longer negative pulses (in the KHz range) is applied to the target [57]. The pulse width and duration are sufficient to neutralize the positive charges on the target surface, but at the same time, the technique allows the target to have a longer exposure time at the negative voltage, during which the actual sputtering takes place. Its major advantage over rf is the flexibility it provides in modulating the relative pulse widths and frequency as per the sputtering requirements.

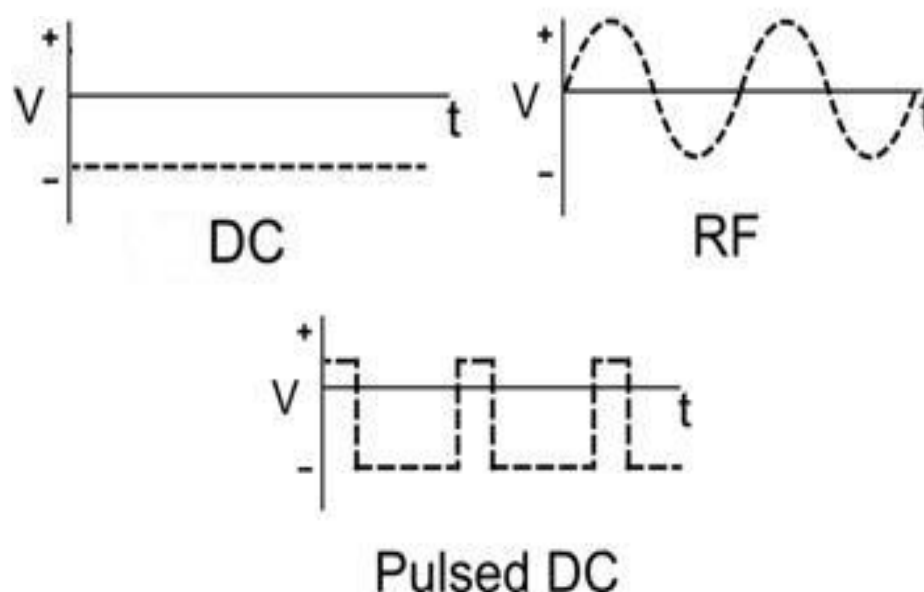


Figure 2-1: Various waveforms used for sputtering.

If a compound material thin film is desired, there are, in general, two methods available. The first is to directly sputter off a target made of the compound itself. But the disadvantage here is that the composition of the deposited film and the target material would essentially be the same, and hence film properties cannot be varied. The second method is called reactive sputtering. Here, a reactive gas is introduced into the chamber during deposition. Typically, the material sputtered off the target reacts with this gas in the plasma to form a compound, which then gets deposited on the substrate. Chemical reactions can also occur on the surface of the target, the chamber wall and on the substrate. The main advantage of this technique is that the composition of the sputtered film can be controlled by varying the flow rate of the reactive gas. Here again, if the target is capable of forming an insulating layer in the presence of the reactive gas (often referred to as “target poisoning”), a simple dc source would not work. An alternative source such as pulsed dc needs to be used.

2.1.1 Deposition system

Vanadium Oxide thin films were deposited by reactive pulsed-dc magnetron sputtering. The sputter tool used is a Kurt J. Lesker CMS-18 system consisting of a cylindrical 304 stainless steel chamber fitted with three TORRUS magnetron sputtering guns. The substrate stage can hold wafers up to 6" diameter and is capable of rotating at up to 10 rpm. A turbo-molecular pump, in conjunction with a mechanical pump can pump the system down to less than 10^{-6} Torr in under 2 hours. It also has a load lock chamber that facilitates the introduction of the sample into the main chamber without breaking vacuum. The sputter guns are powered by either an RFX600 rf generator or an MDX 1000 DC power supply coupled with a Sparkle 20 pulse generator. Gases flowing into the system are controlled by MKS mass flow controllers (mfcs).



Figure 2-2: Kurt J. Lesker CMS-18 Sputtering system.

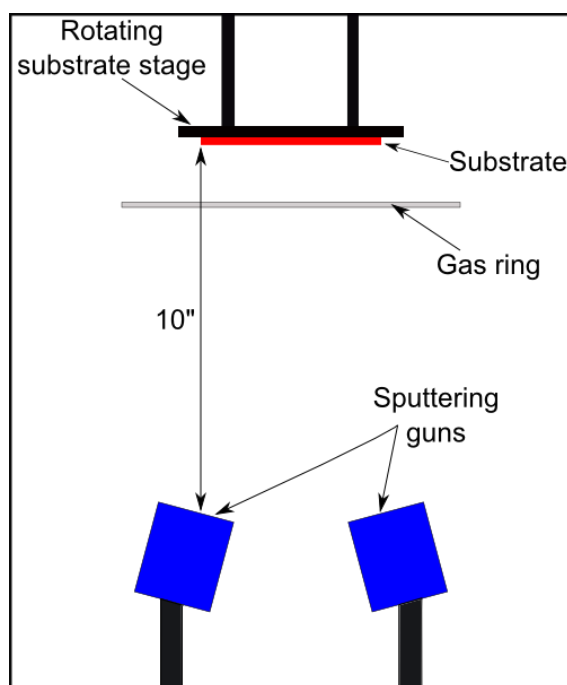


Figure 2-3: Schematic representation of the sputtering chamber.

Oxidized Si wafers with ~ 100 nm of thermal SiO_2 were used as substrates. A small portion was covered with Kapton tape to create a step profile in order to facilitate thickness measurements. The sputtering target was a 99.5% pure Vanadium target – 3" diameter, 0.25" thick. Argon (99.99% pure) was used as the base gas to sustain the plasma and was fed into the chamber through perforated rings around the sputter guns. The reactive gas, oxygen (99.99% pure), which was used to control the stoichiometry of the deposited films, was introduced through a gas ring located just below the substrate. The target power used was 300 W with a 20 kHz pulse yielding a power density of 6.8 W/cm^2 . The characteristic voltage-time pulse waveforms were monitored using a digital oscilloscope and one such characteristic response is shown in the Fig. 2-4.

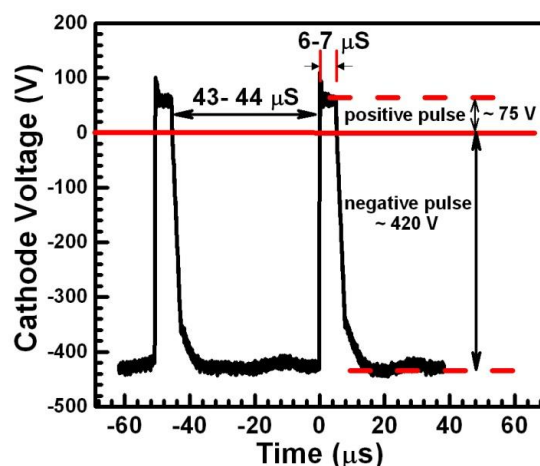


Figure 2-4: Pulse profile used for depositing VO_x films.

2.1.2 Film deposition procedure

The chamber was pumped down to a pressure of 10^{-7} Torr or lower using a turbo molecular pump. The working pressure was then set to 5 mTorr by allowing argon gas to flow into the chamber at the required rate. The target was pre-sputtered for 5 min. in pure argon atmosphere to remove any residual oxide layer that might be present on the surface. Subsequently, ultra high purity oxygen gas (99.99% pure) was introduced into the chamber through the gas ring. In order to determine the optimum conditions for VO_x depositions, a series of pre-deposition experiments were evaluated to understand the effect of chamber initial conditions and processing parameters on the V- target (cathode) current. (To a first order, the cathode current is proportional to the number of Ar^+ ions bombarding the target surface per second, which in turn determines the number of vanadium atoms sputtered per second.) For this purpose, the relative oxygen to argon percentage was varied in small incremental steps, keeping the total flow constant, and the corresponding changes in the cathode current were monitored. Care was taken to remain long enough (typically 5 – 10 min) at each step in order to allow sufficient time for the current to stabilize. Once the required high percentage of oxygen was

reached, the ratio was slowly decreased back to the starting value, monitoring the cathode current all the while. A similar hysteresis curve was also obtained by varying the total gas flow rate in the forward (increase) and reverse (decrease) directions while keeping the oxygen percentage constant.

Once the curves were obtained, films were deposited at various points along the hysteresis curves. When depositing films under conditions depicted by the forward curve of the hysteresis loop, the target was first conditioned by pre-sputtering in the metallic zone for 5 min, before letting in the required amount of oxygen just before opening the shutter. For samples under conditions of the backward curve, the conditioning needs to be done at high flow rates of oxygen. The oxygen flow rate is then reduced to the required rate a few seconds before opening the shutter. This is done to make sure that the target is in oxide mode at the instant when sputtering starts.

The deposited films were then characterized, structurally and electrically, to understand the correlation between film properties and the deposition conditions.

2.2 Annealing

A series of annealing experiments were done to modify the structure and properties of the vanadium oxide films and evaluate any beneficial effects on the TCR and resistivity. A tube furnace with quartz lining, equipped with glass covers at the front and back ends to facilitate gas flow, was used for these experiments. The ambient gas was fed into the back of the furnace and flowed out of the front cover through a bubbler filled with water. An OMEGA CN-2010 series programmable controller was used to control the temperature of the furnace. The furnace was first preheated to the required temperature at the rate of 10 °C/min. The samples were then placed on a Si wafer carrier and inserted into tube and annealed for the required time. Subsequently they

were taken out and air-cooled to room temperature. Because of the reactivity of the VO_x films, care was taken to ensure reproducible annealing conditions.



Figure 2-5: Picture of the tube furnace used for annealing experiments.

Two sets of annealing experiments were done – one in a nitrogen atmosphere (inert) and another in an oxygen atmosphere (oxidizing). The typical gas flow rates used were ~10 SCFH (standard cubic feet per hour) for both sets. Samples were annealed at four different temperatures – 200, 300, 400 and 500 °C for three different time periods – 10, 20 and 30 min.

2.3 Ion Implantation

The ion implantation was done at a commercial facility (Core Systems, CA). The implantation parameters were arrived at based on TRIM (Transport of Ions in Matter)

simulations. The energy was chosen in such a way that the peak of the Gaussian profile is located at approximately half the depth of the film. For a VO_x film, with $x \sim 2$, this value came out to be 10 keV. As an example, the simulation profile obtained for H^+ ion implanted into a VO_2 film with an energy of 10 keV is shown in Fig. 2-6. Four different ion implantation schemes were performed: $\text{H}^+ 10^{13}$ atoms/ cm^2 , $\text{H}^+ 10^{15}$ atoms/ cm^2 , $\text{He}^+ 10^{14}$ atoms/ cm^2 , $\text{He}^+ 10^{15}$ atoms/ cm^2 . The beam currents used were 10 μA , 40 μA and 80 μA respectively for the $\text{H}^+ 10^{13}$, $\text{H}^+ 10^{15}$ and the two He^+ implants.

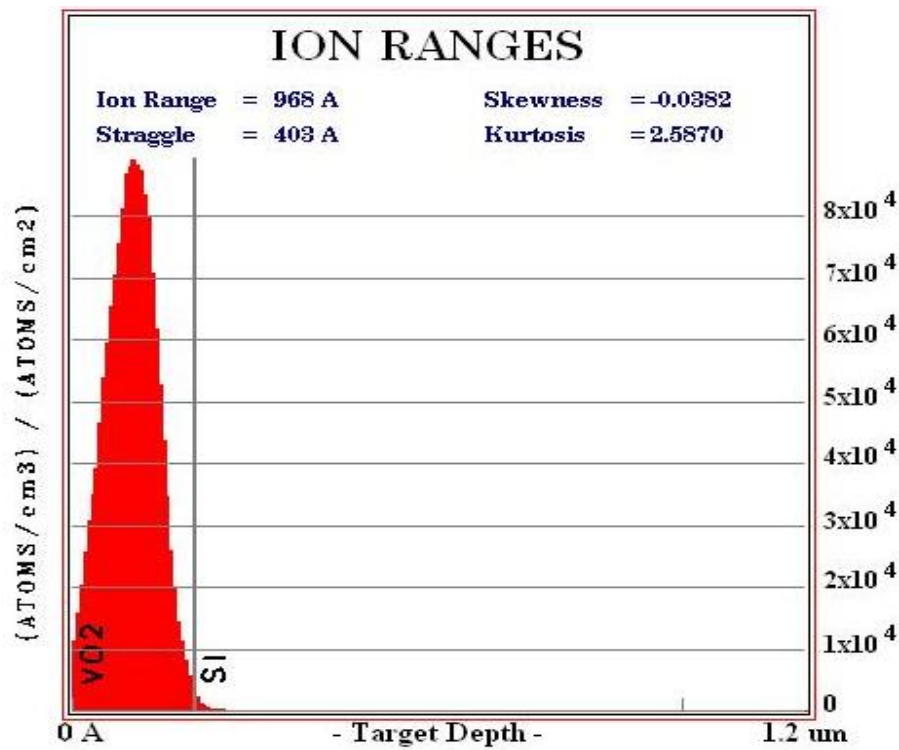


Figure 2-6: TRIM ion ranges for H^+ implanted into 200 nm VO_2 film on Si substrate with an energy of 10 keV.

2.4 Electrical Characterization

Resistivity and TCR are two of the most important metrics of the bolometer material. Resistance is usually obtained from the slope of the current-voltage curves, and resistivity is calculated by factoring in the appropriate contact spacing and cross-sectional area. The temperature coefficient of resistance (TCR) is defined as the percentage change in resistance (or resistivity) per unit change in temperature and is given by

$$TCR = \frac{1}{R} \frac{dR}{dT} \quad (2.1)$$

where R is the resistance of the film at the reference temperature.

To facilitate these measurements, nickel electrodes ~5 mm long, with separation ranging from 200 to 700 μm (see Fig. 2-7) were sputtered onto the VO_x films using a shadow mask. Current-voltage (I-V) curves were obtained using a Keithley 2400 source meter. To vary the measurement temperature, the samples were placed on an MMR Technologies low temperature microprobe station connected to a K-20 programmable temperature controller. Measurements were done at temperatures up to 105 $^{\circ}\text{C}$ in increments of 10 $^{\circ}\text{C}$, allowing sufficient time (typically 2 minutes) for the samples to stabilize at each temperature. Fig. 2-8 shows a typical set of I-V curves obtained for our VO_x films. The linearity of the curves suggests good ohmic contacts. The resistivities calculated are then plotted as a function of temperature as shown in Fig. 2-9. The TCR value is obtained from the slope of $\log \rho$ vs. T plot.

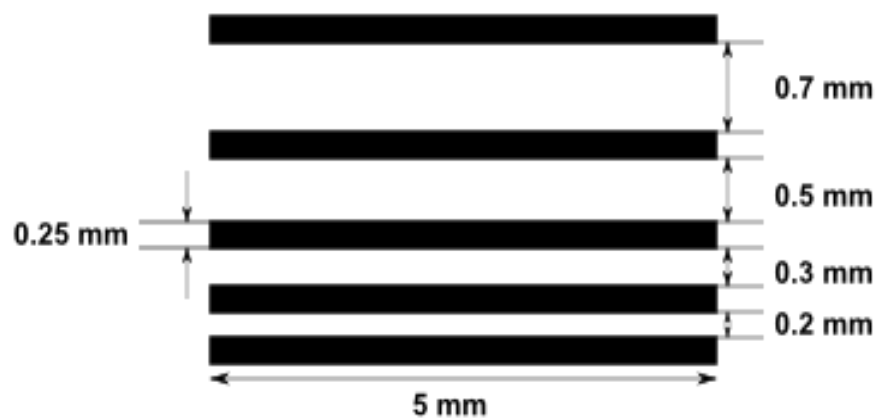


Figure 2-7: Schematic of the strip electrodes used for resistance measurements.

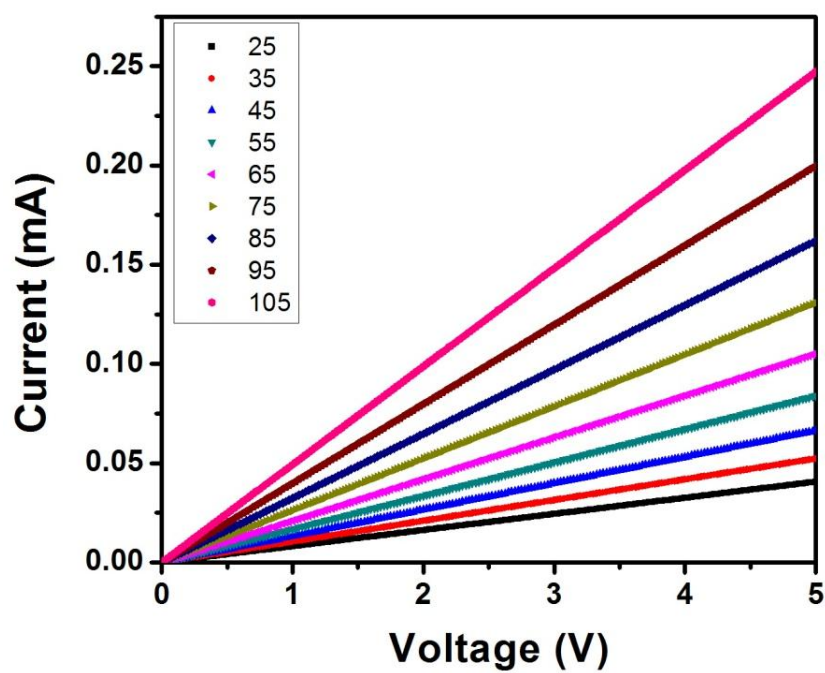


Figure 2-8: Typical current-voltage curves obtained for VO_x thin films at different temperatures.

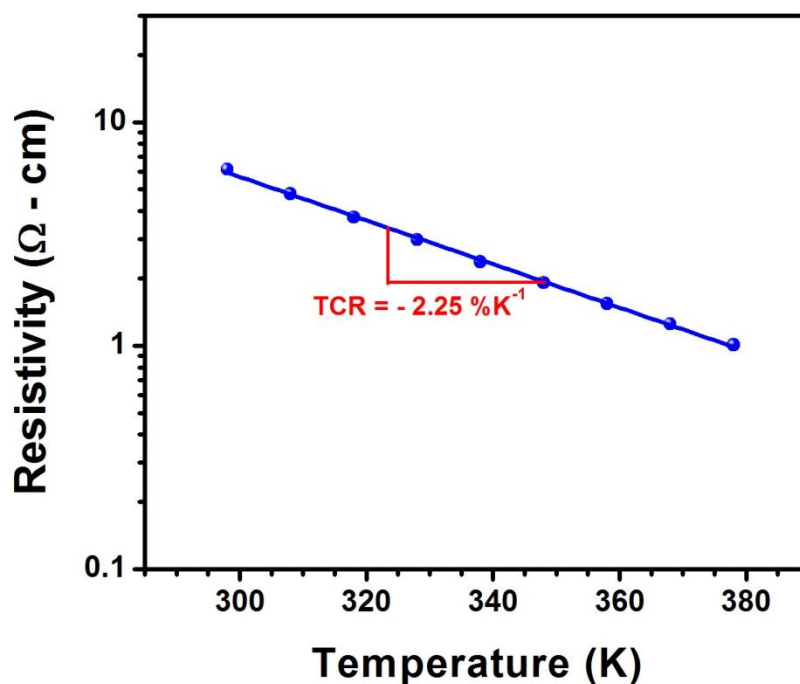


Figure 2-9: Graph showing calculation of TCR.

2.5 Profilometry

The film thickness, and consequently the deposition rate, was determined using a Tencor Alpha-step 500 surface profilometer. The step profile created by the kapton tape was used for this measurement. The stylus was made to scan over a length of 500 μm across the step to determine the difference in height between the two levels, which gives the thickness of the film. The force used on the stylus was 3.7 mg.

2.6 X-ray Diffraction

Glancing angle X-ray diffraction was done using a PANAnalytical PRO X'Pert MPD with $\text{Cu K}\alpha_1$ ($\lambda = 1.54 \text{ \AA}$) radiation, to analyze the structure of the deposited film. Diffraction

patterns were collected for 2θ values between 10° and 75° with a 2° glancing angle, and scanned at $3^\circ/\text{min}$ rate. The phases present were identified by comparing the peak intensities and their corresponding 2θ values to various vanadium oxide standards using the software MDI Jade v9.0.

2.7 Scanning Electron Microscopy

Cross-sectional microstructures of the films were obtained using a field emission scanning electron microscope (Leo 1530). Sample preparation involves cleaving a small piece of the sample, and mounting it onto the holder such that the freshly cleaved surface faces the electron source for imaging. Usually, an additional conducting layer of gold is deposited onto semiconducting or insulating samples in order to avoid charging effects. Alternatively, one could use lower operating voltages thereby minimizing the charging effect. In this work, a voltage of 1kV was used, with working distance between the lower portion of the lenses and the sample surface ranging from 1 to 3 mm. Under these conditions, the device had a resolution of 3 nm with a maximum magnification of about 200kX.

2.8 Atomic Force Microscopy

Atomic force microscopy (AFM) was used to obtain the surface roughness and grain size of the films. Images were collected using a Digital Instruments Dimension Series 3100 scanning probe microscope (Santa Barbara, CA) using 125 μm long etched silicon tips. The equipment was operated in tapping mode and images were collected over a $2\text{ }\mu\text{m} \times 2\text{ }\mu\text{m}$ area.

2.9 Raman Spectroscopy

Raman spectroscopy is a useful tool to obtain the vibrational properties of a material. Detailed information about material structure and bonding can be determined by analysis of the Raman vibrational spectrum. The Raman spectrum arises from the inelastic scattering of high-frequency radiation with the electron clouds that make up chemical bonds. When incident light impinges on the sample, most of the light is scattered elastically. However, a small percentage of the incident light can couple to a vibrational mode of the compound causing a loss of energy. The emitted lower energy photon, appears at a slightly different frequency than that of the incident beam and is typically described as a Raman shift. By comparing the Raman spectrum of standard samples to a sample of interest, detailed structural and bonding information can be obtained.

Micro-Raman spectra were collected using a Renishaw inVia Raman Microscope (Renishaw Inc., Gloucestershire, UK) configured in a backscattering geometry. The excitation source was a HeNe laser (632.8 nm) with an incident sample power of ~5 mW. All spectra were collected using a 100X microscope objective (with a numerical aperture of 0.9) which provides a spatial resolution of ~ 1 μm . Since the films are typically grown on Si single crystal wafers, a large Si background signal is always observed and serves as an internal wavelength calibration signal for each sample. The Raman features due to the VO_x films are obtained by spectral subtraction of a Si reference spectrum taken from an uncoated Si wafer.

Chapter 3

Pulsed-dc sputtering of vanadium oxide

As mentioned in the previous chapters, sputtering of vanadium oxide is a complex process due to its non-equilibrium nature, and hence requires precise control in order to achieve required properties. Even a slight change in the thin film processing parameter can affect the stoichiometric uniformity as well as the resulting electrical properties. This chapter focuses on the evaluation of various process parameters in the pulsed-dc reactive sputtering of vanadium oxide, to arrive at optimal deposition conditions. In particular, the effect of total gas flow rate and the oxygen percentage in the reactive gas mixture on the target current is analyzed and subsequently correlated to the electrical and structural properties of the resultant film.

3.1 Process hysteresis characteristics:

One of the significant characteristics of the reactive sputtering process is target current hysteresis. Fig. 3-1(a) shows the variation of the cathode (target) current as a function of the percent oxygen flow in the chamber for various total ($\text{Ar} + \text{O}_2$) gas flow rates. For the 18 sccm gas flow rate, at low oxygen percentages, the current remained stable at a maximum value of ~ 0.85 A. However, when the oxygen percentage reached $\sim 12\%$, the cathode current dropped abruptly to about 0.65 A. This occurs due to the formation of an oxide layer on the target. In effect, the target sputtering rate is overwhelmed by the target oxidation rate. This is often referred to as target poisoning when the effect is undesirable. At O_2 percentages greater than 12%, further increase in oxygen caused only small changes in the target current indicating a stable sputtering zone. As can be seen in the figure, when

the oxygen percentage was slowly decreased, the current did not immediately return to the high value of ~ 0.85 A at 12% O_2 . Instead it increased very slowly (on the order of mA), and the target remained in the oxidized target regime until the oxygen percentage reached $\sim 8\%$, at which point it rapidly rose back up to the initial value of 0.85 A. At 18 sccm total flow rate, the process hysteresis leads to an unstable target zone from ~ 8 to 12% O_2 which can lead to large variability in the electrical properties of VO_x thin films deposited within this window. A similar hysteresis curve was observed for a process with 32 sccm of total gas flow. However, in this case, the observed intermediate zone was much smaller and occurred at lower oxygen partial pressures, $6.5\% < O_2 < 8\%$. Further increase in the total gas flow rate continued to decrease the width of the process hysteresis as well as shift the hysteresis window to lower O_2 percentages. At 58 sccm, the hysteresis became very slim and the unstable intermediate zone occurred for 4-5 % O_2 , as shown in Fig. 3-1(a).

If the hysteresis curves are replotted in terms of total oxygen flow instead of percent oxygen flow, an interesting trend develops as seen in Fig. 3-1(b). In all three curves, regardless of the total gas flow, the forward hysteresis legs converge near 2.5 sccm of oxygen. This suggests that in the case of this specific system volume, pressure (5 mTorr) and target size (3"), an oxygen flux of ~ 2.5 sccm is sufficient to oxidize the target. Surprisingly, the amount of Ar flowing through the system can vary significantly, i.e. from ~ 15.5 to 55.5 sccm of Ar and not drastically affect the onset of target oxidation. However, the Ar flow rate does appear to affect the recovery of the metal target regime on the reverse leg of the hysteresis, with higher Ar flow rates leading to faster recovery and a smaller hysteresis width. This is because higher Ar gas flow rates are able to remove any lingering oxygen gas much more quickly. At lower flow rates, the reactant species have enough time to influence the target conditions gradually. But as the gas flow rate is increased, in order to

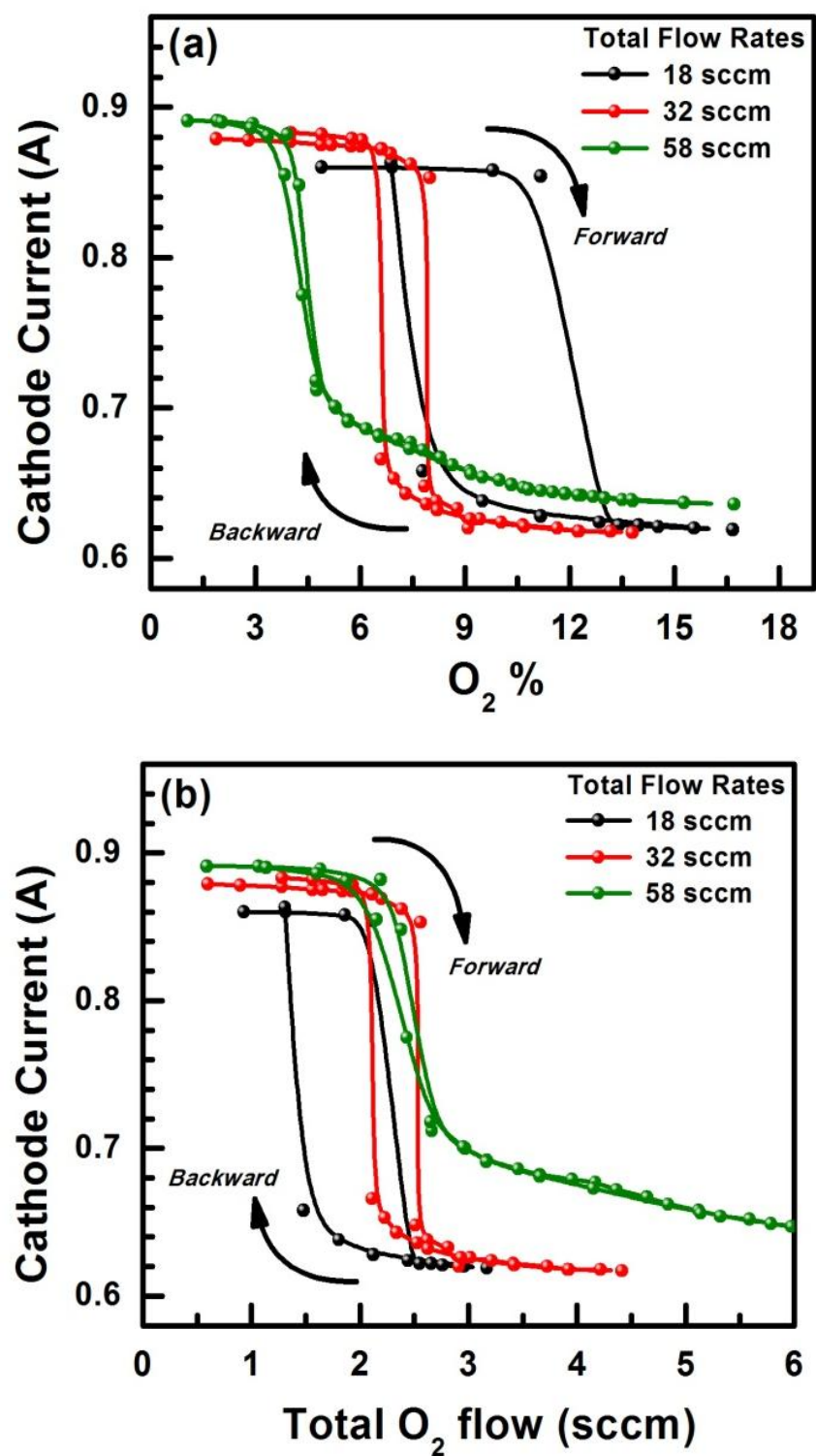


Figure 3-1: Variation of cathode current as a function of (a) oxygen percentage (b) total oxygen flow in the chamber.

maintain the same total pressure, the pumping speed of the chamber also increases, and hence the reactant residence time decreases. This also explains the variations in the saturation current values at various flow rates. Saturation current is lowest at the lowest flow rate since the species have enough time to more thoroughly react and oxidize the target.

Similar experiments under variable total gas flows at fixed oxygen percentage also yielded hysteresis responses in target currents, as shown in Fig. 3-2(a). Overall, the hysteresis curves are similar to those observed in the earlier data, where the total gas flow was kept constant and the oxygen percentage was varied. At a constant 5% pO_2 , an intermediate zone was found in the range 50-70 sccm where the cathode current gradually dropped from ~ 0.85 A to 0.7 A, beyond which point it remained relatively stable. Upon reversing the total flow rates, the current stayed low till about 60 sccm, below which it started increasing back towards its starting value. However, at a 10% O_2 level, a larger hysteresis width was observed along with a shift in the position of the intermediate zone to lower total gas flow rates.

Fig. 3-2(b) displays the constant percent oxygen data replotted in terms of total oxygen flow. Once again, the three forward hysteresis legs begin to descend near a common total oxygen flow, in this case 2.7 sccm, which is close to 2.5 sccm observed in the earlier data presented in Fig. 3-1(b). These experiments indicate that the nature of the target current is effectively determined by the total O_2 flow and that the Ar gas flow rate plays a minor role. Thus, the process for the reactive sputtering of a metallic target can be distinguished into three operating regimes based on the oxygen mass flow [58]. At low oxygen gas flows, (region I, identified as the *elemental* zone), most of the oxygen is incorporated into the deposited film or getterred by vanadium metal present on the chamber

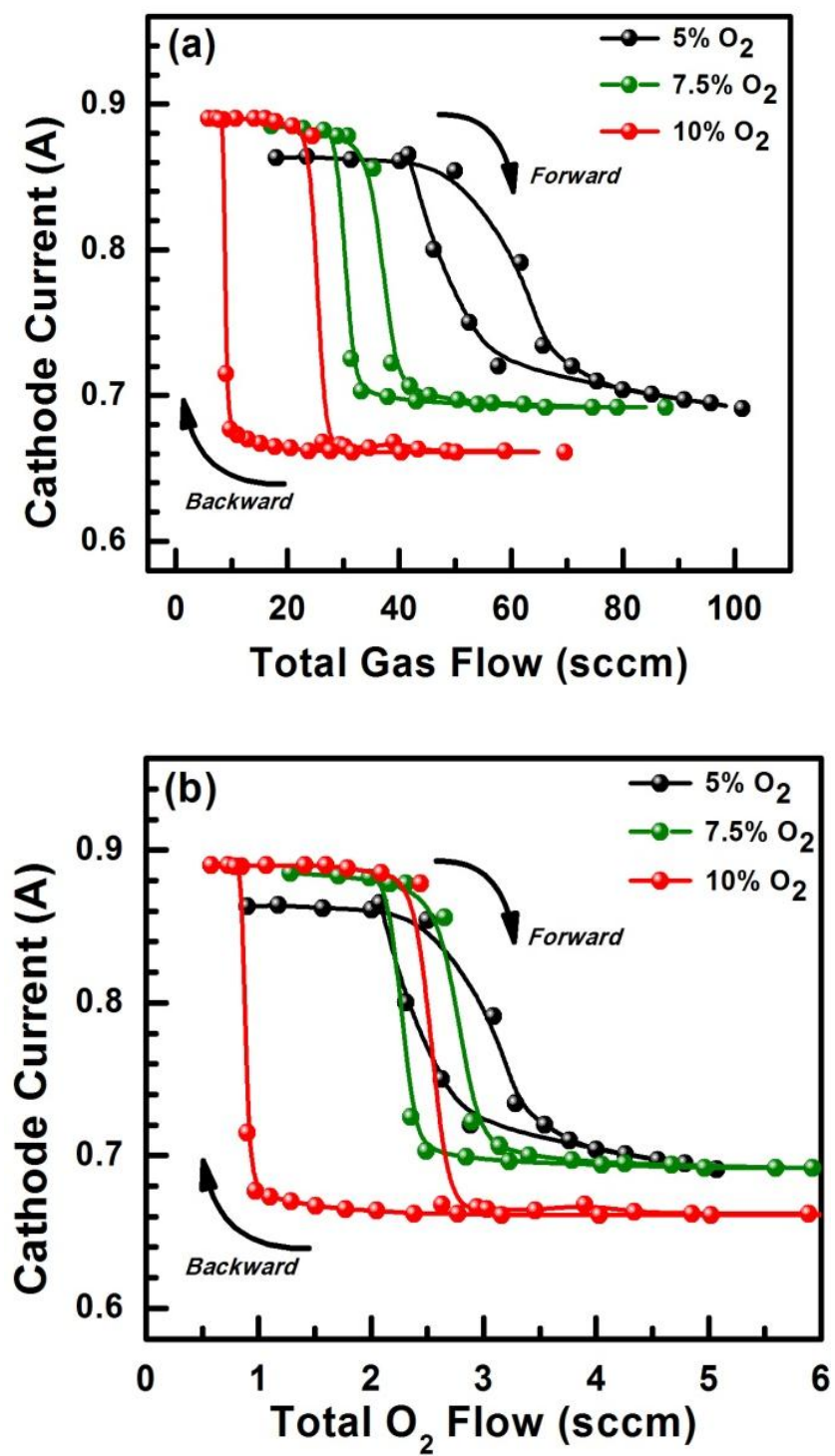


Figure 3-2: Variation of cathode current as a function of (a) total gas flow (b) total oxygen flow in the chamber.

walls which leaves the target impedance mostly unaffected. In region II, (the *intermediate* zone), as the oxygen mass flow increases, the amount of oxygen present in the system begins to overwhelm the gettering rate of the sputtered vanadium metal leading to the local oxidation of the target and less sputtered vanadium metal. This cascade of events eventually leads to an abrupt increase in target impedance. This continues until the target is “fully oxidized” and a steady state is attained in region III, the *oxidized* zone. The composition of the target changes continuously with the change in flow rate of the reactive gases as indicated by change in cathode current. These observations are consistent with Berg’s theory of reactive sputtering [59].

Films were then deposited at various points along the hysteresis curves and their structural and electrical properties evaluated.

3.2 Structural Properties:

One of the immediate consequences of the oxidation of the target and the sputtering process hysteresis can be observed in the film deposition rate. As an example, Fig. 3-3 shows that the deposition rates of VO_x films indeed exhibited hysteresis with total gas flow rates at a fixed oxygen percentage. It has been reported that the differences in the film deposition rates as a function of available reactive species is due to an increase in the binding energy of V on the target surface and hence a decrease in the sputter yield [58].

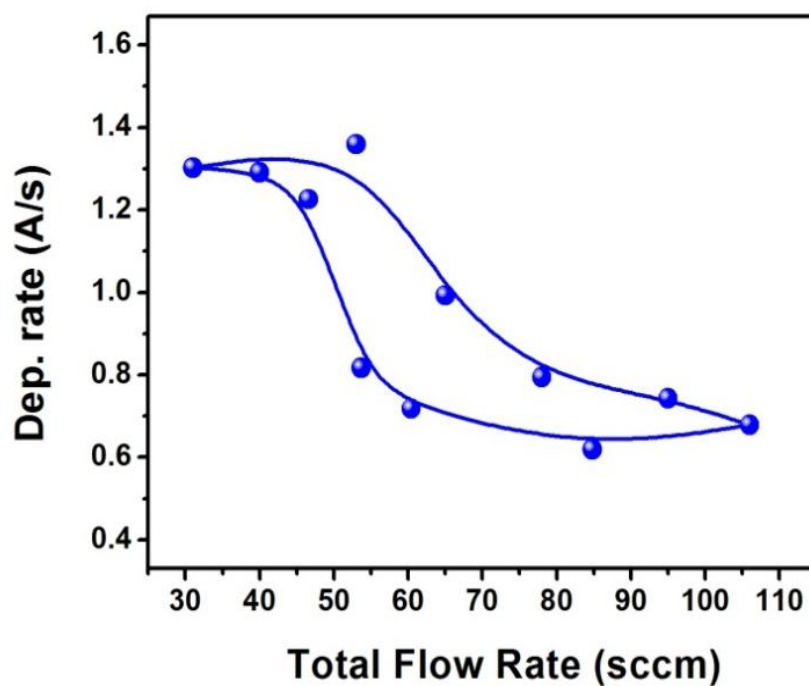


Figure 3-3: Deposition rate as a function of total gas flow rate at 5% O_2 .

Fig. 3-4 shows X-ray diffraction data of films deposited at fixed total flow rate (18sccm) but different oxygen percentages. At low oxygen percentages, FCC VO phase seems to dominate with distinctive XRD peaks. However, at higher oxygen percentages, the films were found to be X-ray amorphous. A similar effect was observed with an increase in the flow rates at fixed oxygen percentages. The peak around 53° is from the reflection of the Si (311) plane. This peak is often observed during GIXRD, and it moves around its mean position when the grazing incidence angle, α , is varied [60, 61].

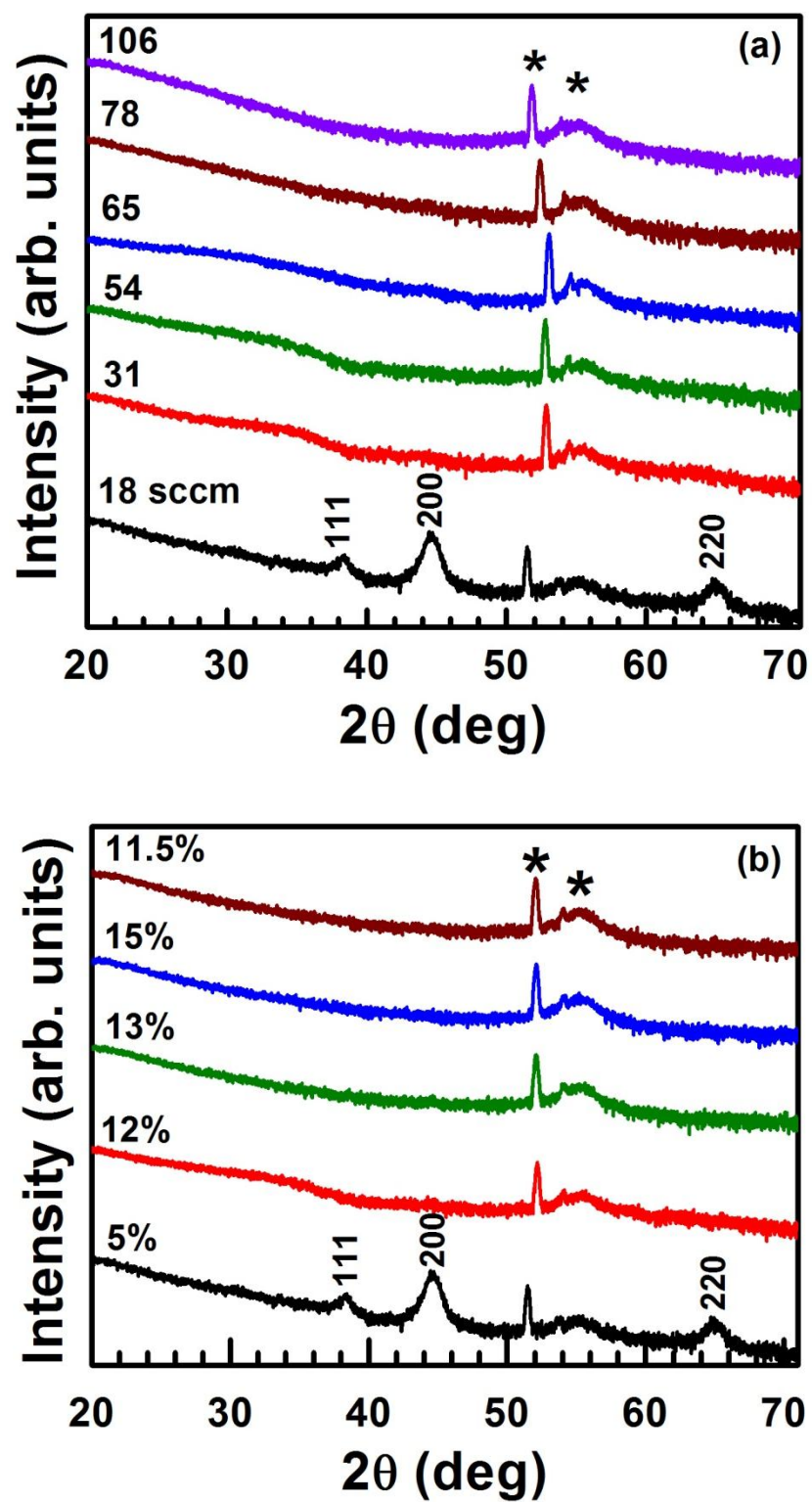


Figure 3-4: X-ray diffraction patterns of films deposited at (a) 5% O₂ and different flow rates (b) 18sccm flow and different oxygen percentages.

To assess the influence of total gas flow rates on the microstructure of the VO_x films, cross-sectional SEM analysis was performed on selected samples. Fig. 3-5 shows cross sectional SEM images of the VO_x films deposited with 5% O_2 at different total gas flow rates. It is evident that as the total flow rates increased (from 30 to 90 sccm), the film microstructure changed from columnar to equiaxed features even though the oxygen partial percentage is same for these samples. However, films deposited at fixed total flow (18 sccm) and different oxygen percentages did not show this transition, remaining columnar even at high oxygen percentages (see Fig. 3-6).

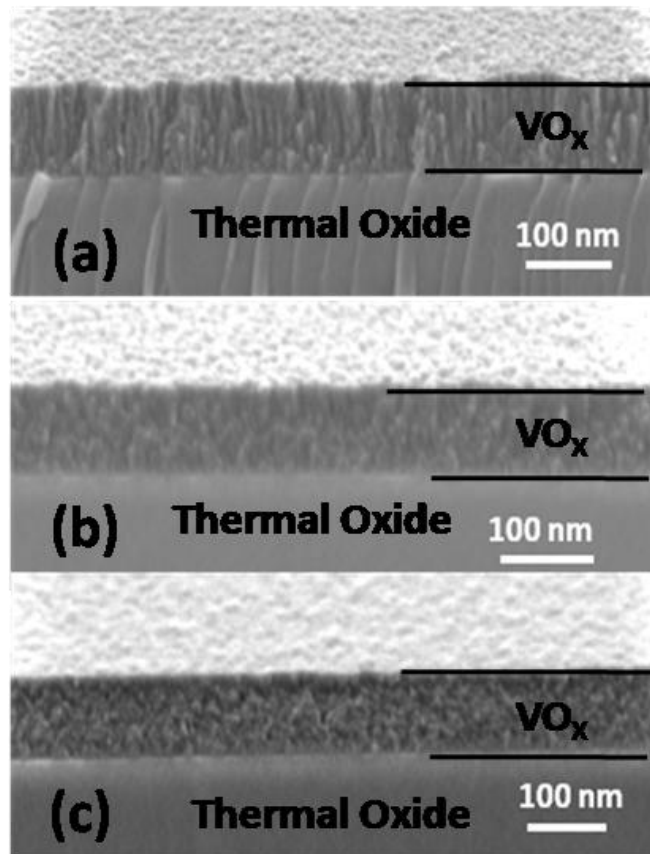


Figure 3-5: Cross-sectional FESEM images of samples deposited with 5% O_2 at different flow rates - (a) 31 sccm (b) 65 sccm (c) 90 sccm.

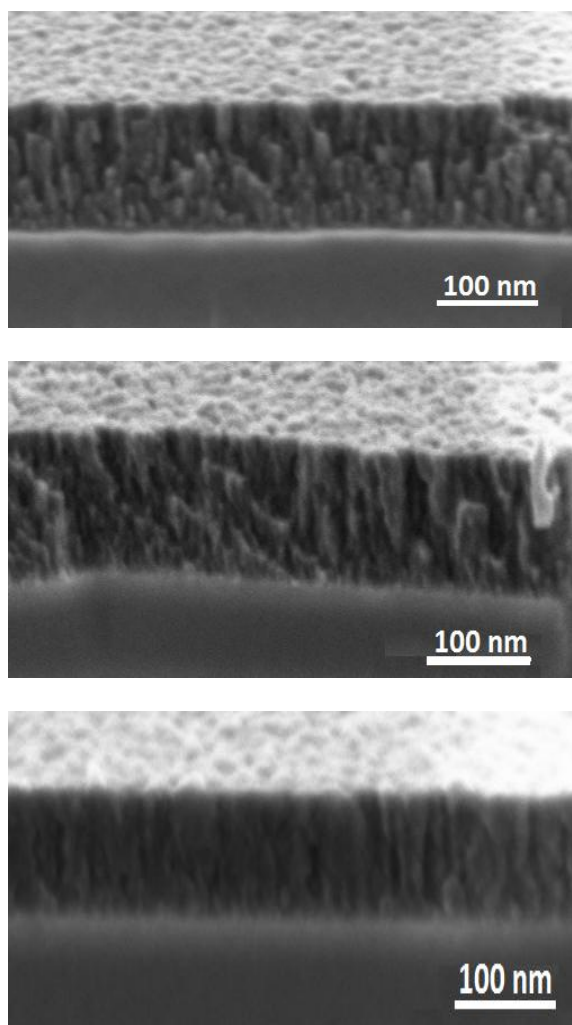


Figure 3-6: Cross-sectional FESEM images of samples deposited at 18 sccm flow with different oxygen percentages - (a) 5% (b) 12% (c) 15%.

Raman spectra of the samples deposited at constant flow rate of 18 sccm are shown in Fig. 3-7. The films grown between 10-14% O_2 on the forward curve appear very similar, in sharp contrast to the film grown at 17% O_2 which displays a significantly different Raman signature (Fig. 3-7(a)). The features observed at 10-14% O_2 levels are typical of amorphous $VO_{x \sim 2}$ thin films [52]. The largest peak at $\sim 890\text{ cm}^{-1}$, is attributed to a V-O stretch (usually associated with V^{4+}) while the broad peak centered near $\sim 370\text{ cm}^{-1}$ is likely due to a V-O bending mode. The spectrum of the 17% O_2 film, however, suggests the presence of a

disordered V_2O_5 phase. On the reverse curve of the hysteresis, the disordered V_2O_5 phase persists from 15% O_2 to the 9% O_2 level, only reverting back to the amorphous VO_{x-2} phase at 8% O_2 (Fig. 3-7(b)).

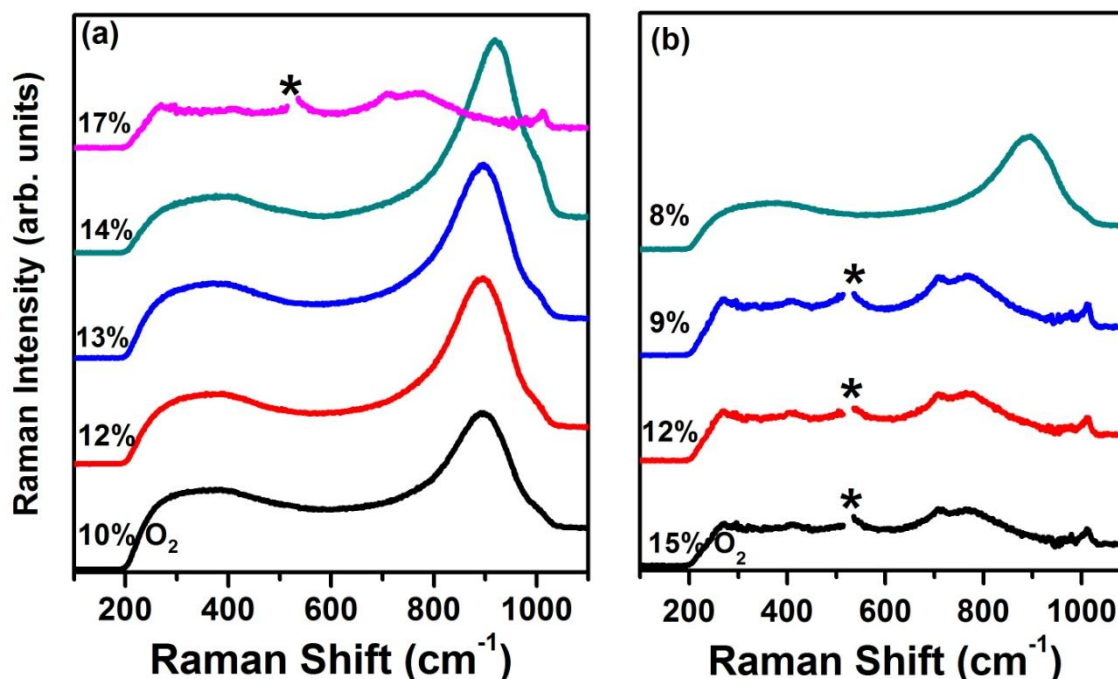


Figure 3-7: Raman spectra of samples deposited at a constant flow rate of 18 sccm in the (a) forward and (b) reverse legs of the hysteresis curve shown in Fig. 3-1. Features denoted by the * are artifacts due to the subtraction of a Si reference spectrum.

Examination of the hysteresis plot in Fig. 3-1 shows that the “poisoned regime” exists above 12% O_2 on the forward curve of the hysteresis, and while the most drastic change in the Raman spectra does not occur until 17% O_2 , there are still significant changes present in the other spectra. Most notably there is a large change in the relative intensity of the two main peaks. At 10% O_2 , the ratio of the higher frequency peak at 890 cm^{-1} to the lower frequency peak at 370 cm^{-1} is ~ 2.0 . This ratio steadily increases to 2.6, 2.6 and 3.7 at the 12, 13 and 14% O_2 levels respectively. This increase in relative Raman intensity is most

likely due to an increase in the Raman scattering cross-section of the films as the oxidation level increases [62]. The increasing level of oxygen in the system eventually leads to the formation of a disordered V_2O_5 thin film at 17% O_2 . The disordered V_2O_5 phase persists on the return path of the hysteresis until the target begins to become metallic at 8% O_2 .

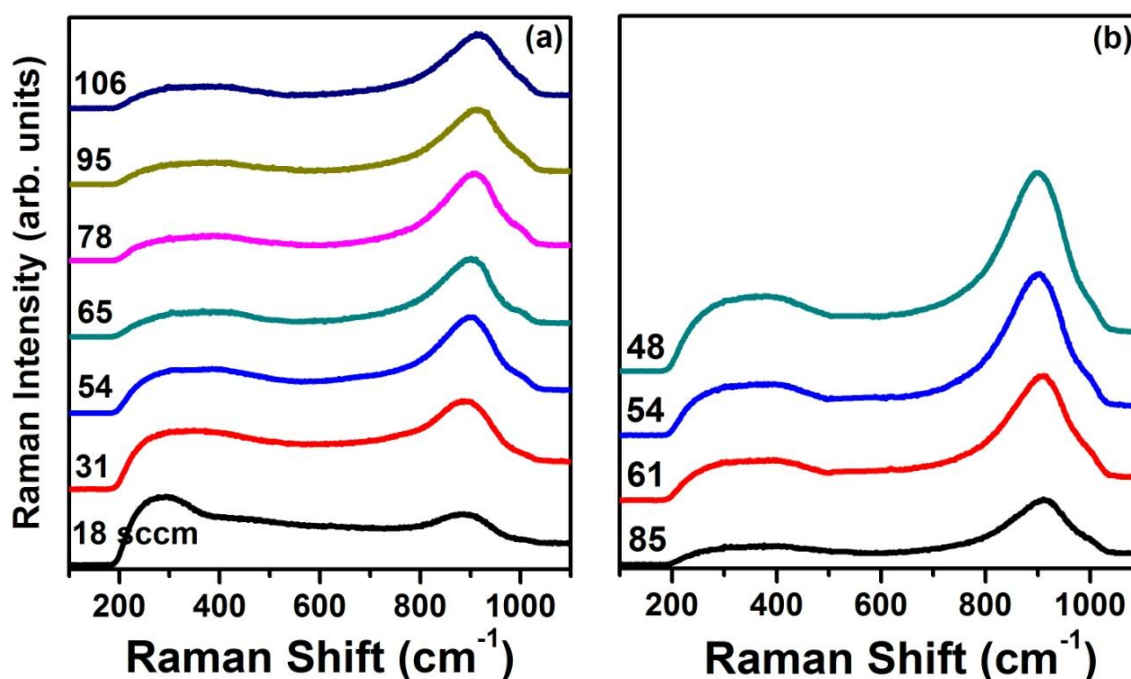


Figure 3-8: Raman spectra of samples deposited at a constant oxygen percentage of 5% along the (a) forward and (b) reverse parts of the hysteresis curve shown in Fig. 3-2).

The second set of Raman spectra, displayed in Fig. 3-8, corresponds to the hysteresis curve in shown in Fig. 3-2. In this case, the relative amount of O_2 is kept constant at 5% while the total system flow rate is varied. In contrast to the earlier Raman data, no significant changes in the spectra are observed and all the spectra look relatively similar to each other. The exception is the spectrum of the 18 sccm sample, where the low frequency peak is observed at a much lower frequency, 285 cm^{-1} than the ~ 370 cm^{-1} position observed in the other spectra. The position of the peak at 285 cm^{-1} is significant and indicates the

presence of defective FCC VO rock salt nanocrystals [63]. This is corroborated by the presence of FCC VO in the XRD data depicted in Fig. 3-4. Another major difference in the 18 sccm spectrum is the weak intensity of the V-O stretching mode of amorphous $\text{VO}_{x \sim 2}$ at 890 cm^{-1} , suggesting that a comparatively smaller amount of amorphous VO_x is present in the 18 sccm sample in contrast to the samples at higher flow rates.

Comparing the relative intensity ratio of the high frequency mode to the low frequency mode, it was observed that it gradually increases from 0.8 at 18 sccm to 1.5 at 31 sccm to 2.2 at 54 sccm before maximizing at 3.4 at 78 sccm. This is similar to the behavior observed in the previous set of Raman spectra. As the amount of overall oxygen in the system increases, the relative intensity ratio of the high to low frequency modes increases as well. The same behavior is also observed on the reverse leg of the hysteresis, with relative ratios of 3.3, 3.1, 3.1 and 2.6 observed for the 85, 61, 54, and 48 sccm flow rates respectively. In addition, the high frequency mode also appears to shift gradually to higher frequencies as the total gas flow increases. At 18 sccm the peak is at 882 cm^{-1} and slowly shifts upward to a maximum of 915 cm^{-1} at 106 sccm.

3.3 Electrical Characterization:

The resistivities of the deposited films were measured using 2-point probe technique as explained in Chapter 2. All films exhibited linear I-V behavior between 0 and 5 V. The overall trend observed was that as the cathode current decreases, the resistivity of the sample increases for a given oxygen percentage in the plasma but different total flow. This is not surprising, since as the cathode current decreases, the sputter rate of V- metal decreases, and hence the vanadium to oxygen ratio decreases, resulting in more oxygen rich

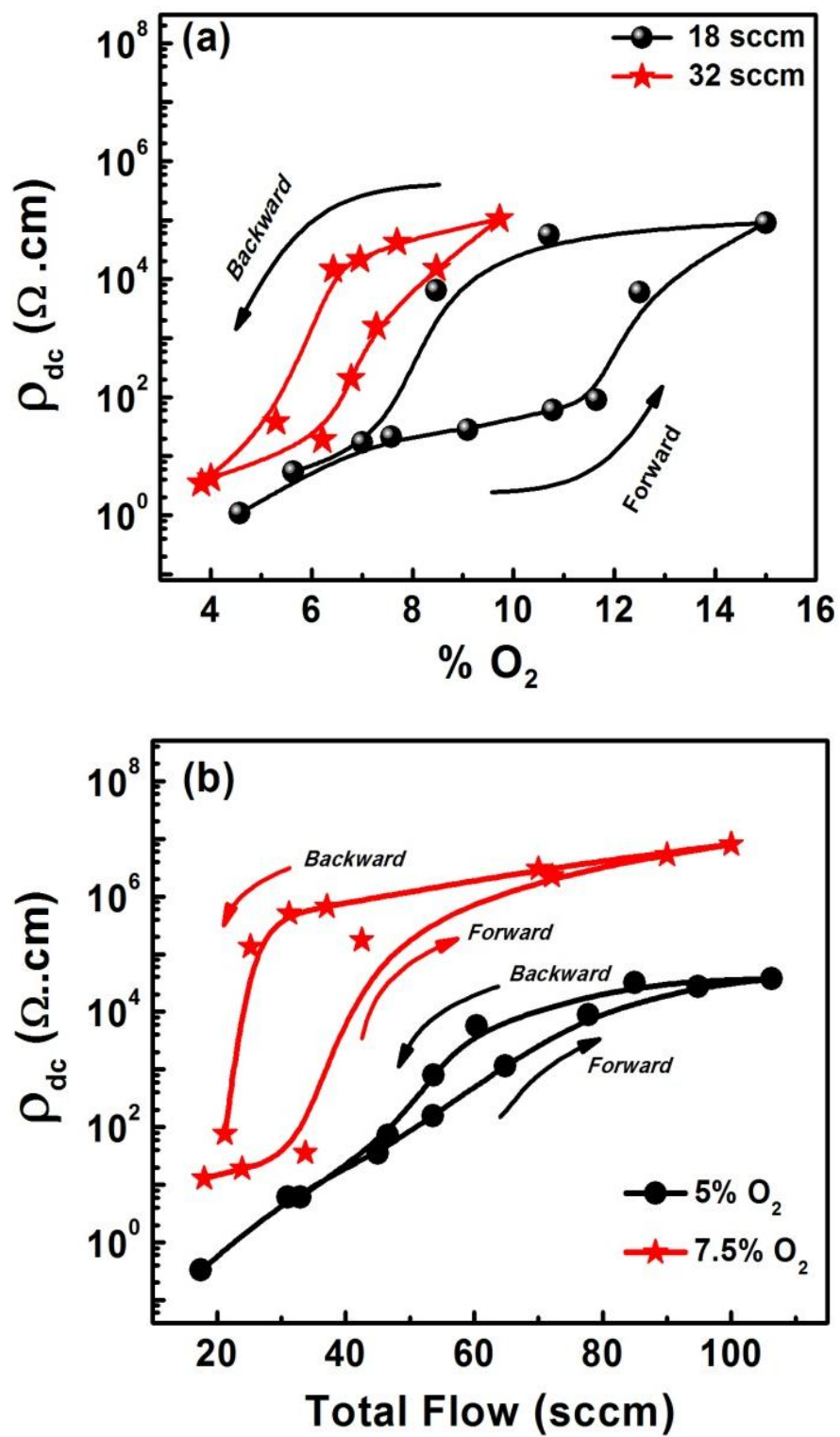


Figure 3-9: Resistivity of the films as a function of $\text{O}_2\%$ and total flow rate.

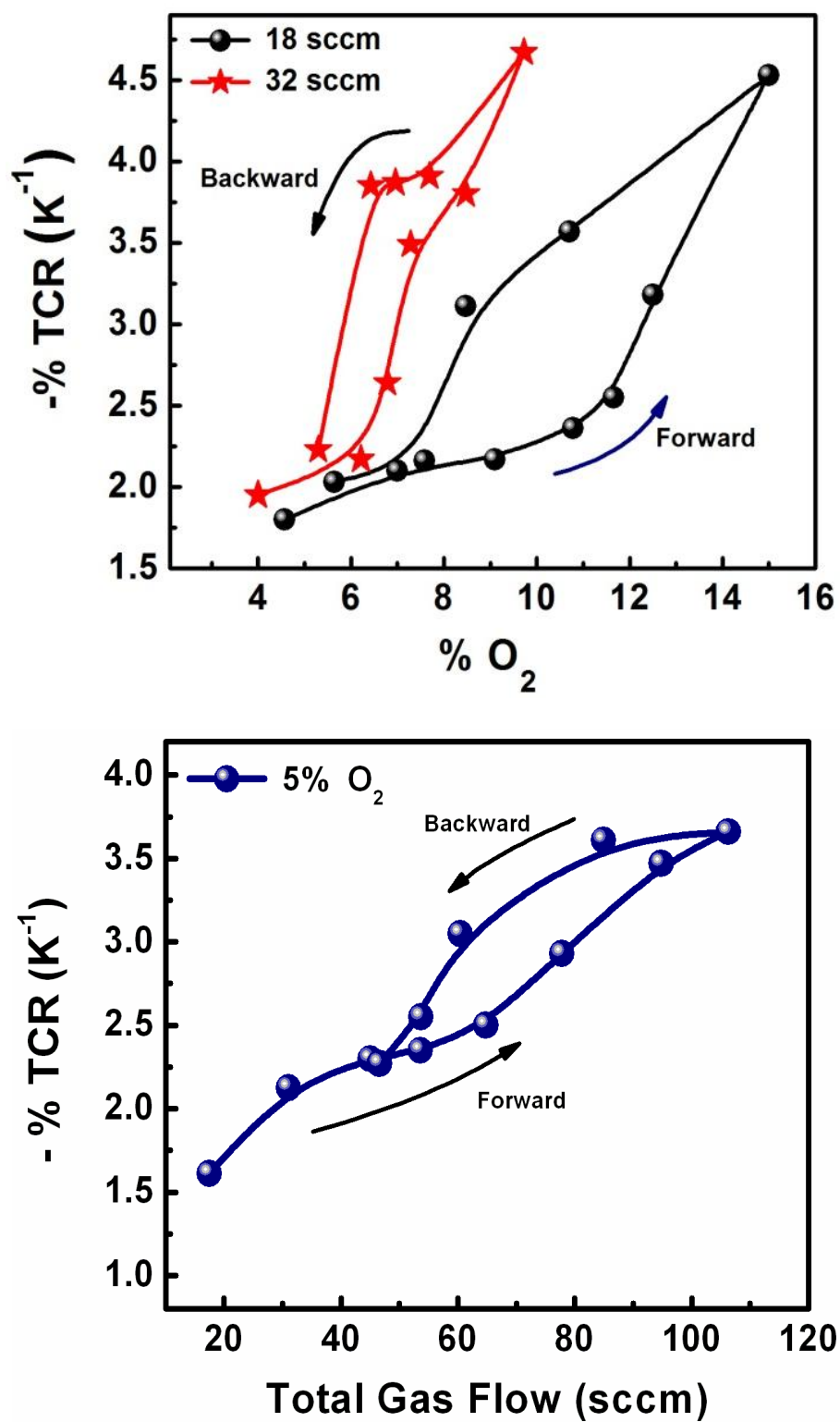


Figure 3-10: TCR of the films as a function of $O_2\%$ and total flow rate.

VO_x films with corresponding higher resistances. However, at higher cathode currents, in the elemental zone, the film properties depend on both the oxygen content and flow rate since the reaction is limited by the amount of oxygen present in the chamber available to react at the growing film surface.

When the room temperature resistance of the films was plotted as a function of O₂%, Fig. 3-9(a) and total gas flow rate, Fig. 3-9(b), it also exhibited a hysteresis behavior. This can be attributed to the hysteretic behavior exhibited by the cathode current since the resistivity of the films has a direct dependence on the cathode current. Particularly, the VO_x films that are processed in the *intermediate* zone vary greatly in properties and correlate to the target current as it directly influences the V:O ratio and hence the resulting structural/electrical properties of the film. This hysteresis behavior is also reflected in the TCR of the films as shown in Fig. 3-10.

Figure 3-11 shows the plot of the resistivity of all the films deposited under various conditions, including both segments of the hysteresis loop, as a function of their cathode current. A linear dependence was observed, with slight deviations at the two extremes. The deviations are believed to be due to the current saturating and the reaction becoming limited by the amount of oxygen present in the chamber. But in the central regime, the resistivity had a direct dependence on cathode current. Hence cathode current can be used as a diagnostic measure for controlling the film properties.

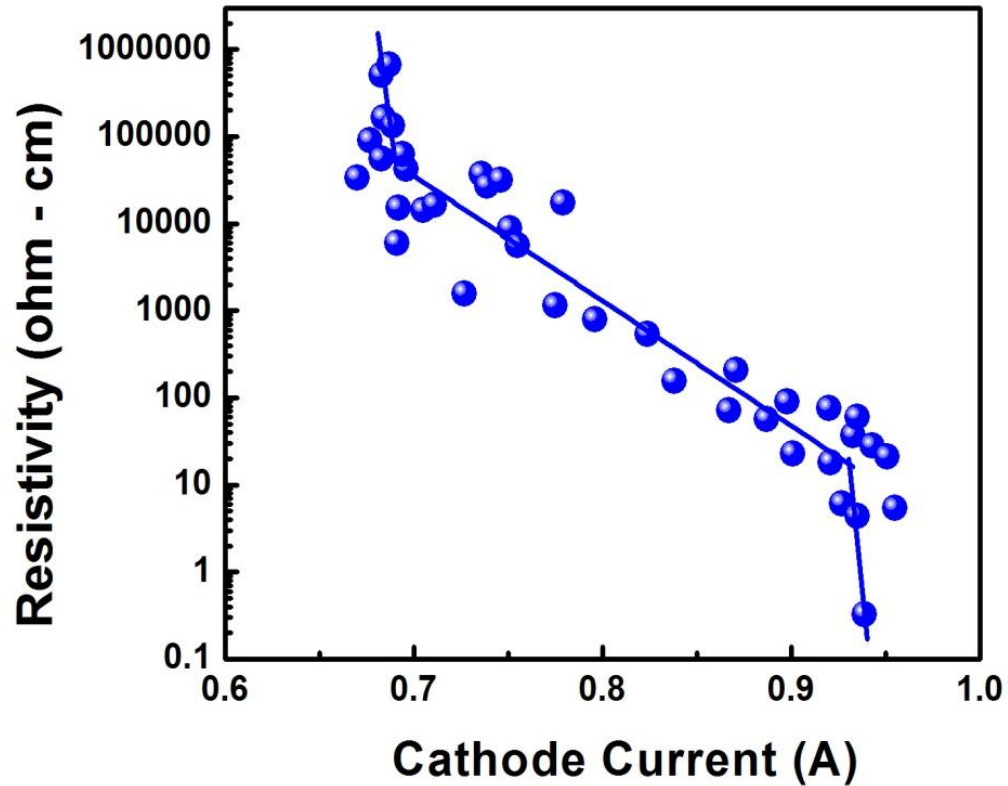


Figure 3-11: Dependence of resistivity on cathode current.

3.4 Application of the Meyer-Neldel Rule:

In order to better understand the mechanisms controlling TCR and resistivity, a qualitative analysis of transport properties was performed to correlate the sputter-process hysteresis conditions to the temperature dependent electrical conductivity responses, within the framework of Meyer-Neldel's Rule [64]. In general, conductivity (σ_{dc}) due to charge carrier migration in amorphous/disordered materials can be expressed by the empirical relation:

$$\rho_{dc}^{-1} = \sigma_{dc} = \sigma_a \exp\left(\frac{-E_a}{kT}\right) \quad (3.1)$$

where E_a is the activation energy for charge migration and σ_a is the pre-exponent that provides information about electronic states. According to the Meyer-Neldel rule (MN rule), this conductivity pre-factor σ_a itself has an exponential dependence on the activation energy as given by [64]:

$$\sigma_a = \sigma_{ao} \exp \left(\frac{E_a}{E_{MN}} \right) \quad (3.2)$$

where E_{MN} is the Meyer-Neldel constant. If the E_{MN} value is positive, it is known as the conventional MN rule and if E_{MN} is negative, it is known as the inverse MN rule. Fig. 3-12 shows a hypothetical plot of distribution of density of states ($N(E)$) between conduction (E_c) and valance (E_v) bands with the Fermi energy level (E_F) located within the band gap typical of a semiconducting material. This localized density of states (DOS) distribution changes with temperature and bias conditions, compensating the local charge trap sites. Even though Eq. 3-2 was proposed initially as an empirical relation, its physical significance is that the Fermi energy in an amorphous semiconductor/insulator shifts its position to maintain charge neutrality depending on the variations in the localized state concentration and distribution within the mobility gap [65]. In particular, if the DOS are exponentially distributed (gaussian form) in energy and the Fermi level is controlled by a deeper DOS in the mobility gap, the energy factor (E_{MN}) in the Eq. 3-2 is related to the energy distribution of these trap states while the pre-factor (σ_a) is related to the microscopic transport properties.

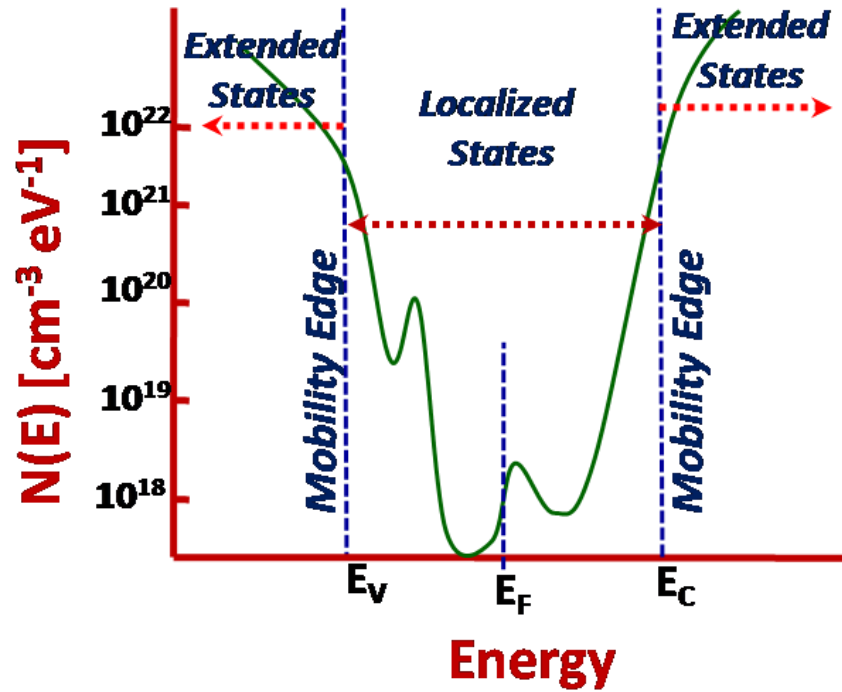


Figure 3-12: Schematic of density of states in mobility gap of an amorphous semiconductor.

The activation energies of these VO_x films were found to lie in the 0.1 – 0.5 eV range for different series of samples that were made along the hysteresis curves in Fig. 3-1 and 3-2. As shown in Fig. 3-13(a), the VO_x thin film samples deposited at 18 sccm total flow with oxygen percentages varying between 5 and 15% obeyed both conventional and inverse MN rules. Below 12% O_2 , the $\log(E_a)$ vs. $\log(\sigma_a)$ has a negative slope of $(-16.5 \pm 4.3) \text{ eV}^{-1}$ indicating an inverse MN rule, whereas above 12%, the slope is $(5.7 \pm 2.4) \text{ eV}^{-1}$ showing conventional MN behavior. Similarly, films deposited at a fixed oxygen percentage of 5% exhibited an inverse MN behavior with a slope of $(-26.3 \pm 1.5) \text{ eV}^{-1}$ for total flow less than 60 sccm, and a direct MN behavior with a slope of $(5.9 \pm 1.9) \text{ eV}^{-1}$ above this value. It is interesting to note that this changeover point from an inverse to a direct MN behavior coincides with the change in the target condition from a metallic to an oxidized state.

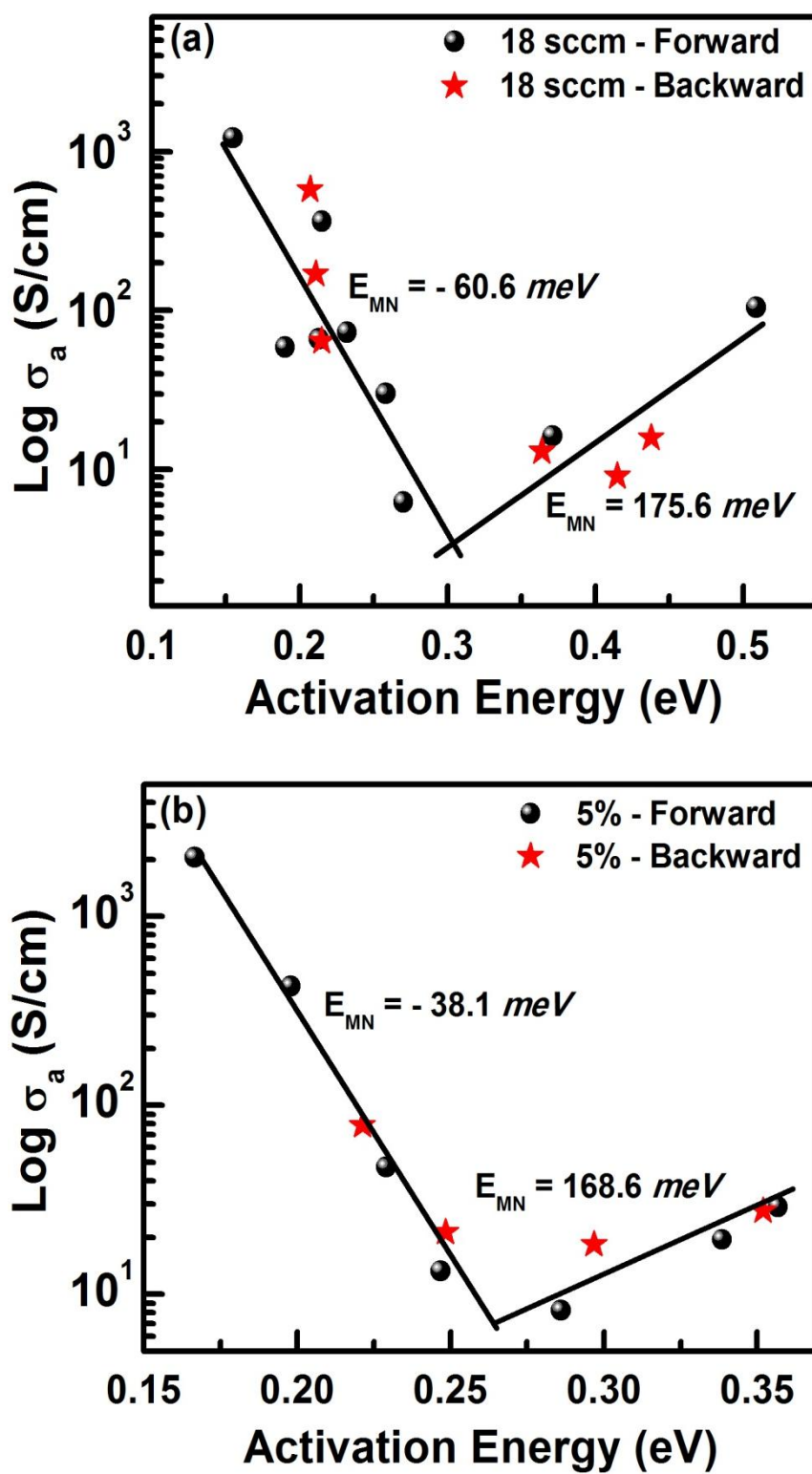


Figure 3-13: Meyer- Neldel relation for samples deposited at [a] fixed oxygen percentage (5%); [b] fixed total flow rate (18 sccm).

The above variations in the E_{MN} values are generally attributed to the differences in the DOS in the material, which in turn depends on the number of dangling bonds [66], or possibly, the V:O ratio in these films. A similar transport behavior obeying inverse MN behavior at low activation energies and direct MN rule at higher activation energies has also been observed for undoped $\mu\text{C-Si}$ films [67] and for non-metallic YBCO films [68]. In $\mu\text{C-Si}$, the inverse-MNR behavior of low activation energy films is attributed to their dense columnar microstructure, which leads to long range ordering and hence delocalization of an appreciable range of states in the band tail state distribution. Similarly, in YBCO, it is explained using a numerical model which is also based on the differences in the density of states for various oxygen concentrations in the film. Hence, observation of this behavior in vanadium oxide films suggests the existence of very many localized states in these films which contribute to conduction. Also their energy distribution and the electron-lattice coupling are determined by the compensation of the V:O defects[65], which in turn depends on the processing conditions.

3.5 Summary

Vanadium oxide thin films were deposited over a wide range of flow rates and oxygen partial pressures and their TCRs were plotted as a function of resistivities. The general trend observed was that a higher TCR corresponds to a higher resistivity. Films with characteristics similar to those used in the microbolometer industry were obtained at low flow rates (~ 18 sccm) and low oxygen partial pressures ($\sim 5\%$ O_2). The presence of a VO nano-crystalline phase embedded in the bulk amorphous matrix is believed to be the reason for the lower resistivity of the films deposited at these flow rates and oxygen partial pressures.

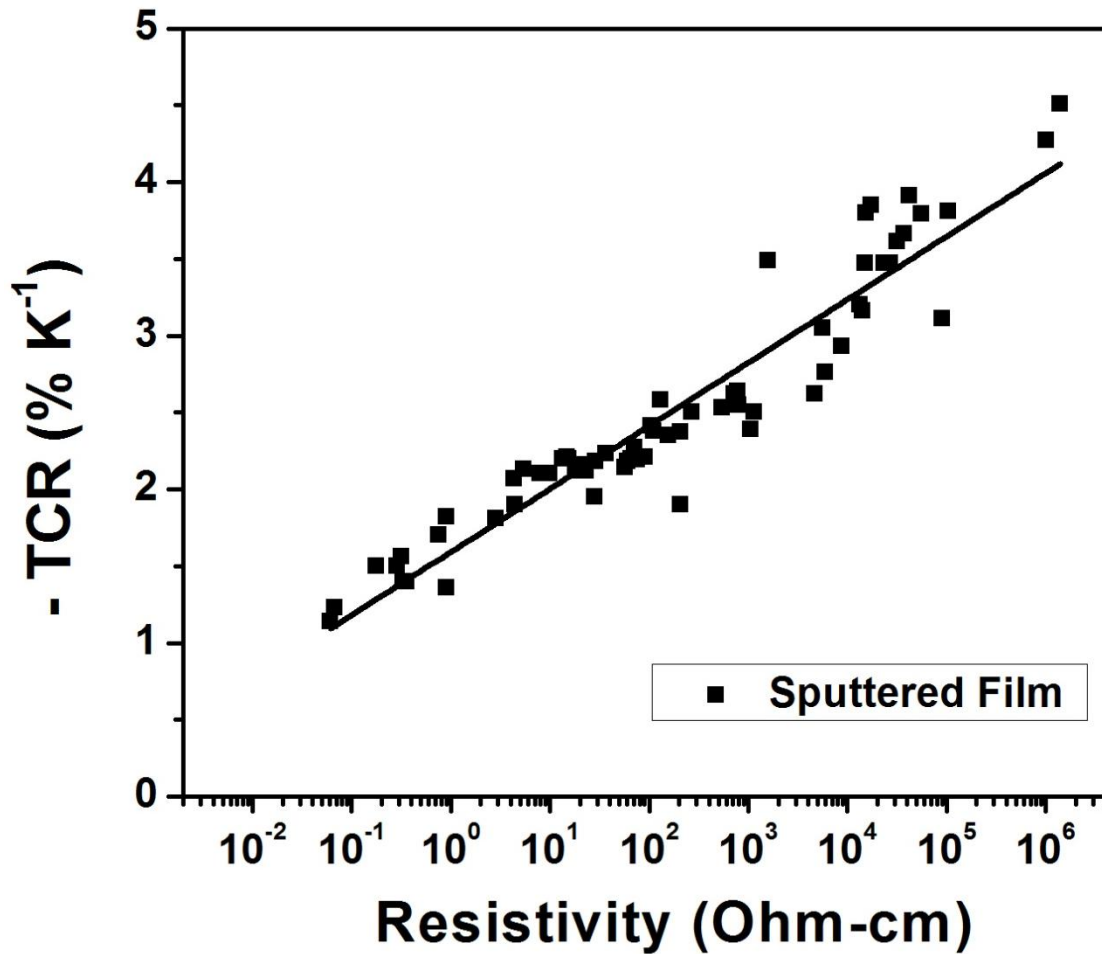


Figure 3-14: Relationship between TCR and resistivity of as-deposited films.

In comparison to the data published in various papers and patents, the TCR of these magnetron sputtered samples are slightly lower for any given resistivity. However, after taking a closer look at the published data and also talking to people from the industry, it may be that these variations arise mainly from the differences in the way TCR is calculated. The TCR values we calculated so far are an average value for the temperature range 25 – 100 °C. However the industry uses a localized TCR calculated at room temperature using the activation energy method as described below.

Resistivity of a material is given by the generic expression

$$\rho = \rho_o \exp\left(\frac{-E_a}{kT}\right) \quad (3.3)$$

When plotted on a semi-log scale, the slope of resistivity versus $1/T$ plot gives the activation energy. The TCR at any given temperature is calculated from this using the formula

$$TCR = \frac{-E_a}{kT^2} \quad (3.4)$$

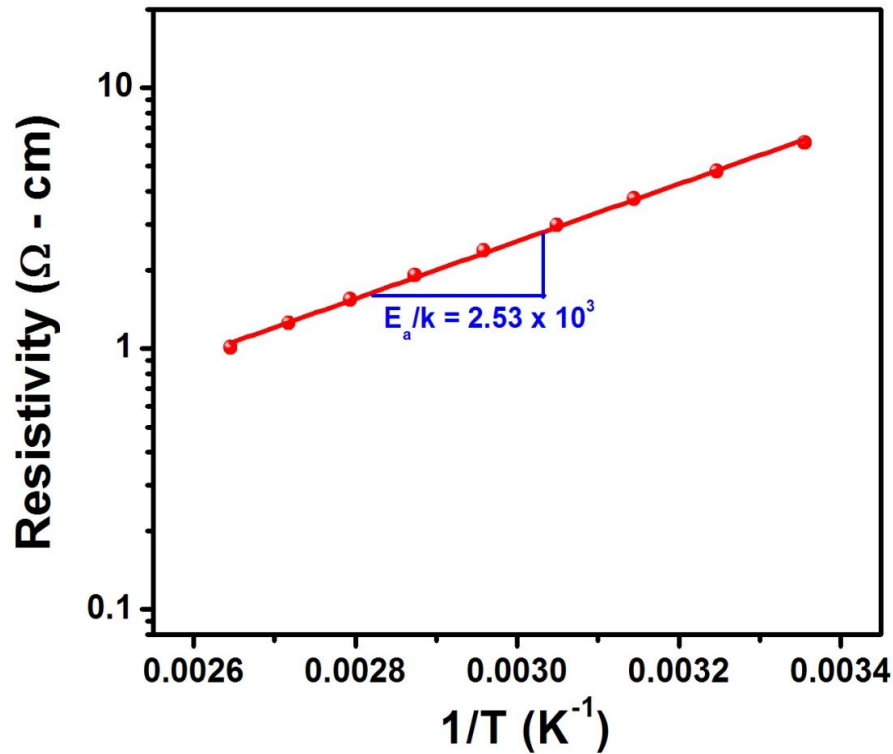


Figure 3-15: Plot of resistivity as a function of $1/T$.

The room temperature TCR values calculated by this formula were consistently higher by about 30%. As an example, for the data shown above, the TCR at room temperature comes out to be $-2.81\% \text{K}^{-1}$ while the TCR at 100°C is $-1.82\% \text{K}^{-1}$. The value obtained using our initial

method was -2.25 \%K^{-1} , which can best be described as an average value for this entire temperature range.

When these newly computed TCR values were plotted against some standard data from the literature, we found that there was a significant overlap. However, the data obtained by Wood [6] was still higher for certain resistivity ranges. Hence post-deposition processing was investigated as a means to enhance the TCR of these magnetron sputtered films.

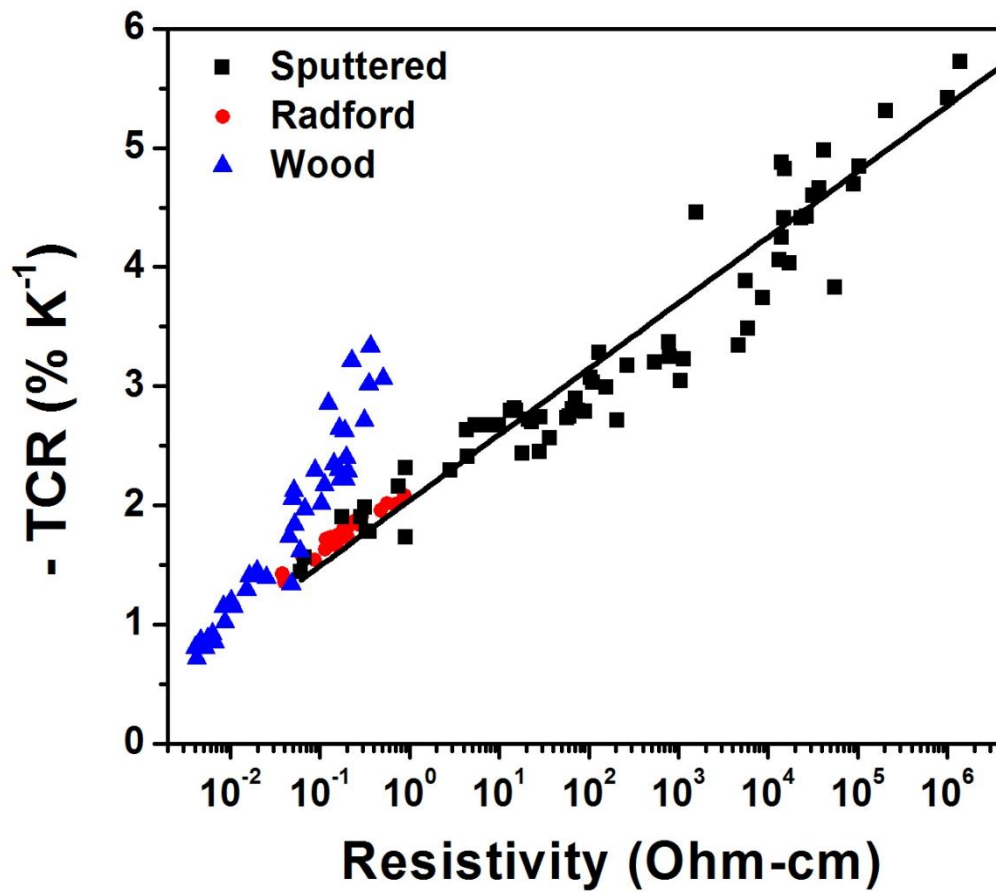


Figure 3-16: Comparison of TCR and resistivity of pulsed dc magnetron sputtered films to data published by Wood [6] and Radford [10].

Chapter 4

Post-deposition processing: Annealing

This chapter deals with how annealing can be used to improve the properties of vanadium oxide films for use in microbolometers. Two sets of annealing environments were explored – oxygen (oxidizing) and nitrogen (inert). Samples were annealed at four temperatures – 200, 300, 400 and 500 °C for varying time periods and the effects on electrical and structural properties were studied.

The experiments were initially performed on two samples whose TCR and resistivity values were of interest to the microbolometer industry – one deposited at 5% O₂ and the other at 7.5% O₂ with a total flow rate of 18sccm at 5 mTorr pressure. Both films exhibited linear I-V behavior and their room-temperature resistivities were measured to be 0.6 and 13 Ω-cm, with TCRs of -1.6% and -2.2% respectively. Once the optimal anneal conditions were identified, the experiment was performed on a wide range of samples to establish the versatility and reproducibility of the process.

4.1 Oxygen Annealing

4.1.1 Electrical Properties

Annealing in oxygen caused large variations in the electrical properties of the film as shown in Fig. 4-1. The sample deposited at 5mTorr pressure with 5% O₂ at 18 sccm had an initial resistivity of 0.6 Ω-cm with a TCR of -1.6%. The 200 °C anneal caused the resistivity to fluctuate a little bit around this initial value while the TCR increased slightly. However, when annealed at 300 °C, the resistivity dropped by over an order of magnitude, and the *log* (resistivity)

versus T curve is no longer linear, instead displaying a small change in slope at around $67\text{ }^{\circ}\text{C}$, indicative of the metal-insulator transition associated with VO_2 films. Interestingly, the measured room-temperature resistivities of the films seem low in comparison to the reported resistivity values of VO_2 thin films in literature [69]. This suggests that the films are not purely VO_2 and very likely contain a mixture of VO_x phases, as is evident from the x-ray diffraction data shown in Fig. 4-3. It is surmised that this large drop in resistivity might be due to some kind of ordering in the film as crystalline domains of various VO_x phases begin to coalesce. Unfortunately, the high TCR values obtained for these $300\text{ }^{\circ}\text{C}$ oxygen annealed films are not useful since the TCR is not constant over the temperature range of interest.

When annealed at $400\text{ }^{\circ}\text{C}$, the resistivity started to increase drastically, and ended up a few orders of magnitude higher than that of the starting material. Also, the $\log(\text{resistivity})$ versus T plot became linear again, with a TCR of $\sim -2.8\%$. This is because the more stable higher oxides of vanadium (mainly V_2O_5), which are less conductive, begin to form around that temperature. The resistivity and TCR do not change much in going from $400\text{ }^{\circ}\text{C}$ to $500\text{ }^{\circ}\text{C}$ anneal.

For the sample deposited at 7.5% O_2 and annealed under the same conditions, a very similar trend was observed. There were some minor variations, however. For example, the drop in resistivity after the $300\text{ }^{\circ}\text{C}$ anneal was much greater than that for the 5% O_2 sample. Also, the film had non-linear $\log(\text{resistivity})$ vs. T characteristic after the 10 min anneal at $400\text{ }^{\circ}\text{C}$, though it eventually became linear after the 30 min anneal. These variations are attributed to the differences in the initial amount of oxygen present in the samples. But overall, the general trend observed was the same.

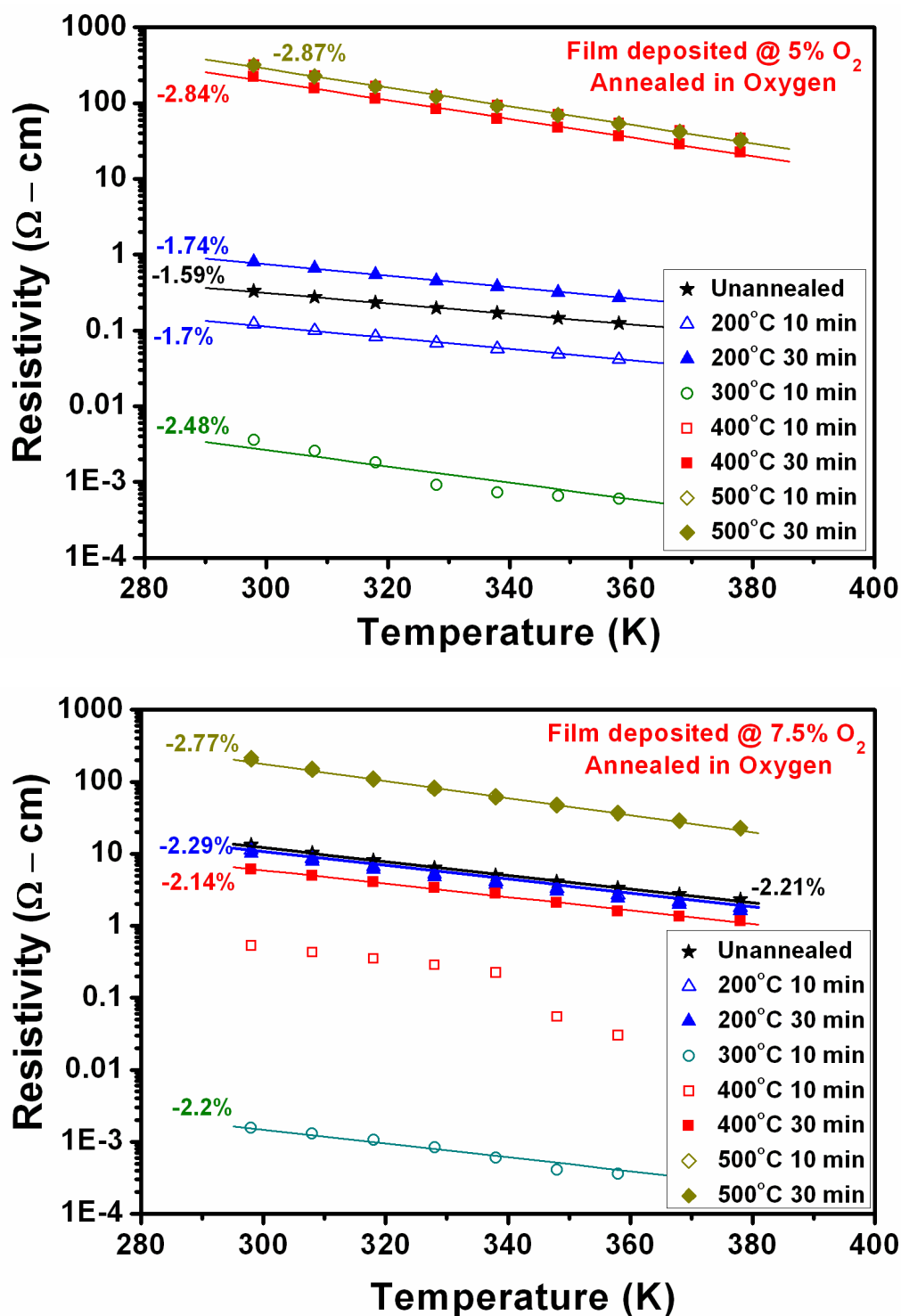


Figure 4-1: Resistivity and TCR values as a function of annealing temperature for films annealed in oxygen atmosphere. The resistivity drops for the 200 and 300 °C anneals, but starts to increase after the 400 and 500 °C anneals. The data points corresponding to 400 °C anneal of the 7.5% sample are not clearly visible as they overlap with the 500 °C ones.

Fig. 4-2 shows the TCR and resistivity of the oxygen annealed films plotted on the universal resistivity vs. TCR curve. We can clearly see that for any given resistivity, the TCR of the annealed film is higher.

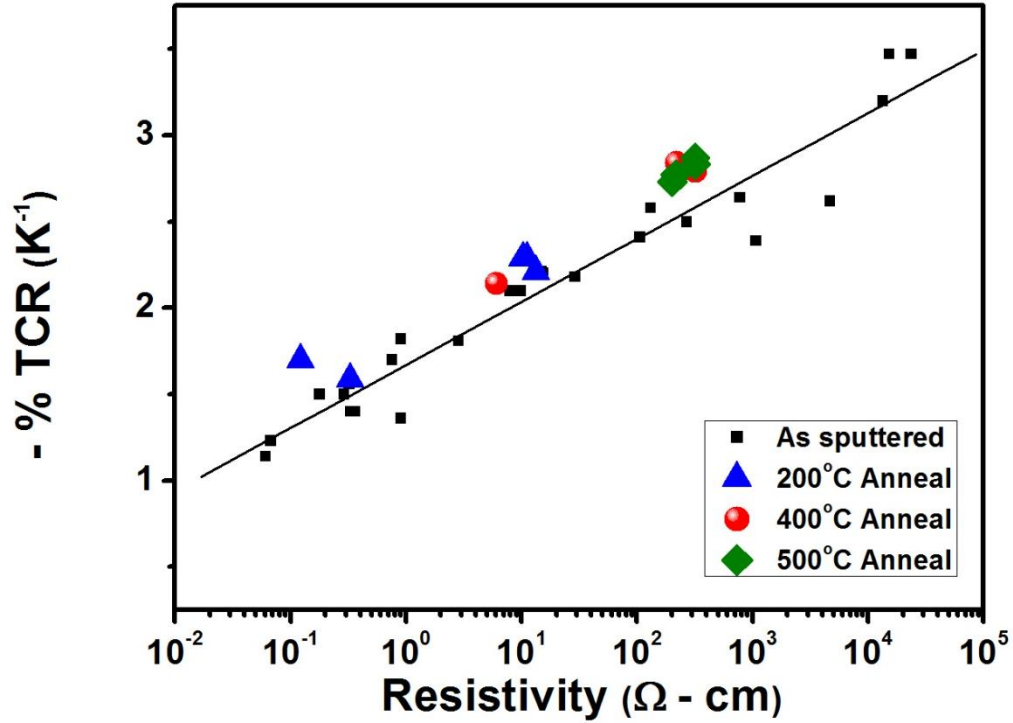


Figure 4-2: Comparison of the TCR of oxygen annealed films with as-deposited films.

4.1.2 Structural Properties

Fig. 4-3 shows the x-ray diffraction patterns of samples annealed in oxygen for 30 min. at various temperatures. The as-deposited sample was mostly x-ray amorphous with a couple of low intensity peaks corresponding to the fcc VO phase. Annealing the film at 200 °C did not cause the spectra to change by much. But after the 300 °C anneal, some low intensity peaks, possibly corresponding to V_2O_3 and V_2O_5 phases, start to show up, confirming the presence of multiple phases in the thin film. But there was no signature of the VO_2 phase, which was

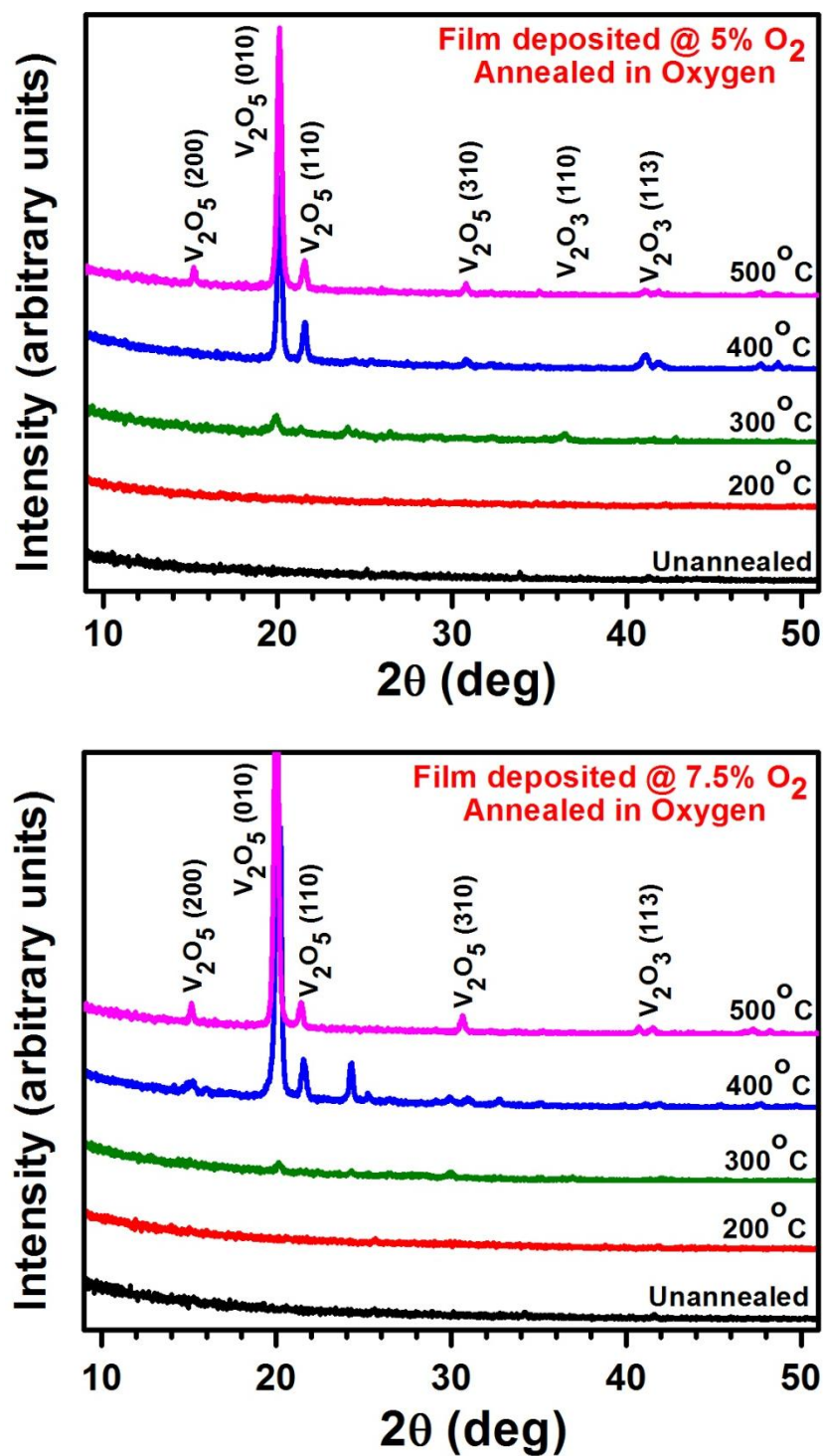


Figure 4-3: XRD spectra of the samples deposited at 5% and 7.5% O_2 and annealed in oxygen ambient. Peaks corresponding to higher oxides of vanadium become prominent for the 400 and 500 °C anneals.

expected based on the metal-insulator transition behavior observed in the electrical properties. We suspect the reason for this is that VO_2 might nucleate as small micro-crystalline domains, scattered through the film, and hence difficult to be detected by XRD. The 400 °C annealed sample clearly showed that higher oxides of vanadium (mainly V_2O_5) begin to form, and they continue to grow at 500 °C too, as indicated by the increase in the x-ray peak intensity.

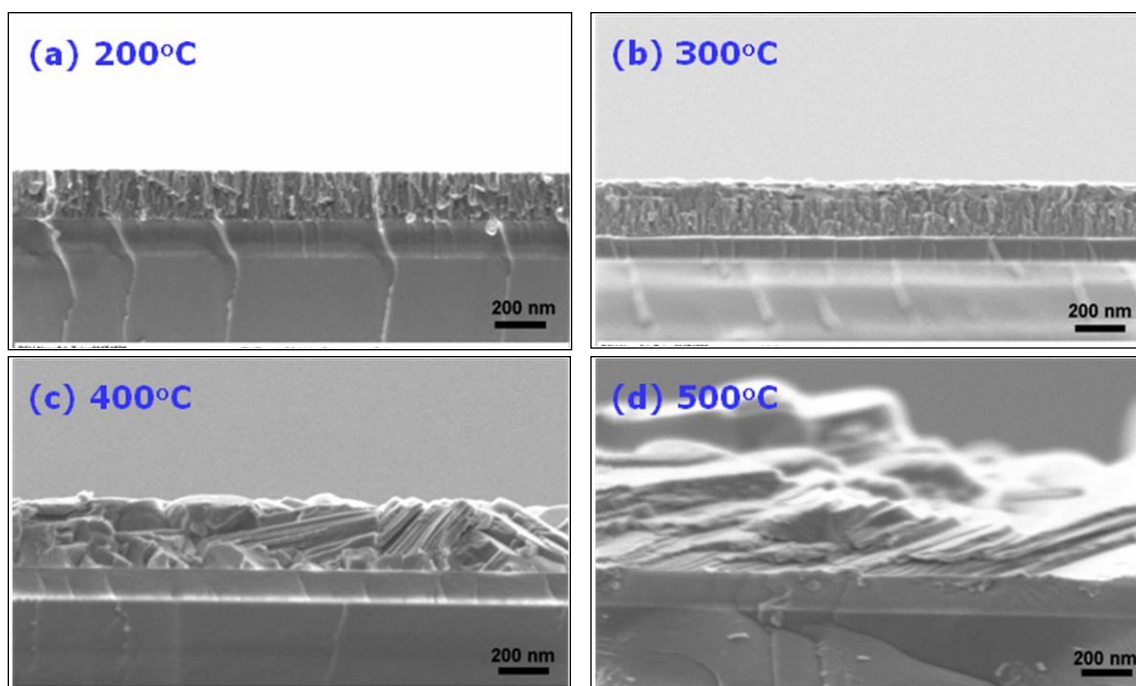


Figure 4-4: Cross-sectional FESEM images of the film deposited at 5% O_2 after annealing for 30 min at various temperatures in oxygen atmosphere. We can clearly see the plate-like structure of V_2O_5 formed after annealing at 400 and 500 °C.

Cross-sectional FESEM images (Fig. 4-4) were taken to see how the microstructure changes with annealing. The as deposited film was columnar, as discussed in Chapter 3. 200 °C anneal did not cause any change to the columnar structure. And rather surprisingly, the 300 °C anneal also did not affect the columnar structure. This is surprising because we see significant changes in the electrical properties and diffraction patterns, but virtually none in the cross-sectional SEM. At 400 °C, the atoms have clearly rearranged to form a plate-like structure, which

is one of the characteristic forms of existence of the V_2O_5 phase [70]. These plates grow in size and become more prominent after the 500 °C anneal.

The changes in morphology and structure are further corroborated by the AFM images, shown in Fig. 4-5. The initial as-deposited film had an apparent grain size of ~40 nm with an RMS roughness of 1.8 Å. The 200 °C anneal did not change the film much and it has almost the same grain size and roughness as the unannealed film. The films exhibited large changes in the surface morphology as the annealing temperature increased further. The apparent grain size gradually increases from ~40 nm for the 200 °C annealed film to ~500 nm for the 500 °C anneal. The RMS roughness also increases from 1.8 Å to 5.4 Å to 6.8 Å and finally to 72.1 Å at 500 °C. The shapes of the grains also change, ranging from small circular grains at 200 °C to more rectangular plate-type grains at 300 °C and finally to much larger more circular plate-type grains at 500 °C.

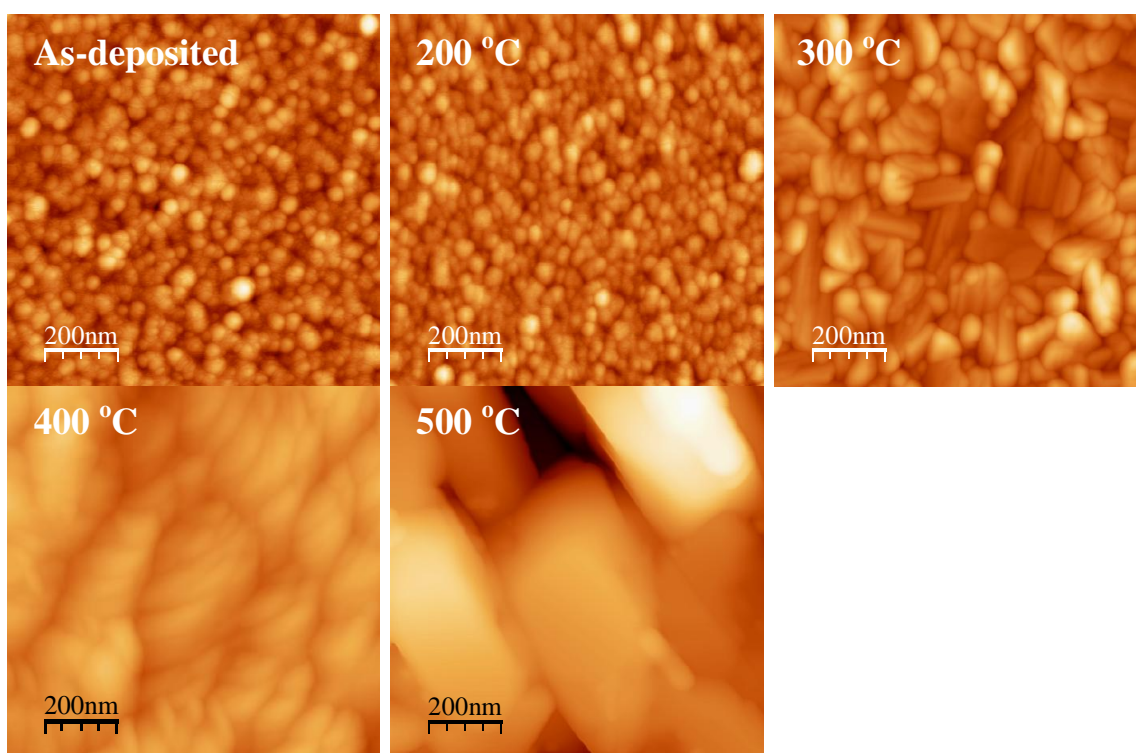


Figure 4-5: AFM images of samples annealed in oxygen at the indicated temperatures.

The annealed films were next examined using Raman spectroscopy to further investigate the apparent morphological and compositional changes that occur. The Raman spectra of the unannealed film and the oxygen-annealed films are displayed in Fig. 4-6. The as-deposited, unannealed film has two different broad bands present, one at 285 cm^{-1} which is probably due to a VO bend and a second band centered near 885 cm^{-1} which is preliminarily assigned to a VO stretch mode [Error! Bookmark not defined.52]. The broadness of the two observed modes, suggests that the film is amorphous, in corroboration with the XRD results. The sample annealed at $200\text{ }^{\circ}\text{C}$ has features very similar to those observed in the unannealed film, indicating that the film has not changed much. However, at $300\text{ }^{\circ}\text{C}$, a drastic change is observed in the Raman spectrum. The spectral features sharpen and a multitude of new peaks appear. This change is concurrent with the large drop in resistivity observed in Fig. 4-1. Preliminary analysis suggests that some crystalline VO_2 is present in this film along with smaller amounts of crystalline V_2O_5 and other unidentified crystalline VO_x phases. The Raman spectra clearly show that near $300\text{ }^{\circ}\text{C}$, the VO_x thin films undergo a distinct transition from amorphous to a more crystalline character consisting of various VO_x phases. The crystalline VO_2 features, most notably the peak near 620 cm^{-1} , are not present in the $400\text{ }^{\circ}\text{C}$ and $500\text{ }^{\circ}\text{C}$ samples. The concurrent increase in resistivity at $400\text{ }^{\circ}\text{C}$ and disappearance of the crystalline VO_2 features in the Raman spectrum, suggest that at $300\text{ }^{\circ}\text{C}$, the VO_2 phase in particular, plays an important role in the observed dramatic change in resistance. At $500\text{ }^{\circ}\text{C}$, all the observed features can be assigned solely to crystalline V_2O_5 , in agreement with the results obtained from the XRD data and SEM images.

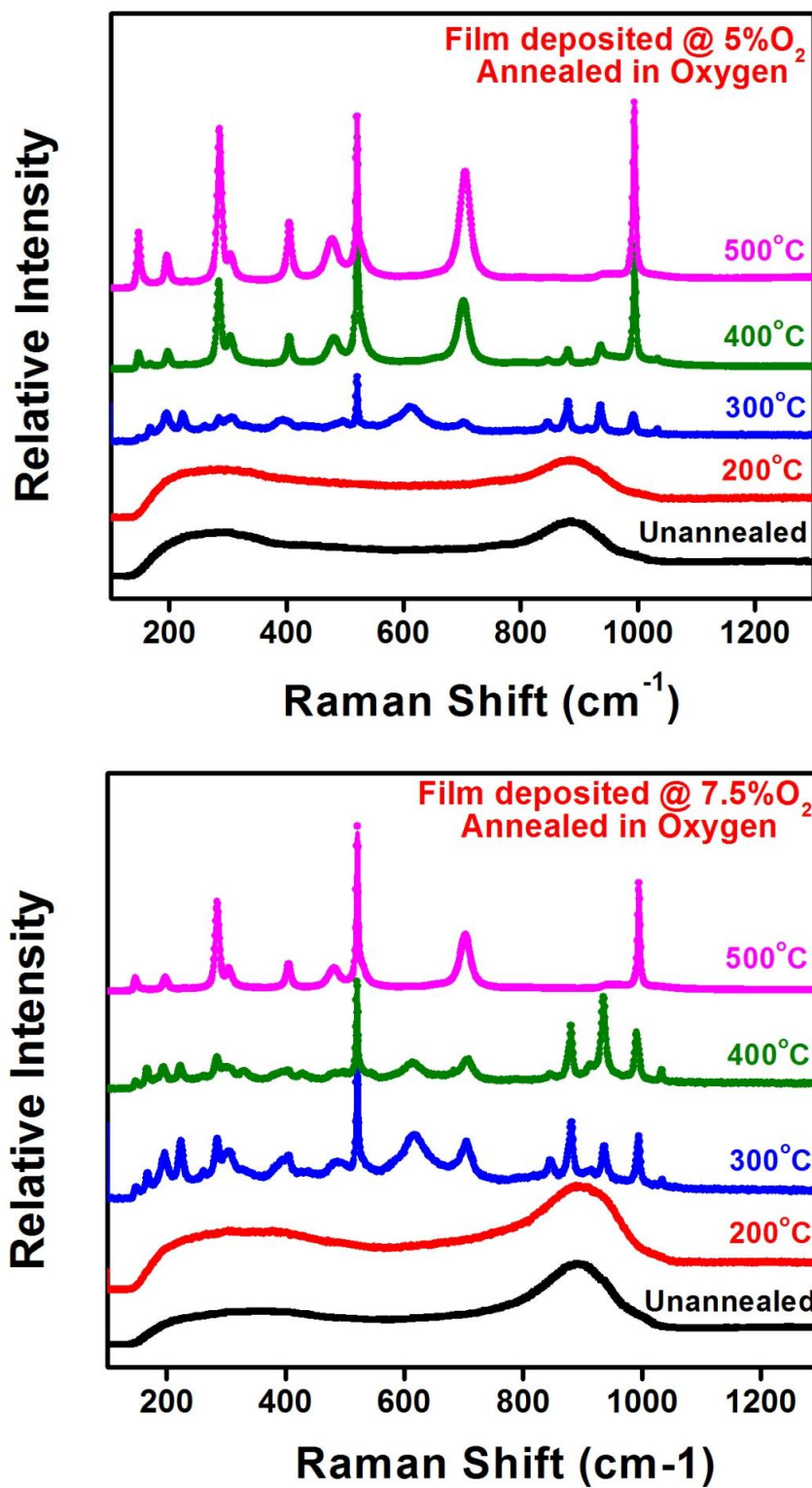


Figure 4-6: Raman spectra of 5% and 7.5% O₂ deposited films as a function of annealing temperature in an oxygen atmosphere. Note the drastic change in the spectra beginning at 300 °C, correlating with the observed drop in resistivity.

From these results, it can clearly be seen that annealing in oxygen environment causes the films to oxidize to various higher oxides of vanadium depending on the anneal temperature. This causes drastic changes in the resistivity and TCR of the film as summarized in Fig. 4-7. The drop in resistivity at 300 °C is not clearly understood at this point of time. It is surmised to be due to some kind of ordering in the film as crystalline domains of various VO_x phases begin to coalesce. The temperature and time are not sufficient to drive these phases to their stable forms. Hence it can be considered as a mixture of several meta-stable phases, including VO_2 , which gives rise to the metal-insulator transition behavior. Beyond 400 °C, the stable V_2O_5 phase seems to dominate with high resistivity and high TCR.

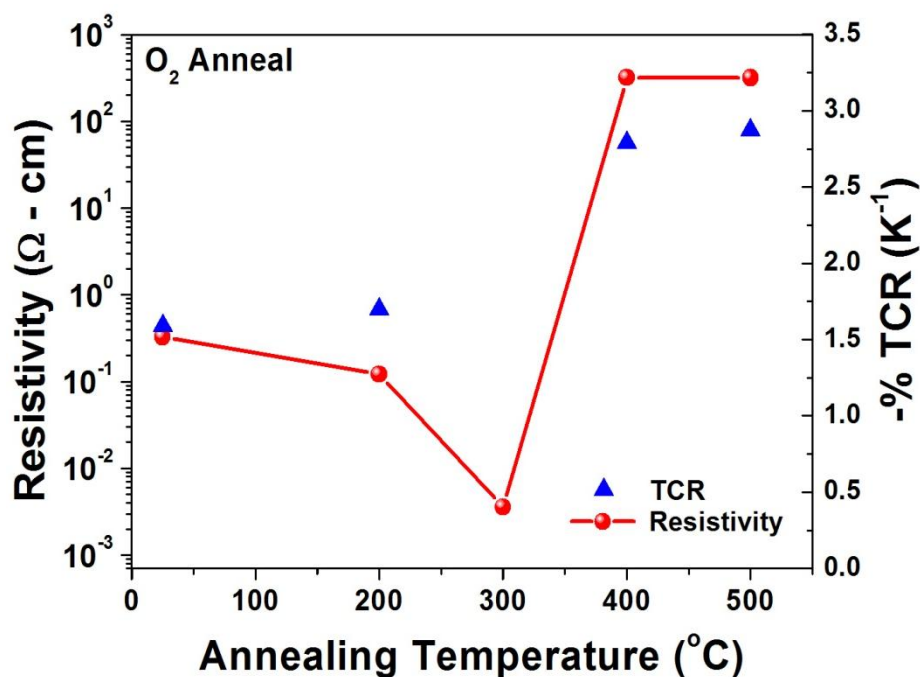


Figure 4-7: Summary of changes in electrical properties as a result of annealing in oxygen at various temperatures.

4.2 Nitrogen Annealing

4.2.1 Electrical Properties

The nitrogen annealed films exhibited a different trend compared to the oxygen annealed ones. Here the resistivity decreases monotonically with temperature. This might be due to increasing loss of weakly bound oxygen in the films to the atmosphere as the annealing temperature is raised, leading to an increase in the metallic nature of the VO_x films. Resistivity and TCR values as a function of anneal temperature is shown in Fig. 4-8. The anneal at 200 °C did not change the resistivity significantly, though the TCR does increase by ~10%. However, the films annealed at 300 °C show a resistivity drop of almost an order of magnitude. This is similar to the drop that was observed at 300 °C in the oxygen annealed films, though in the case of the nitrogen, no metal-insulator transition is observed and the TCR remains constant over the observed temp range. The TCR is actually found to increase by ~ 20% for the 5% O_2 sample, though it remains nearly unchanged for the 7.5% O_2 sample. Nevertheless, in both cases, this combination of high TCR with low resistivity is superior to that of the as-deposited films.

The films become highly conductive with continued annealing up to 400 °C in a nitrogen atmosphere. A 10min anneal for the 7.5% sample and a 30 min anneal for the 5% sample resulted in the *log* (resistivity) vs. temperature plot becoming non-linear, i.e. each film exhibits the metal-insulator transition commonly observed in crystalline VO_2 . This same effect was observed in the oxygen annealed films, albeit at 300 °C. It appears that under both annealing conditions, the as-deposited films gravitate towards forming crystalline VO_2 domains. The transition occurs at a lower temperature in case of the oxygen-annealed samples, apparently due to the presence of extra oxygen. However, the extra oxygen also tends to drive the oxygen-annealed films towards forming the more stable V_2O_5 oxide. In both cases, we observe that transitioning from an

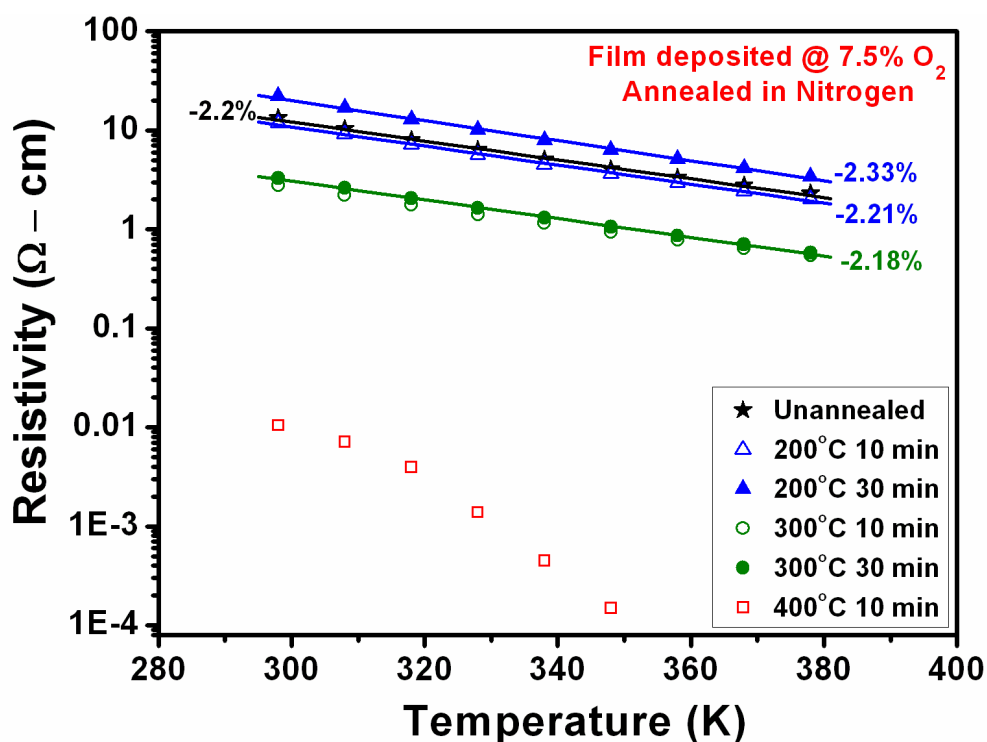
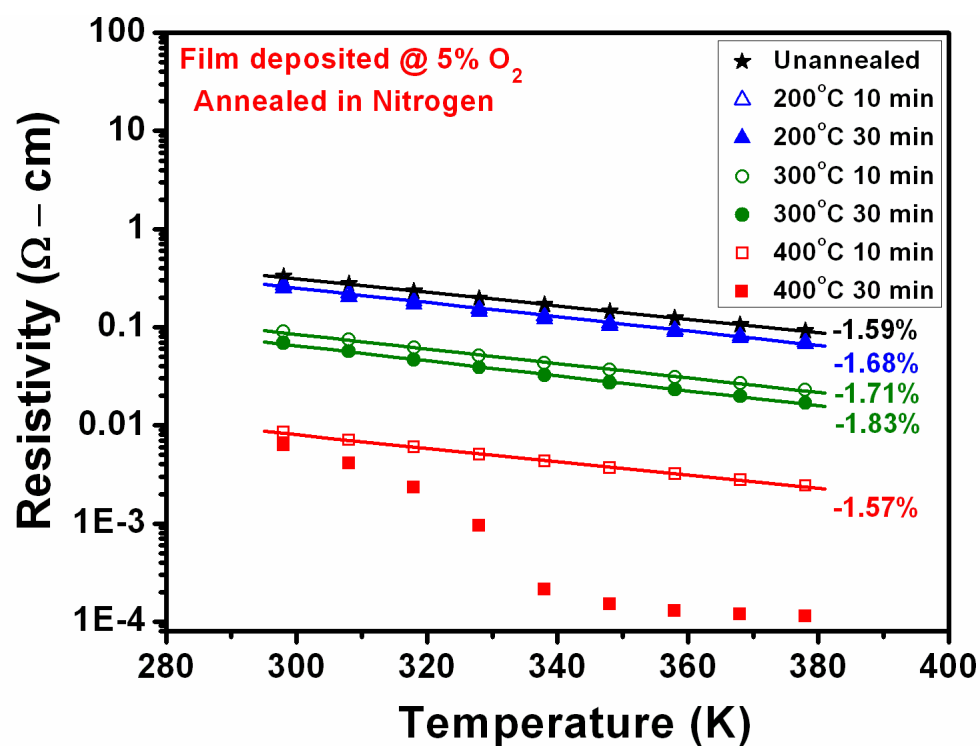


Figure 4-8: Resistivity and TCR values as a function of annealing temperature for films annealed in a nitrogen atmosphere. The film resistivity decreased monotonically with increasing annealing temperatures, but the TCR still remained reasonably high.

amorphous VO_x film to a more ordered phase appears to play an important role in lowering the overall film resistivity while maintaining or even increasing the TCR of the film. Fig. 4-9 shows the overall effect of the nitrogen-annealed films in terms of TCR and resistivity in comparison to the as-deposited films. Here again, as with the oxygen-annealed films, the TCRs obtained for annealed films are much higher than those of the as-deposited films with similar resistivity.

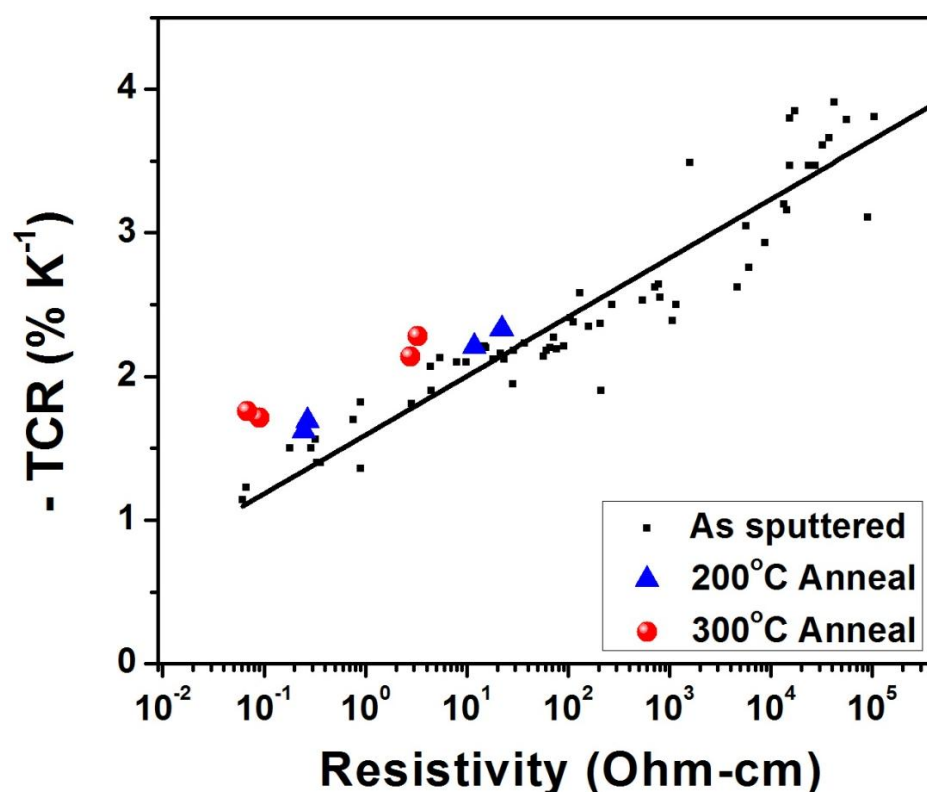


Figure 4-9: Summary of resistivity vs TCR for nitrogen annealed samples.

4.2.2 Structural Properties

The x-ray diffraction spectra of the samples annealed in nitrogen are shown in Fig. 4-10. The as-deposited 5% O_2 sample has distinct peaks corresponding to the fcc VO phase. These peaks are retained even after the 200 and 300 °C anneals, indicating that the structure of the films do not change much with annealing at these temperatures. But after the 400 °C anneal, a new

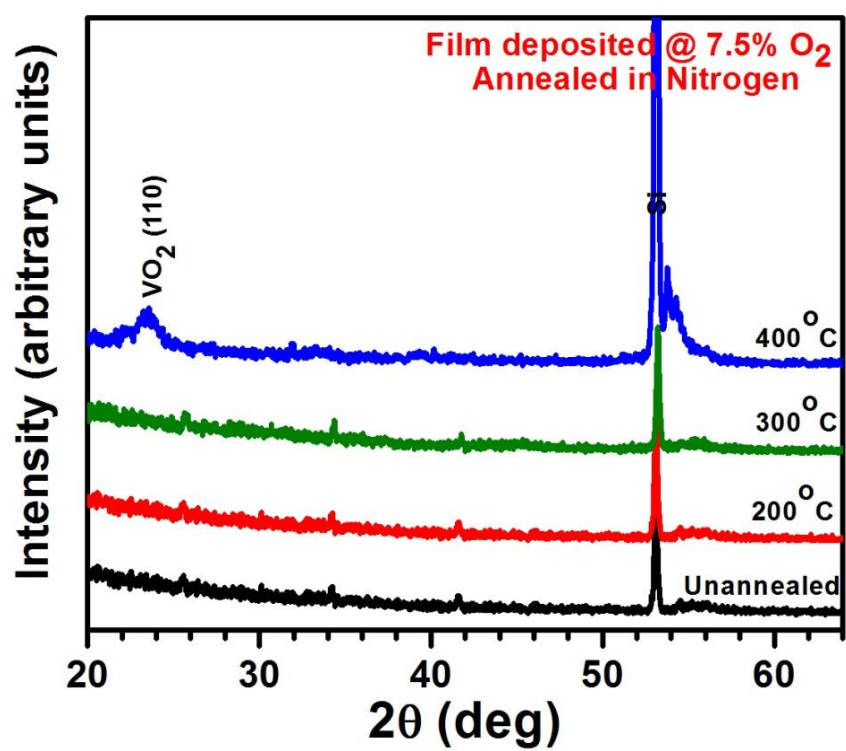
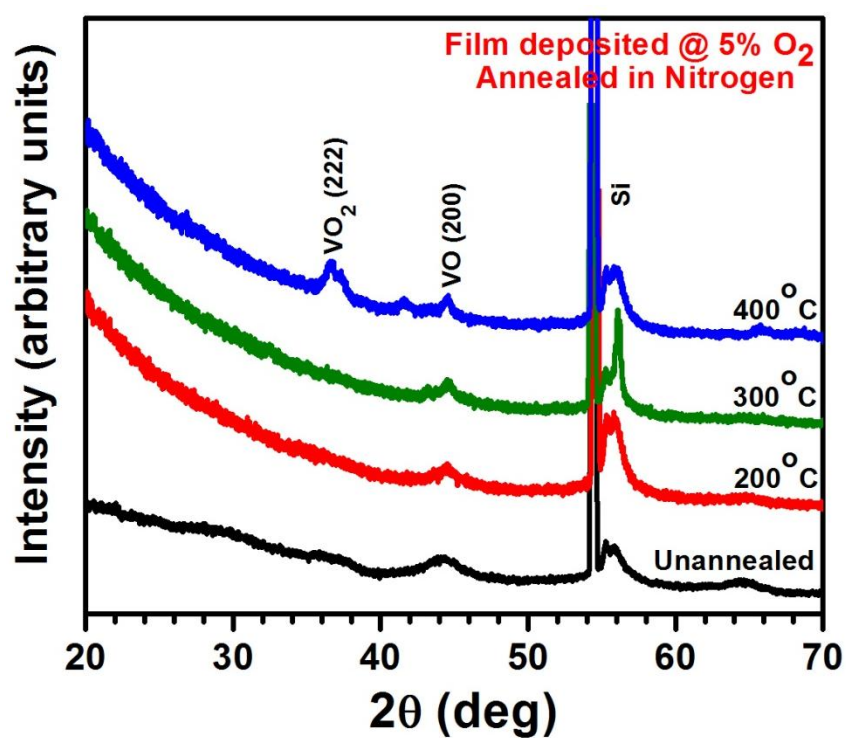


Figure 4-10: X-ray diffraction spectra of films annealed in nitrogen.

peak shows up, corresponding to the VO_2 phase. This is consistent with the observation of the metal-insulator transition behavior observed in the electrical properties. The 7.5% O_2 sample also behaved in a similar fashion, except that the fcc VO phase was not very prominent in both the as-deposited as well as the 200 and 300 °C annealed samples.

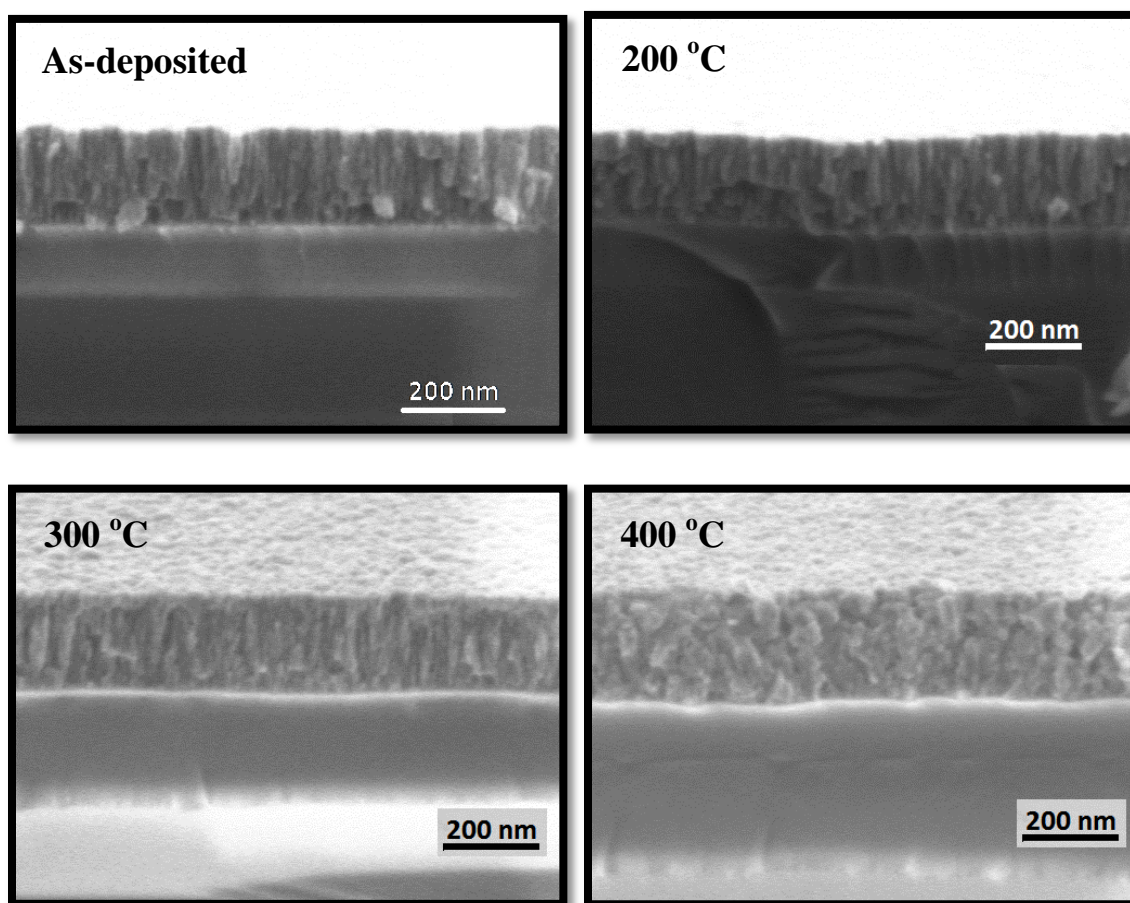


Figure 4-11: Cross-sectional SEM images of the sample deposited at 5% O_2 and annealed in nitrogen atmosphere.

Cross-sectional SEM images revealed that the columnar morphology was retained even after the annealing (Fig. 4-11). These results are supported by the AFM images displayed in Fig. 4-12, where we observe that the grain size and RMS roughness of the films does not change

significantly as the annealing temperature is increased. This is in marked contrast to the oxygen-annealed series, Fig. 4-5, where large structural and morphological changes were seen with increasing temperature due to the formation of V_2O_5 .

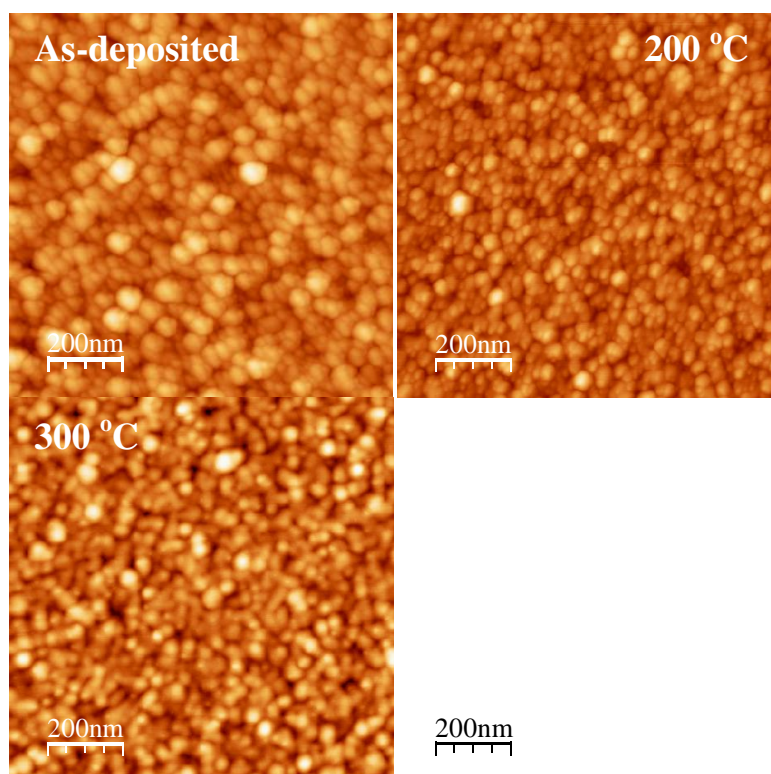


Figure 4-12: AFM images of the sample deposited at 5% O_2 and annealed in nitrogen atmosphere at the indicated temperatures.

The Raman spectra of the samples annealed in nitrogen are displayed in Fig. 4-13 and they also indicate a transition to crystalline VO_2 at 400 °C. The as-deposited film has two broad peaks located at 365 and 890 cm^{-1} indicating that the film is mostly amorphous vanadium oxide. Annealing the film in a nitrogen atmosphere at 200 °C has little effect on the position of the bands, however the peak at 890 cm^{-1} is slightly lower in intensity. The decrease in the relative intensity of the high frequency to the low frequency peak continues for the 300 °C annealed film

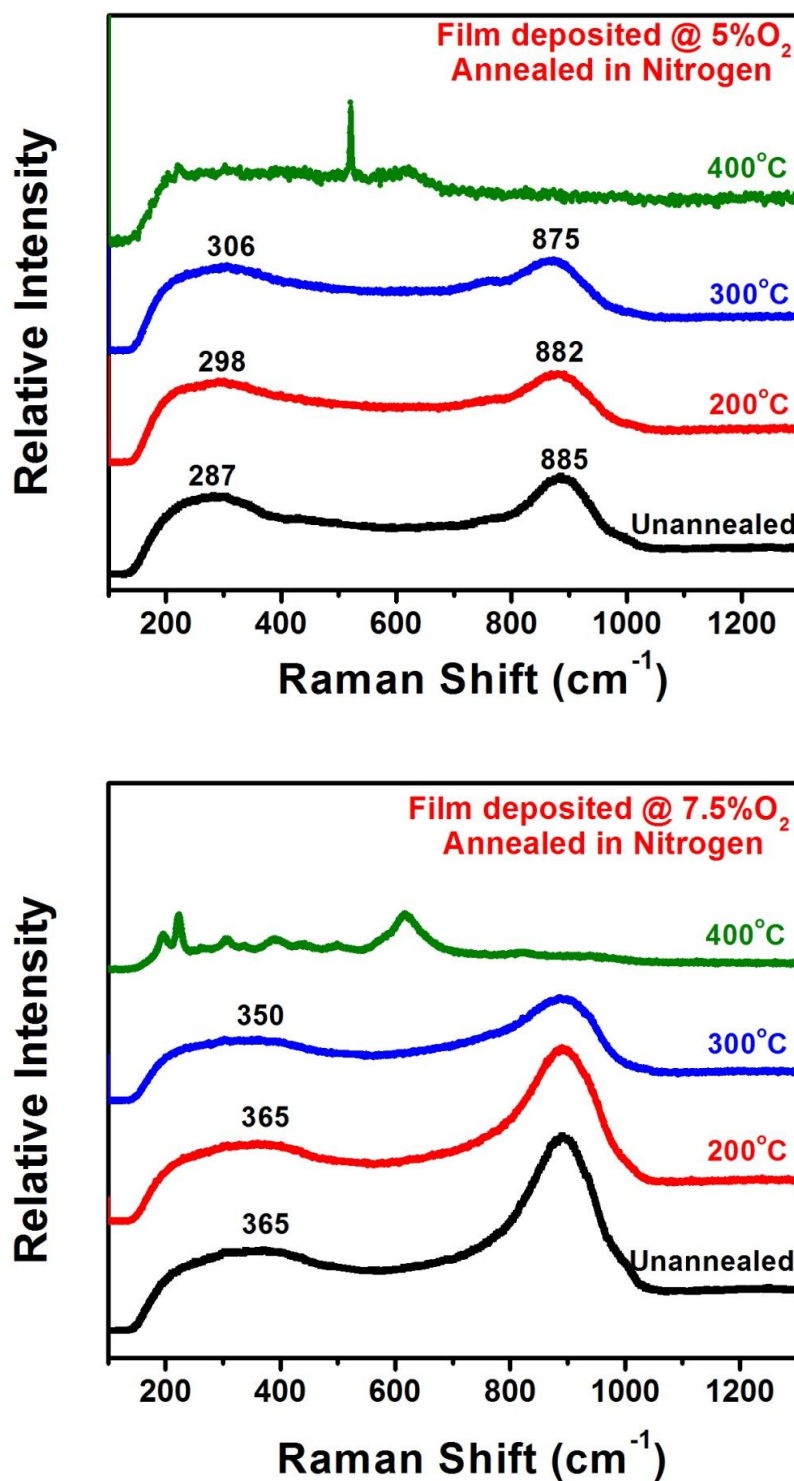


Figure 4-13: Raman spectra of 5% and 7.5% O₂ films as a function of annealing temperature in a nitrogen atmosphere. The as-deposited, 200 °C, and 300 °C samples exhibit broad amorphous VO_x features. At 400 °C, the spectrum develops sharper feature characteristics of crystalline VO₂.

and suggests that the amount of V^{4+} present in the sample decreases. This indicates that the local stoichiometry changes slightly, even though the overall stoichiometry remained the same as measured by RBS. At 400 °C, the film appears to develop some micro-crystalline domains of VO_2 as evidenced by the sudden appearance of the distinctive spectral features of crystalline VO_2 in the Raman spectrum. No other features attributable to other VO_x phases are present in the Raman spectrum at 400 °C. This assignment is consistent with the observation of a strong insulator to metal transition at ~340 K as seen in the resistivity vs. temperature plot shown in Fig. 4-8. This is in contrast to the 300 °C oxygen annealed film spectrum, which displayed features due to V_2O_5 and other unassigned VO_x phases in addition to VO_2 .

Transmission electron microscopy images were taken to see if annealing has caused any changes to the microstructure of the film. The selected area diffraction patterns of the film deposited at 5% O_2 and annealed at 300 °C is shown in Fig. 4-14. The diffraction pattern matches very well with the fcc VO phase. The slight broadening in the reflection rings is due to small size of the nanocrystallites. There was also a diffused ring present, indicating the presence of an amorphous phase. When this was compared to the diffraction pattern of the unannealed film, they matched exactly (Fig. 4-15), suggesting no apparent change in the crystal structure.

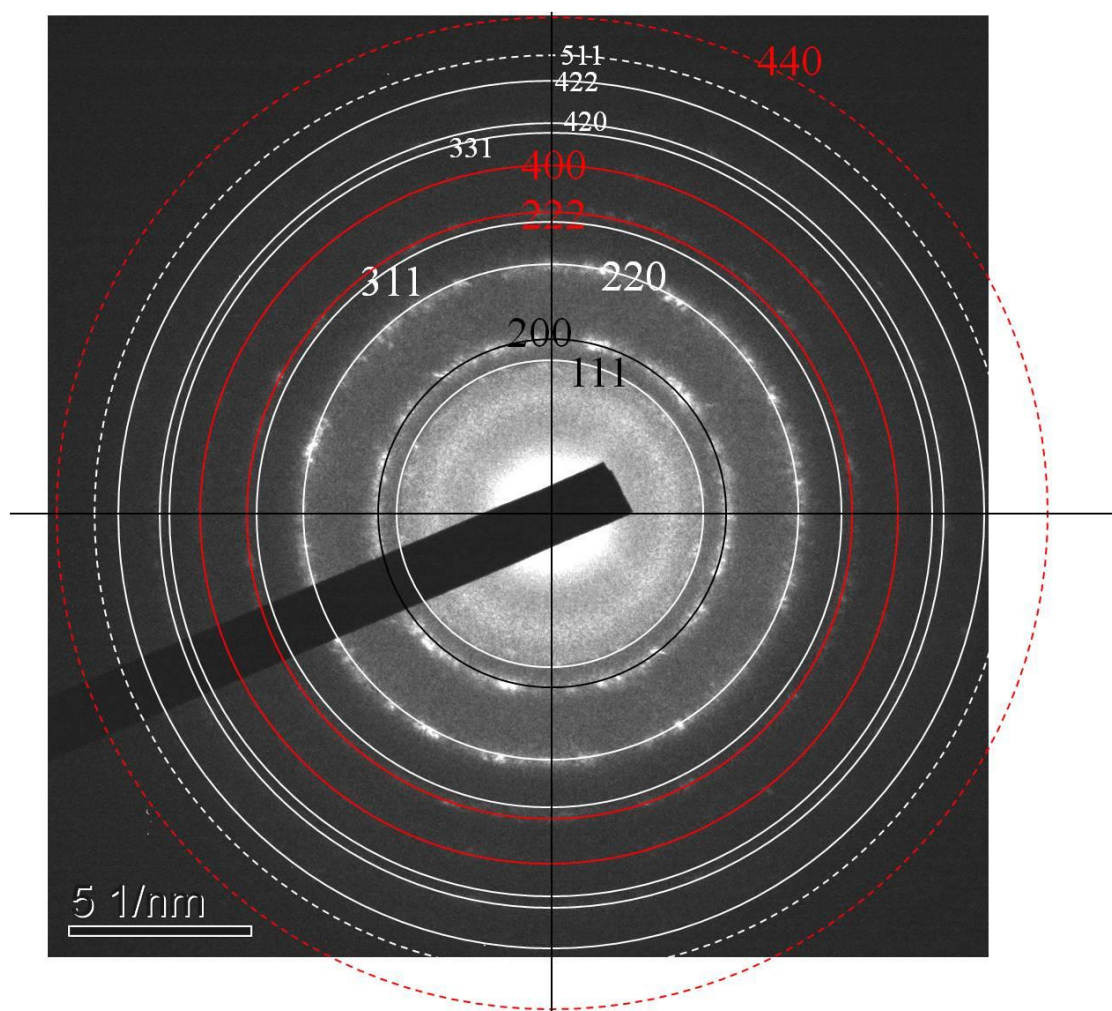


Figure 4-14: Selected area diffraction pattern of the film deposited at 5 mT pressure, 5% O₂ and annealed in nitrogen at 300 °C.

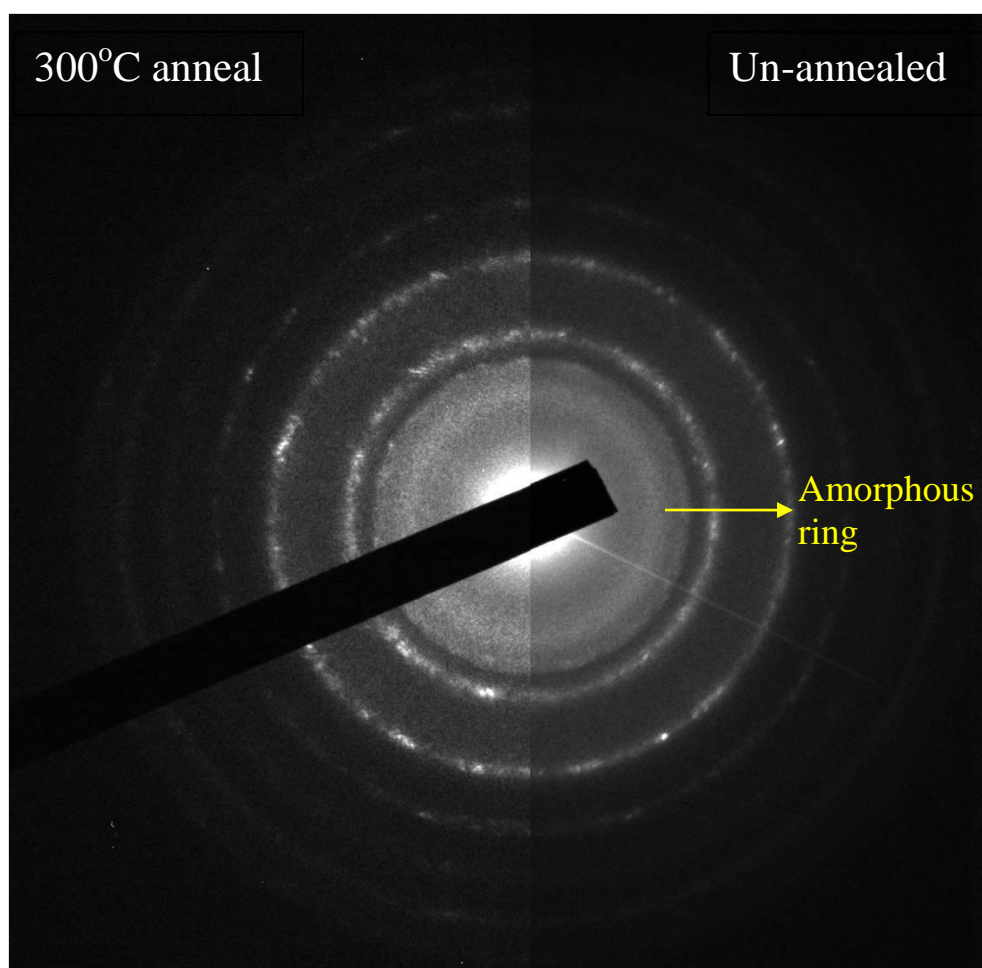


Figure 4-15: Comparison of the selected area diffraction pattern of the as-deposited film and the film annealed at 300 °C.

Dark-field images (Fig. 4-16 and 4-17) revealed that there are a lot of nano-twins [71] present in the sample, with a spacing of 1-2 nm. These nano-twins are speculated to be a low-resistivity phase that has a major contribution to the conduction. But they are present in both the annealed and unannealed samples. Also, there is significant porosity in the samples before and after annealing, observable, but difficult to quantify by TEM. Overall, samples before and after annealing look essentially the same!

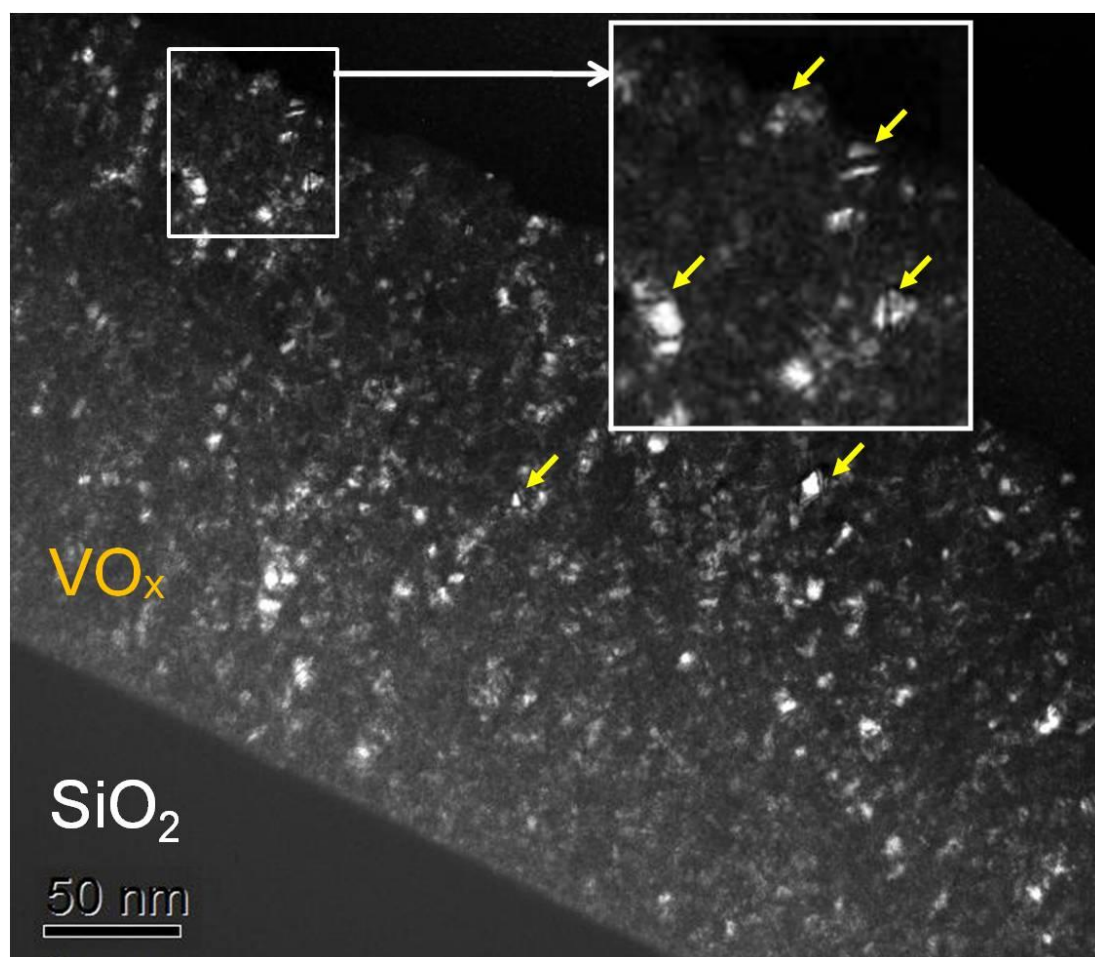


Figure 4-16: Dark-field image of the annealed sample showing micro-twins.

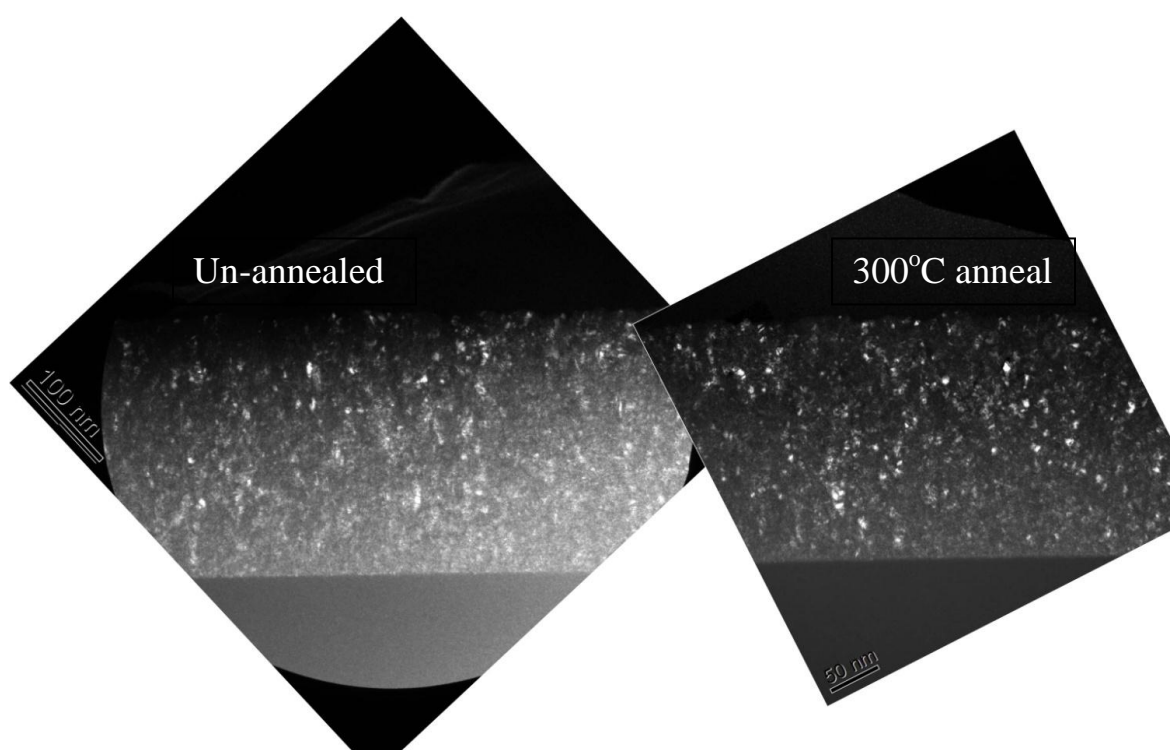


Figure 4-17: Comparison of the dark-field images of as-deposited and annealed sample.

Electron Energy Loss Spectroscopy (EELS) was performed using TEM in order to obtain information about the valence state of vanadium in these samples. Comparison of the EELS spectra of the as-deposited and the annealed sample is shown in Fig. 4-18. There was no difference observed in the Vanadium L_3 and Oxygen K edges, indicating that there is no change in the local chemistry or structure. When mapped against various vanadium oxide standards, it was found that the position of the oxygen K edge lies in-between that of V_2O_3 and VO_2 phases.

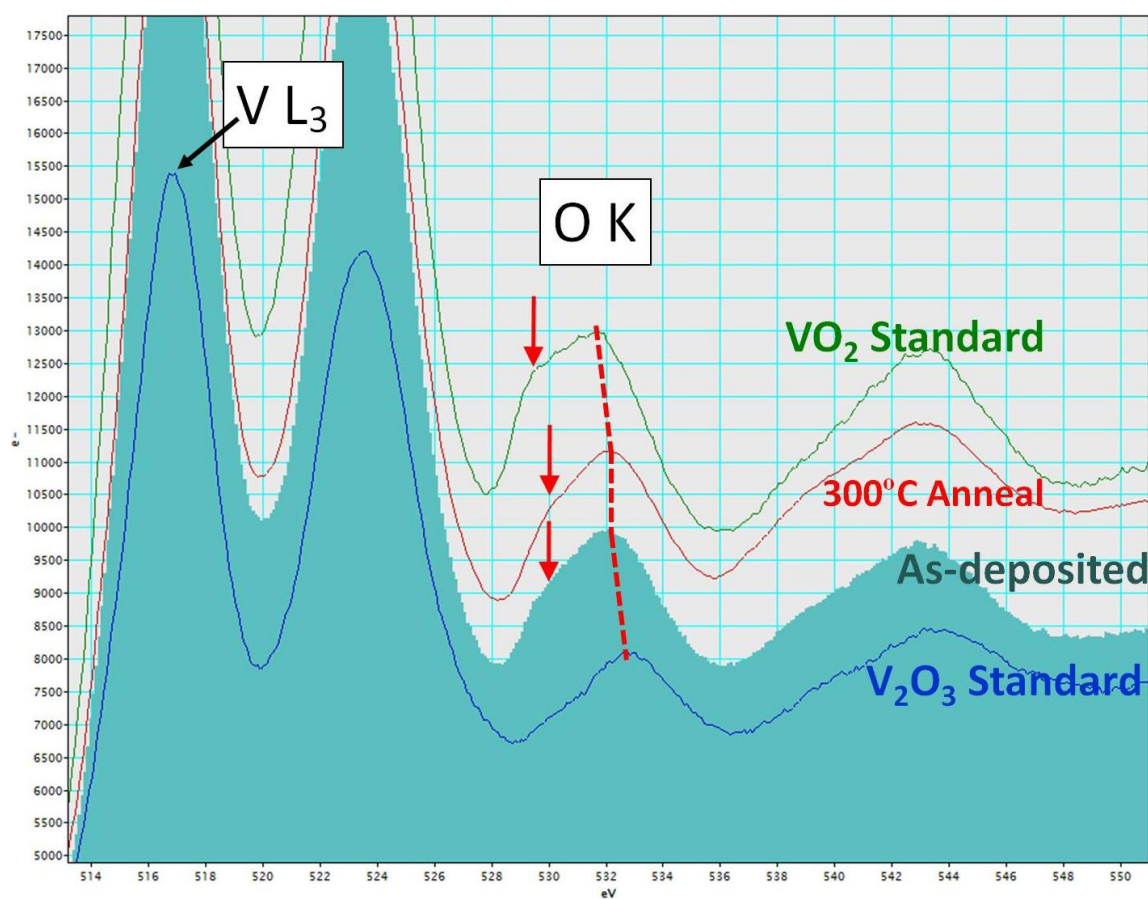


Figure 4-18: Comparison of EELS of the 5% O_2 sample before and after annealing in nitrogen at 300 °C.

EEL spectra were also collected on different regions of the film to compare between the bulk amorphous phase and the nano-twinned regions. It can clearly be seen from the Fig. 4-19 that the peak of the O-K edge of the nanocrystalline region shows an increased chemical shift (ΔE_1) and decreased energy span (ΔE_2) as compared to that of the amorphous phase. This indicates that the amorphous phase is richer in oxygen content than the nano-crystalline phase. Further EELS revealed that the nanocrystalline phase has stoichiometry closer to that of VO standard.

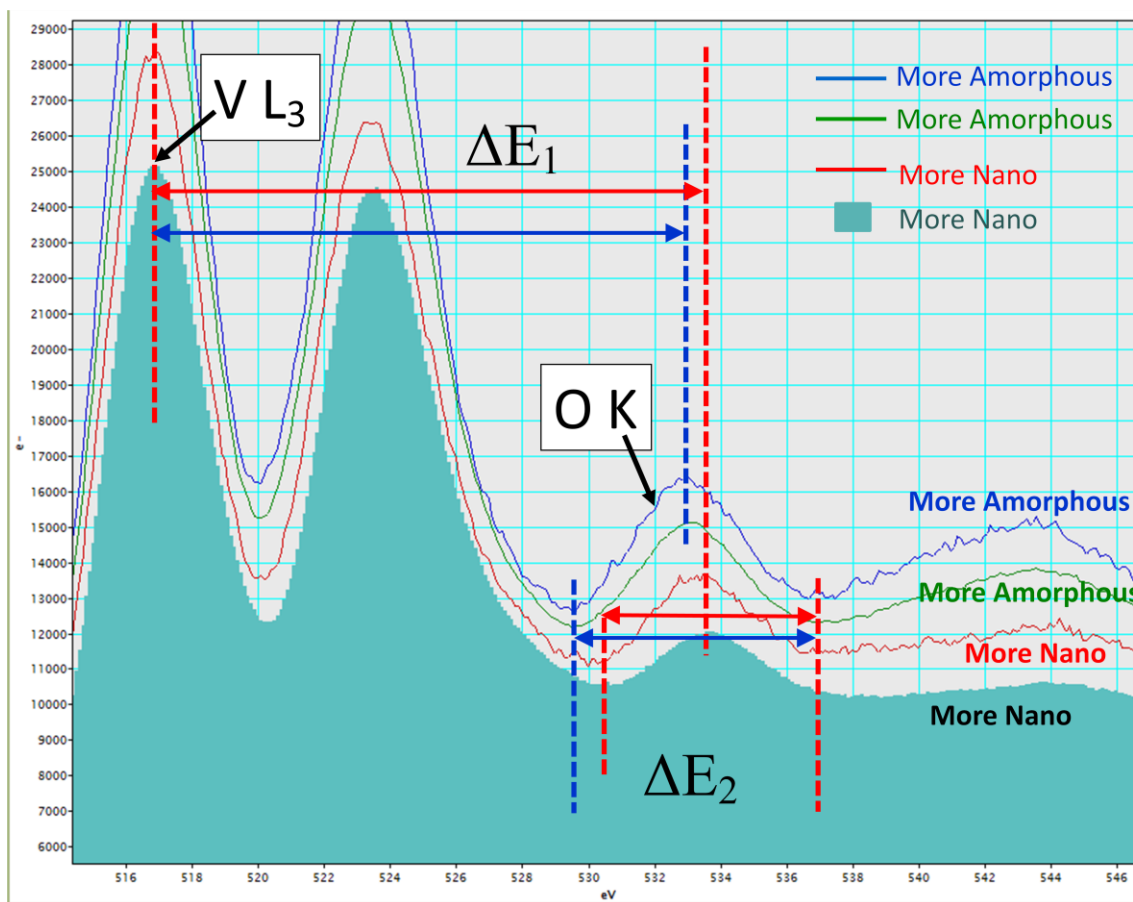


Figure 4-19: Comparison of EELS of amorphous and nano-crystalline regions. The relative positions of the O K edge indicates that the amorphous phase is richer in oxygen than the nano-crystalline phase.

Rutherford Backscattering Spectroscopy (RBS) was performed to obtain the stoichiometric details of these vanadium oxide films. Since the equipment is not available at Penn State, the measurements were outsourced to a facility at Rutgers University. RBS was performed using a 2.275 MeV beam of He^{2+} ions with the detector set at a backscattering angle of 160° . The results obtained for the sample deposited at 5% O_2 , before and after annealing at 300°C in nitrogen, are presented in Table 4-1. The fitted data shows that there is no significant change in the V:O ratio in the film as a result of annealing in nitrogen at 300°C . Both films had a O:V ratio close to 1.9.

Table 4-1: Comparison of RBS data of the 5% O_2 as-deposited sample and the 300°C annealed sample.

	Amount	Fit error
V	651.058	0.013472
O	1239.13	24.8521
Zr	5.59049	0.112157

Unannealed

O:V ratio : 1.90 ± 0.04

	Amount	Fit error
V	635.681	0.046427
O	1214.99	24.244
Zr	5.1567	0.102928

300°C annealed

O:V ratio : 1.91 ± 0.04

4.3 Low-Temperature I-V characteristics

Insight into the electronic structure and transport properties of VO_x films can be obtained by studying the low temperature conductivity behavior of these films. When we have two competing transport mechanisms, the effective resistance is given by

$$\rho_0^{-1} = \rho_1^{-1} \exp\left(-\frac{\varepsilon_1}{kT}\right) + \rho_2^{-1} \exp\left(-\frac{\varepsilon_2}{kT}\right) \quad (4.1)$$

where ε_1 and ε_2 are the respective activation energies. In general, ε_1 corresponds to some kind of band conduction and ε_2 corresponds to hopping conduction. Since, usually, $\rho_1 \ll \rho_2$ and $\varepsilon_1 > \varepsilon_2$ the first term dominates around room temperature while the second term takes over at lower temperatures [72]. In the Meyer-Neldel section, only the first term of this equation was considered since that is what dominates at around room temperature. Moreover, this equation assumes a homogeneous medium, which may not be entirely true in the case of VO_x.

Mott showed that, for amorphous materials, below a certain critical temperature (T_c), the second term corresponding to hopping could be approximated by a power law dependence with temperature given by Eq. 4-2 [73]. This is commonly referred to as variable range hopping (VRH) mechanism. For this case,

$$\rho = \rho_0 \exp\left(\frac{T_0}{T}\right)^p \quad (4.2)$$

where ρ_0 is the pre-exponent factor and T_0 is a measure of the degree of disorder in the film. The value of p depends on the mode of hopping at low temperatures. According to Mott (M-VRH), $p = 1/4$ or $1/3$ for a 3D and a 2D system respectively, considering a constant density of localized states in the mobility gap. But according to Efros and Shklovskii (ES-VRH), in crystalline semiconductors, due to coulombic interactions, the density of localized states diminishes in the immediate vicinity of the Fermi level, thereby resulting in a coulombic gap. This results in a conduction behavior with a value of $p = 1/2$.

For vanadium oxide samples deposited at three different conditions - 18sccm flow with 5, 7.5 and 10% oxygen - the resistivity versus $1/T$ behavior is shown in Fig. 4-20. The critical temperature at which deviation from Arrhenius behavior occurred was found to be 148, 170 and 208 K respectively.

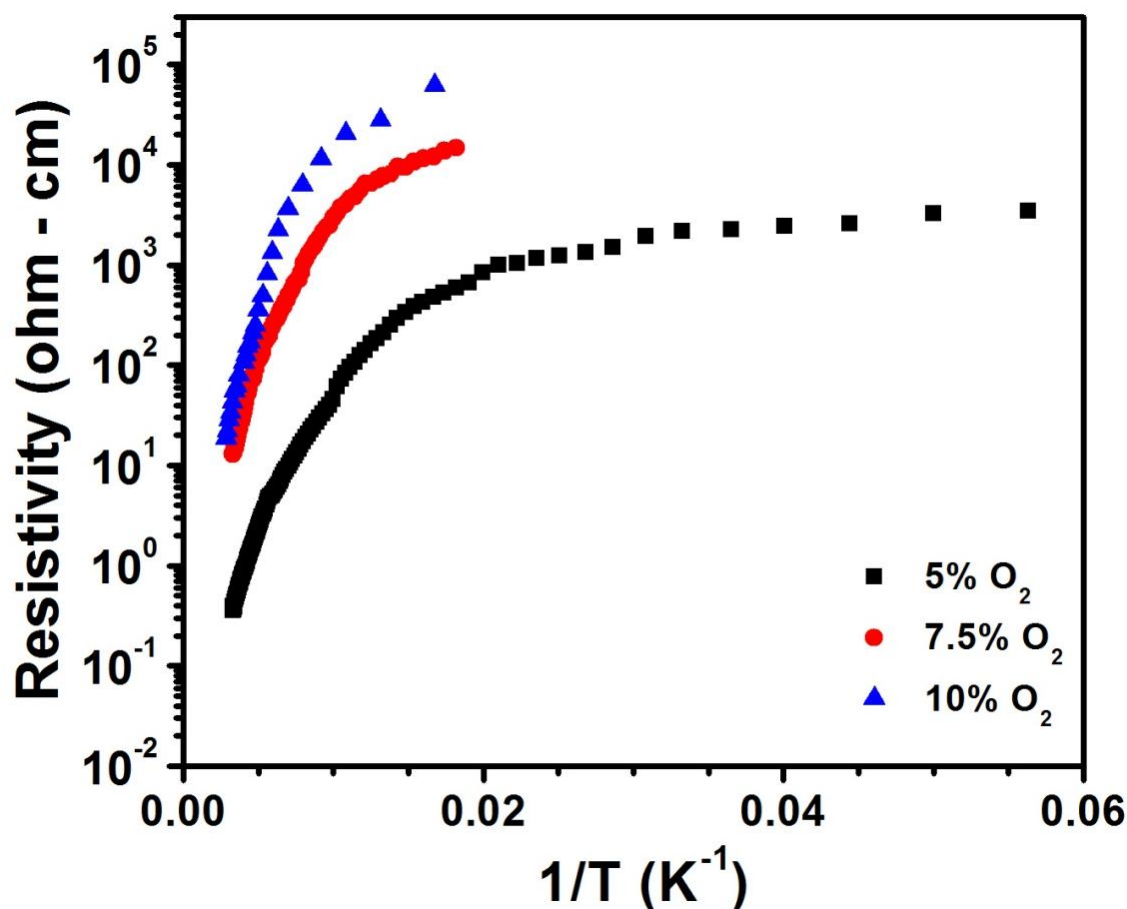


Figure 4-20: Variation of resistivity as a function of temperature for three samples deposited at 5, 7.5 and 10% oxygen at a flow rate of 18 sccm.

The value of the exponent “p” applicable to the conduction behavior observed is obtained by following a method proposed by Hill⁷⁴ and Zabrodskii [75]. Here the localized activation energy dE is calculated at various temperatures using the expression given in Eq. 4.3. When this

localized activation energy is plotted as a function of temperature on a log-log scale, the slope gives the value of “p”.

$$dE = \frac{d\left[\frac{1}{\rho(T)}\right]}{d[\ln(T)]} \quad (4.3)$$

The average value of p for the as-deposited vanadium oxide samples was found to be $\sim 1/2$.

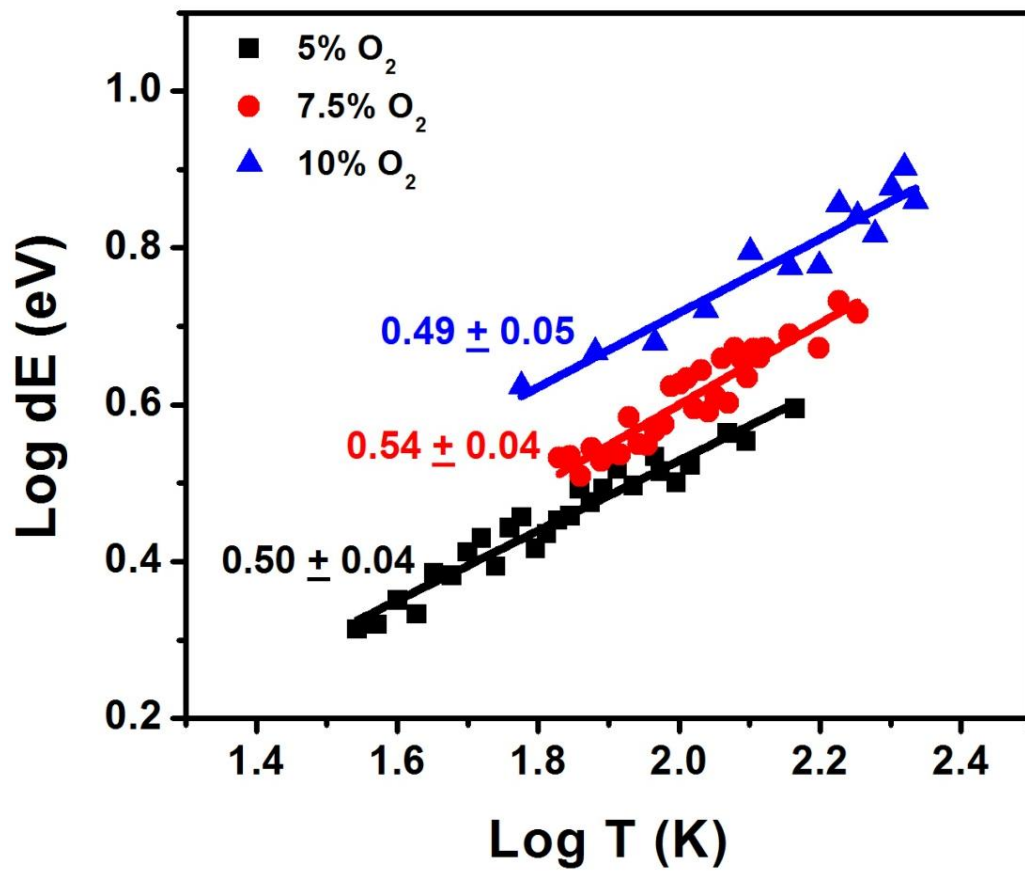


Figure 4-21: Plot of log dE versus log T between T_c and 30 K.

A similar analysis was performed on the annealed samples, the results of which are plotted in Fig. 4-22 and 4-23 below. As the anneal temperature increased, the room temperature resistivity dropped while the slope of the log (resistivity) versus T plot increased, corresponding

to an increase in the activation energy. The increase in slope was found not just at room temperature, but also down to 100 K.

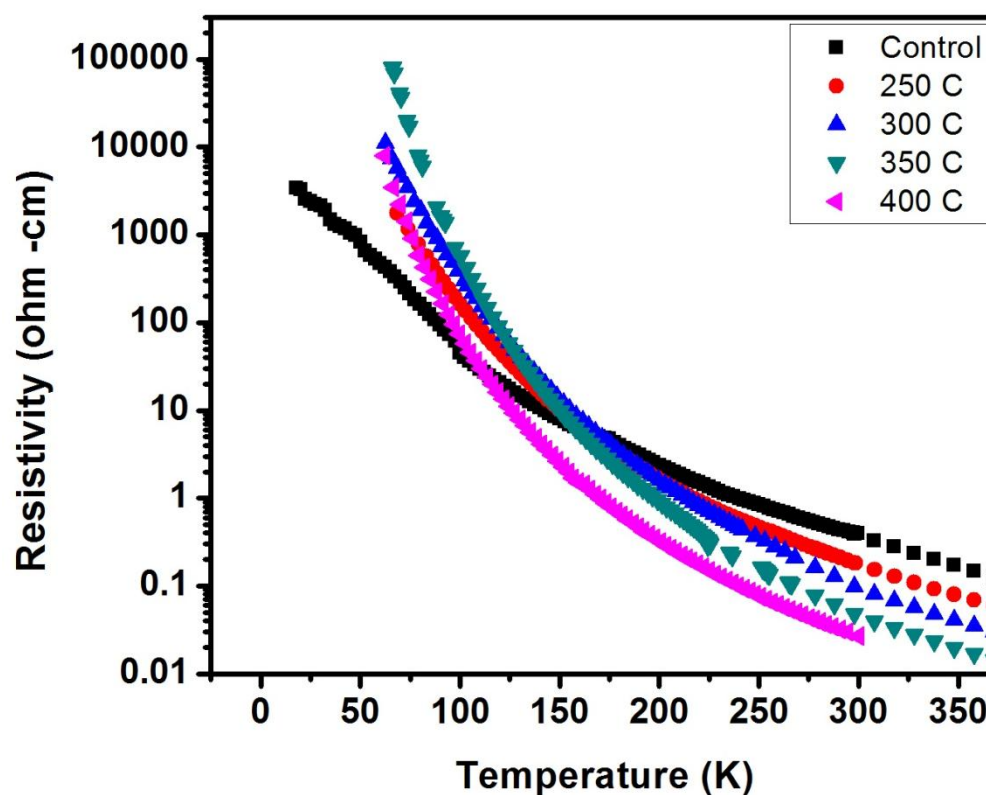


Figure 4-22: Resistivity versus temperature behavior of annealed samples.

An even more interesting trend was observed when resistivity was plotted as a function of $(1/T)^{0.5}$. As the annealing temperature increased, the temperature regime over which ES-VRH was observed extended up to room temperature as shown in Fig. 4-23.

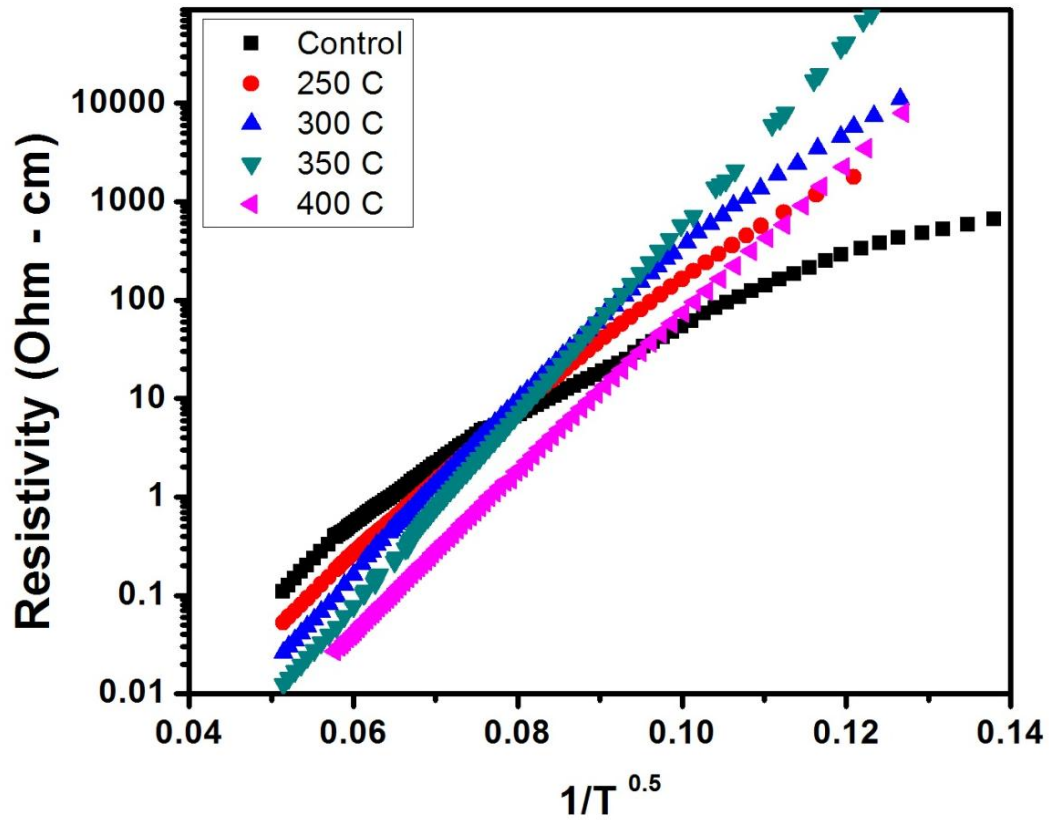


Figure 4-23: Resistivity of annealed samples as a function of $(1/T)^{1/2}$.

4.4 Theoretical model

All results indicate that even though annealing does not change the structure of the film on a macroscopic scale, it does significantly alter the electrical properties. Most likely, this could be caused by some kind of re-arrangement/ordering taking place between the different phases present, leading to alteration of the values of ρ_1 , ρ_2 , ϵ_1 and ϵ_2 , which in effect determine the microscopic conduction behavior.

A proposed structural model is shown in Fig. 4-24. The nano-crystalline fcc rock salt VO phase is dispersed in the bulk amorphous matrix. Some of these nanocrystals are present as twinned structures. There is also significant porosity present in the film. The hypothesis is that

by annealing, we are reducing the porosity and introducing more order into the film, thereby establishing a more connected network between the other phases. The voids in the film cause disorder, resulting in a high number of electronic states in the nearby material. At low temperatures, these defects states aid in conduction by providing additional states for the carriers to hop and hence the as-deposited samples have lower resistivity than the annealed samples. But at higher temperatures, when the hopping distances increase and reach the order of the void size, these voids act as hindrances to the motion of carriers. By annealing, we are in effect reducing the number of voids present in the material and hence the room temperature resistivity of the annealed samples is lower than that of the as-deposited samples. Another possible reason could be the relaxation of the stress present in the material, leading to alteration of the electronic band structure.

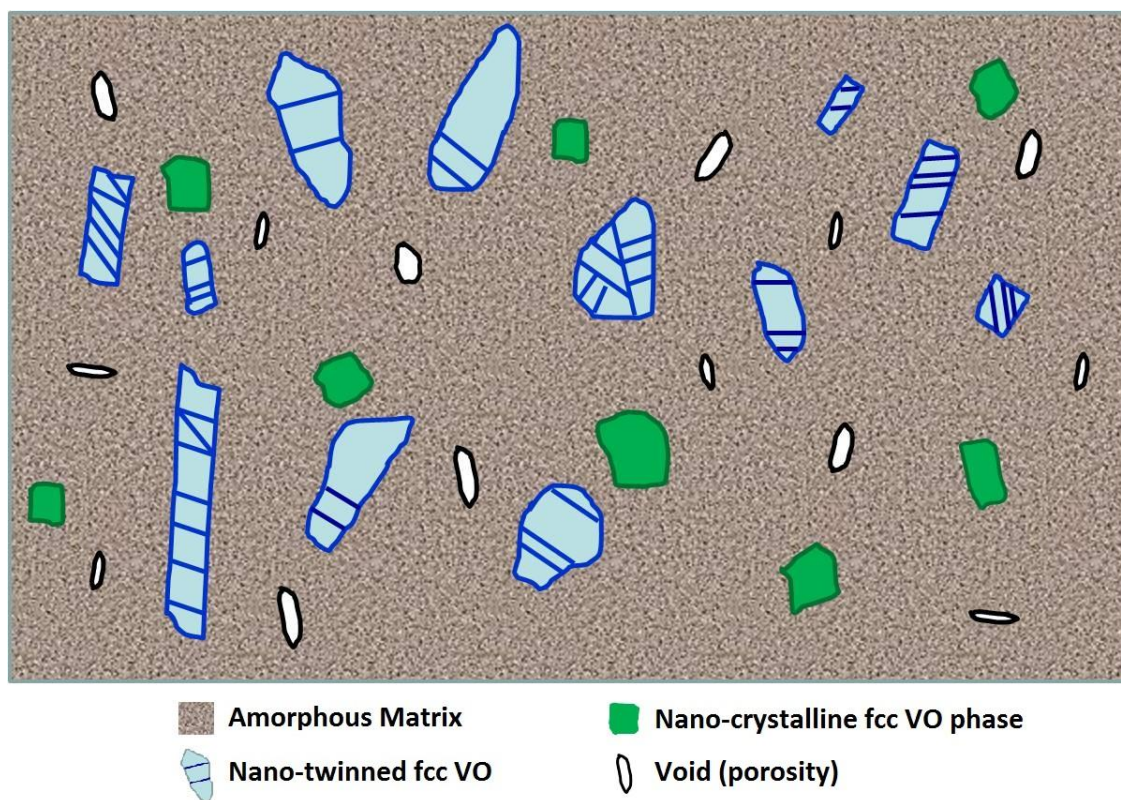


Figure 4-24: Proposed structure model for vanadium oxide thin films.

4.5 Summary

A comparison of TCR and resistivity of the annealed films with the values obtained for as-sputtered films is provided in Fig. 4-25. In almost every case, annealing of the films, regardless of the ambient atmosphere, had a beneficial effect on the TCR in comparison to the un-annealed films. Some of the oxygen-annealed films did have a good TCR/resistivity combination, but their resistivities are outside the current range of interest (~ 0.05 to $5 \Omega\text{-cm}$) for use in microbolometer applications. The graph clearly reveals that higher TCRs with relatively lower resistivities are achieved mainly for the nitrogen-annealed films. In particular, the films annealed at 300°C in nitrogen ambient yielded the optimum combination of properties.

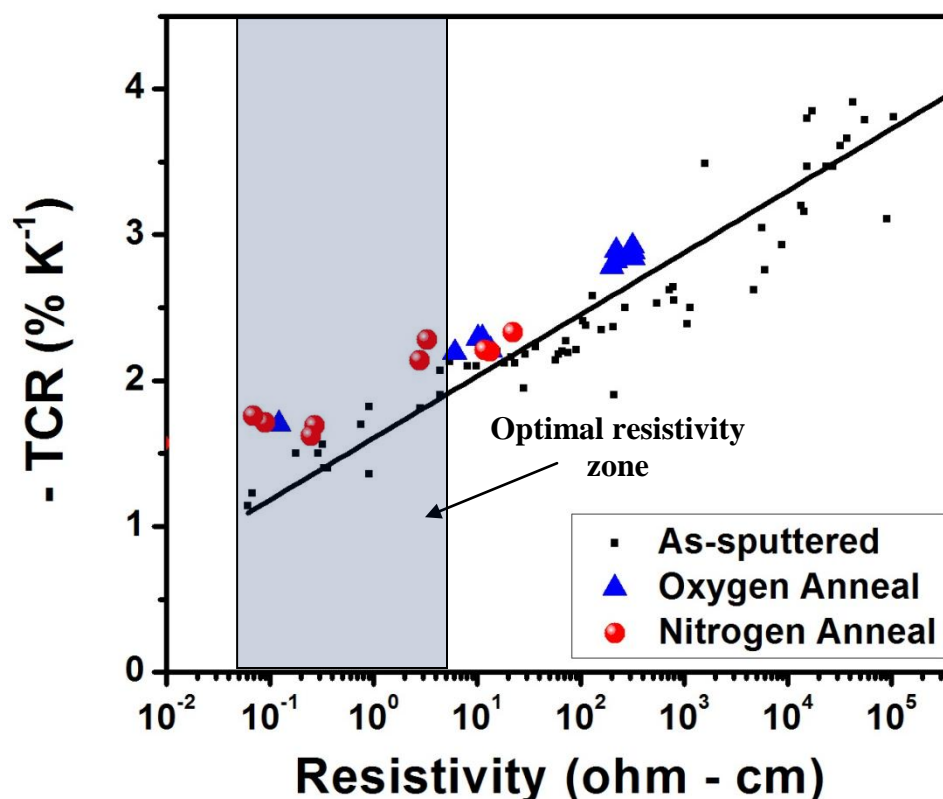


Figure 4-25: Comparison of TCR and resistivity values for annealed and as-sputtered films. Clearly the annealed films have a better TCR at any given resistivity.

This anneal condition was evaluated on many samples with different starting resistivities and different thicknesses in order to establish the effectiveness and versatility of this technique. The results are plotted in Fig. 4-26. It clearly shows that the films annealed at 300 °C in a nitrogen atmosphere for 30 minutes have a superior TCR for any given resistivity.

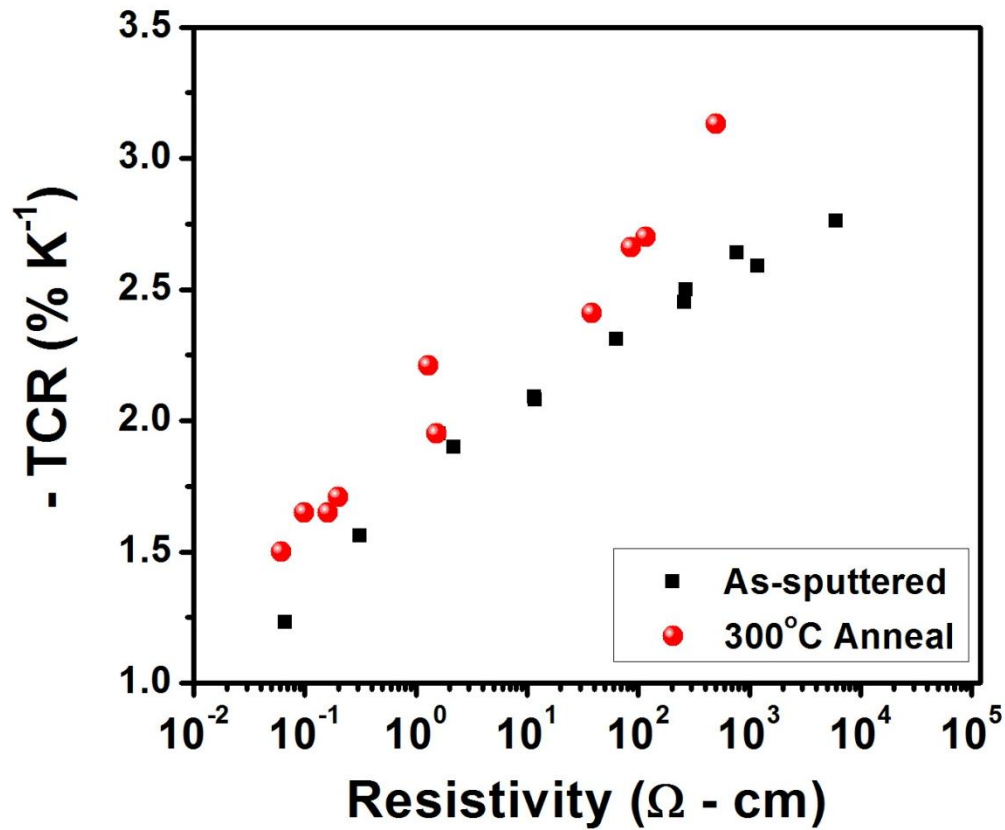


Figure 4-26: Comparison of TCR and resistivity of VO_x films before and after annealing in nitrogen for 30 min.

The TCRs of the annealed samples were then recalculated using the activation energy method, and plotted on the universal plot, in comparison to the other data obtained from literature (Fig. 4-27). It was found that the TCRs obtained after annealing were higher than those published by Radford [10], but somewhat lower than that of Wood [6]. None the less, the large change in

conduction caused by annealing may prohibit these films from being practical in an industrial application because of their instability. More studies on the thermal stability of these films in a film stack representative of that used in commercial microbolometers is necessary in order to determine their viability as an imaging layer in a production focal plane array.

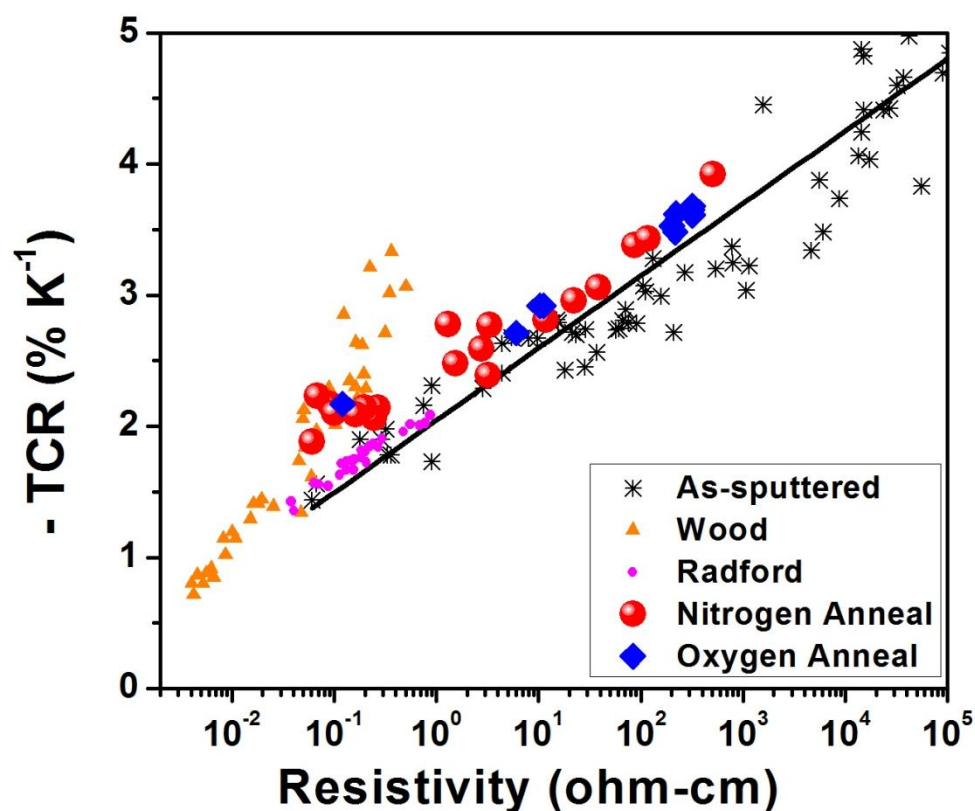


Figure 4-27: Comparison of TCR and resistivity of annealed samples to published results.

Chapter 5

Post-deposition processing: Ion Implantation

Ion implantation is a well known non-equilibrium method to introduce new species into a material in order to modify its chemical, electrical, mechanical or optical property. By judicious choice of the implant species, energy and dosage, the required properties can be achieved. Moreover, the mere passage of high energy ions through a solid can result in modification of the properties. This is generally referred to as ‘radiation damage’, where the effect is not desirable, and can sometimes be removed or reduced by suitable choice of the temperature of the solid during or after implantation. But in many cases, the disorder created by the passage of fast ions has been found to be beneficial [76]. For example, it can cause amorphization of the film and/or introduce point/extended defects in the material. In our particular case, this might lead to changes in the electrical band structure, which in turn might affect the transport properties of the charge carriers.

Two atomic species – hydrogen and helium – were chosen for implantation. Hydrogen is an active species well known for passivating defect states in a wide variety of electronic materials and was hence tried out VO_x . Helium (an inert species) was chosen mainly to distinguish between the effects arising from bombardment on the film and the passivating influence of hydrogen. In this preliminary study, two different dose levels were used for both the elements.

The implantation parameters were arrived at based on TRIM simulations as explained in Chapter 2. The energy chosen was 10 keV. Totally, four different implantation runs were performed: $\text{H}^+ 10^{13}$ atoms/cm², $\text{H}^+ 10^{15}$ atoms/cm², $\text{He}^+ 10^{14}$ atoms/cm², $\text{He}^+ 10^{15}$ atoms/cm². These implantations were performed on four different films with as-deposited resistivities ranging from 0.05 Ω -cm to 100 Ω -cm and their corresponding TCRs varying from -1.1% to -2.7%.

5.1 Results and Discussion

Ion implantation caused significant variations in the TCR and resistivity of the samples as shown in Fig. 5-2. In all the films, after both H^+ and He^+ implantation, the resistivity of the films was seen to increase by half an order of magnitude and the TCR by 5-25% depending on the initial composition. This effect was seen for both dosage levels. The reason for this is believed to be the damage induced in the material because of implantation. The simulation result for target displacements expected from implantation of H^+ (10 keV) in VO_x is shown in Fig. 5-1.

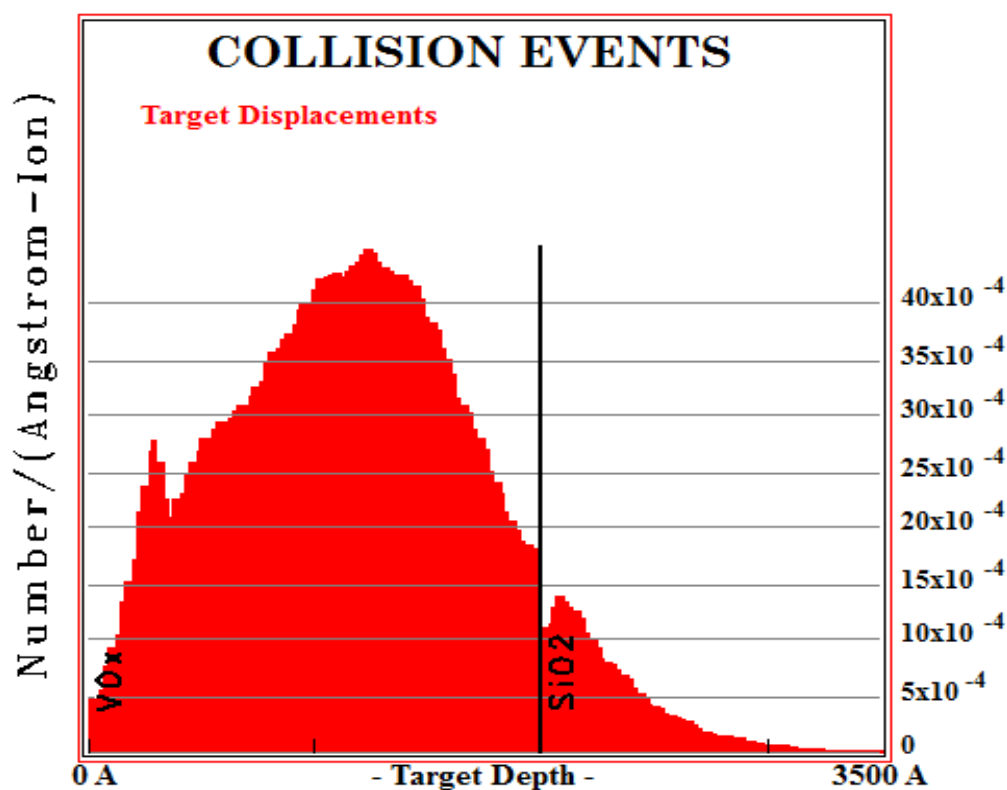
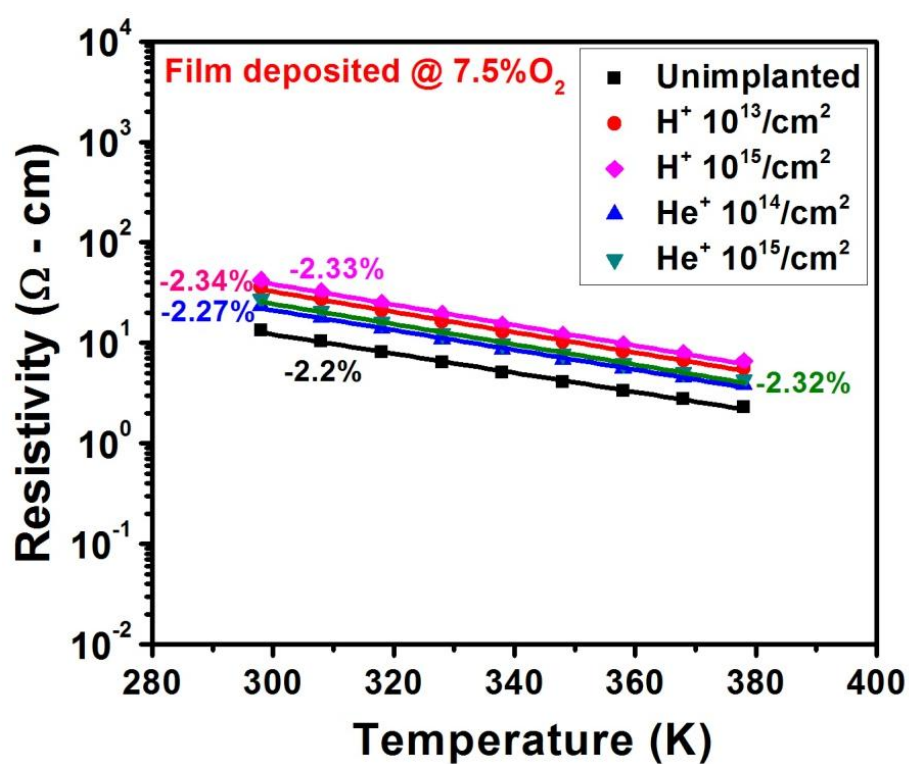
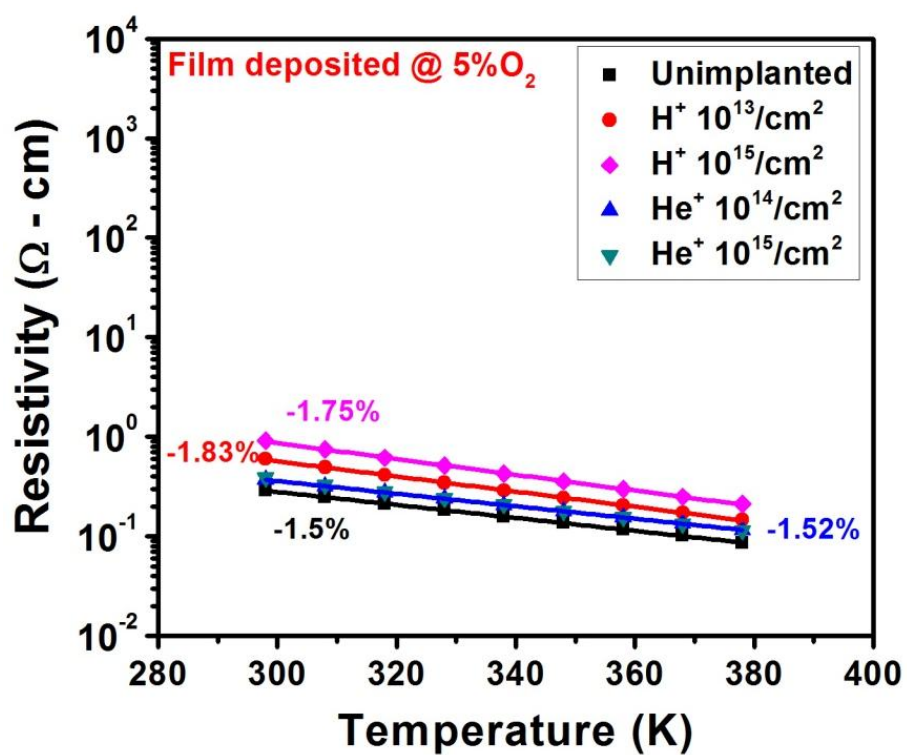


Figure 5-1: Target displacements due to implantation of H^+ in VO_x .



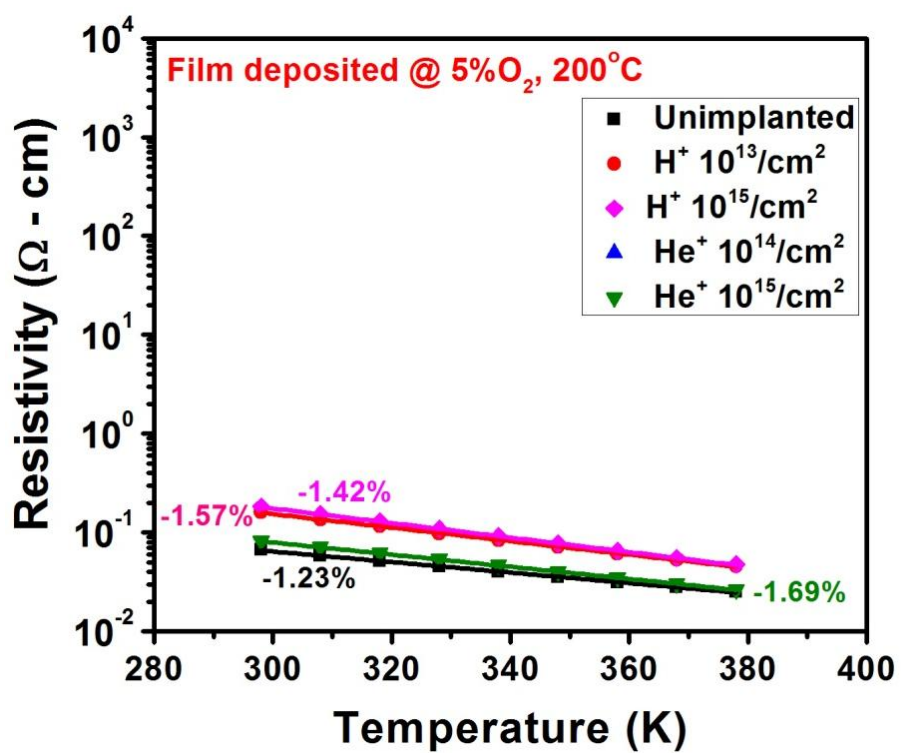
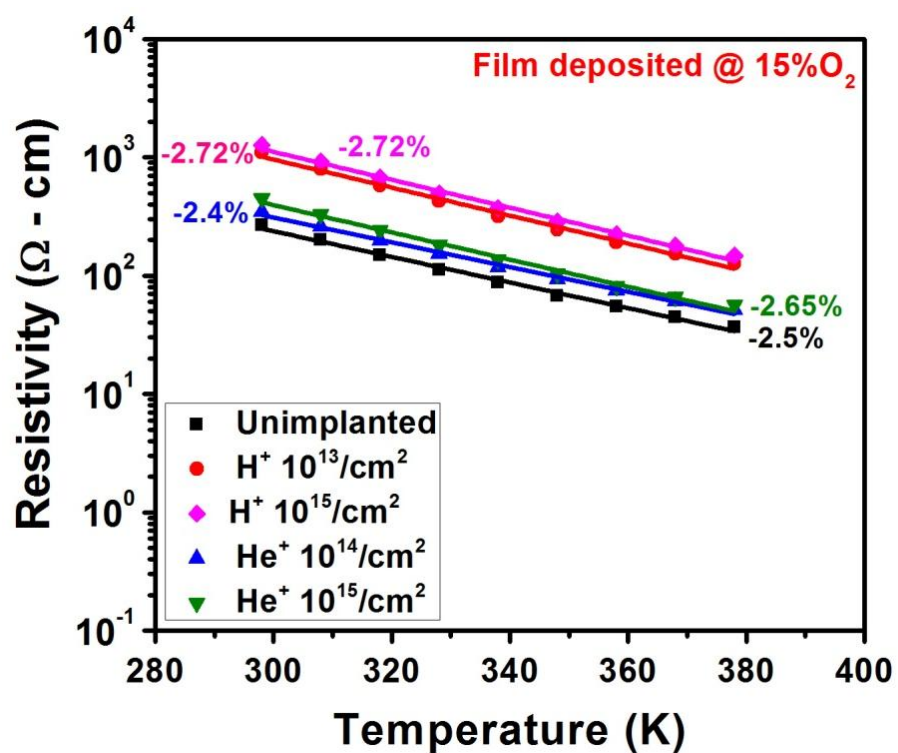
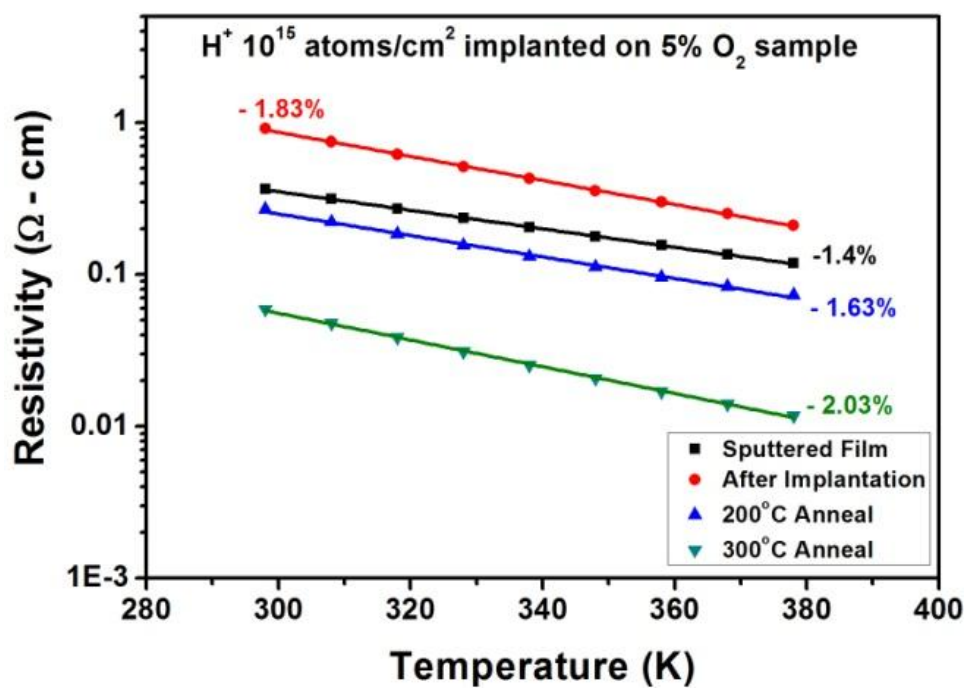
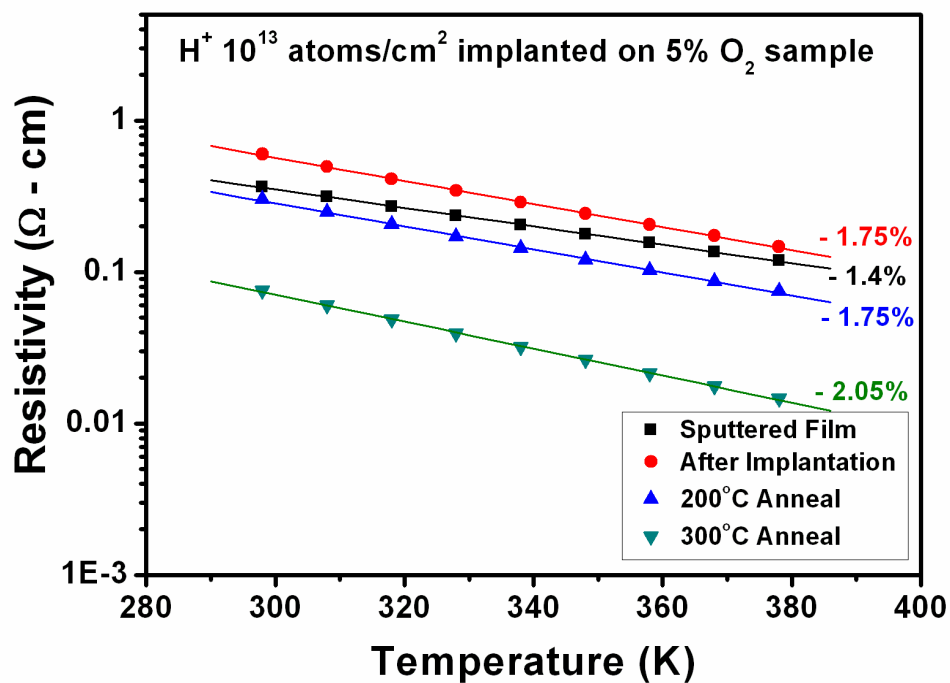


Figure 5-2: Effect of implantation on the TCR and resistivity of VO_x films deposited under different conditions. Both the TCR and resistivity of the films go up after implantation.

In Chapter 4, it was found that annealing in nitrogen resulted in optimal properties for the microbolometer application. So the implanted films were subsequently annealed in nitrogen, to try reduce the resistivity, but at the same time, retaining the improved TCR. Annealing was done for 30 min at each of three temperatures: 200 °C, 300 °C and 400 °C.

The effect of annealing on the electrical properties of the sample deposited at 5% O₂ (starting resistivity ~ 0.3 Ω - cm) and implanted with hydrogen/helium is shown in Fig. 5-3. As with the unimplanted samples, the 200 °C anneal lowered the resistivity slightly without much change to the TCR. But when annealed at 300 °C, the resistivity dropped by more than an order of magnitude and the TCR increased by ~ 30% as compared to the original film. And this was seen for both H⁺ and He⁺ implant at both dose levels. This resultant TCR/resistivity combination was better than that of samples annealed directly after deposition, without the implant. The 400 °C anneal caused the resistivity to drop by more than two orders of magnitude and also made the log (resistivity) versus temperature plot non-linear, making it unsuitable for use in bolometers.



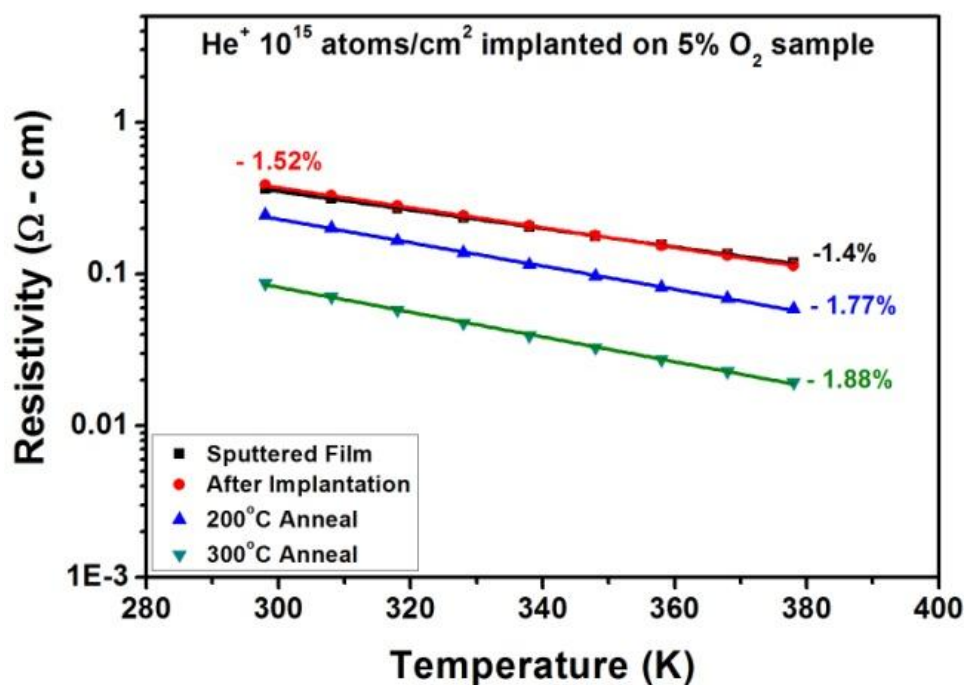
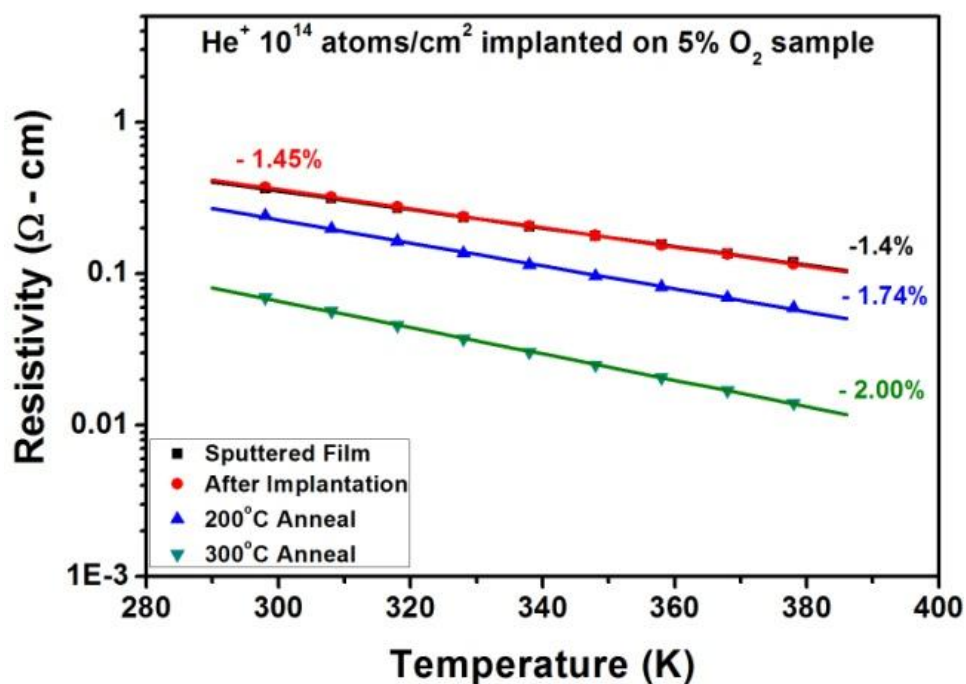


Figure 5-3: Resistivity and TCR values as a function of annealing temperature for a film deposited at 5 mTorr pressure and 5% O₂ and implanted with (a) H⁺ 10¹³ atoms/cm² (b) H⁺ 10¹⁵ atoms/cm² (c) He⁺ 10¹⁴ atoms/cm² and (d) He⁺ 10¹⁵ atoms/cm².

The x-ray diffraction spectra of one of the samples before/after implantation with He^+ and after annealing are shown in Fig. 5-4. All the spectra look very similar, and we can clearly see that the rocksalt FCC VO phase is retained even after implantation and annealing. This shows that ion implantation causes only small damage to the structure of the films, but that is good enough to alter the electrical properties. And this is also reflected in the cross-sectional SEM images shown in Fig. 5-5. The columnar structure is still retained even after the 300 °C anneal.

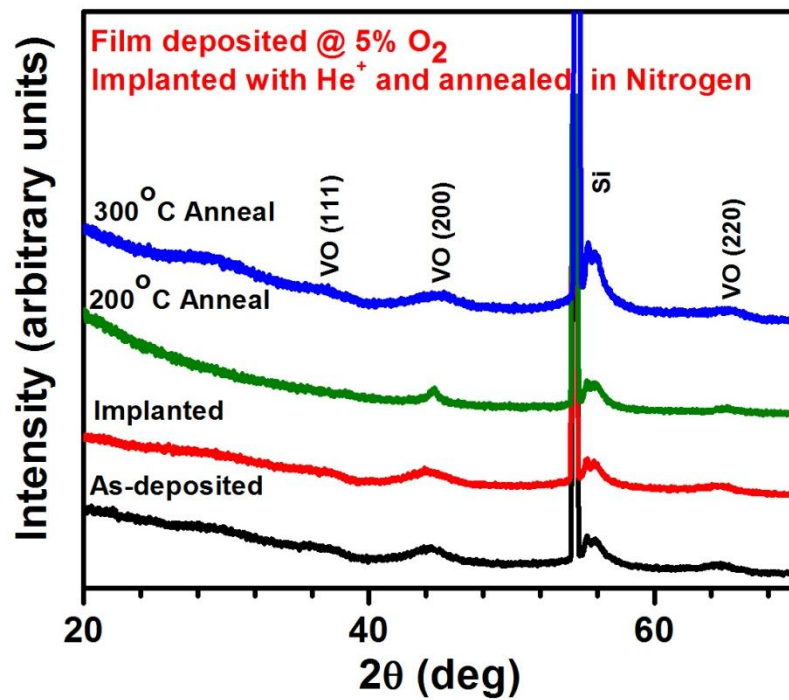


Figure 5-4: Comparison of X-ray diffraction spectra of samples as deposited, after implantation and after annealing in nitrogen.

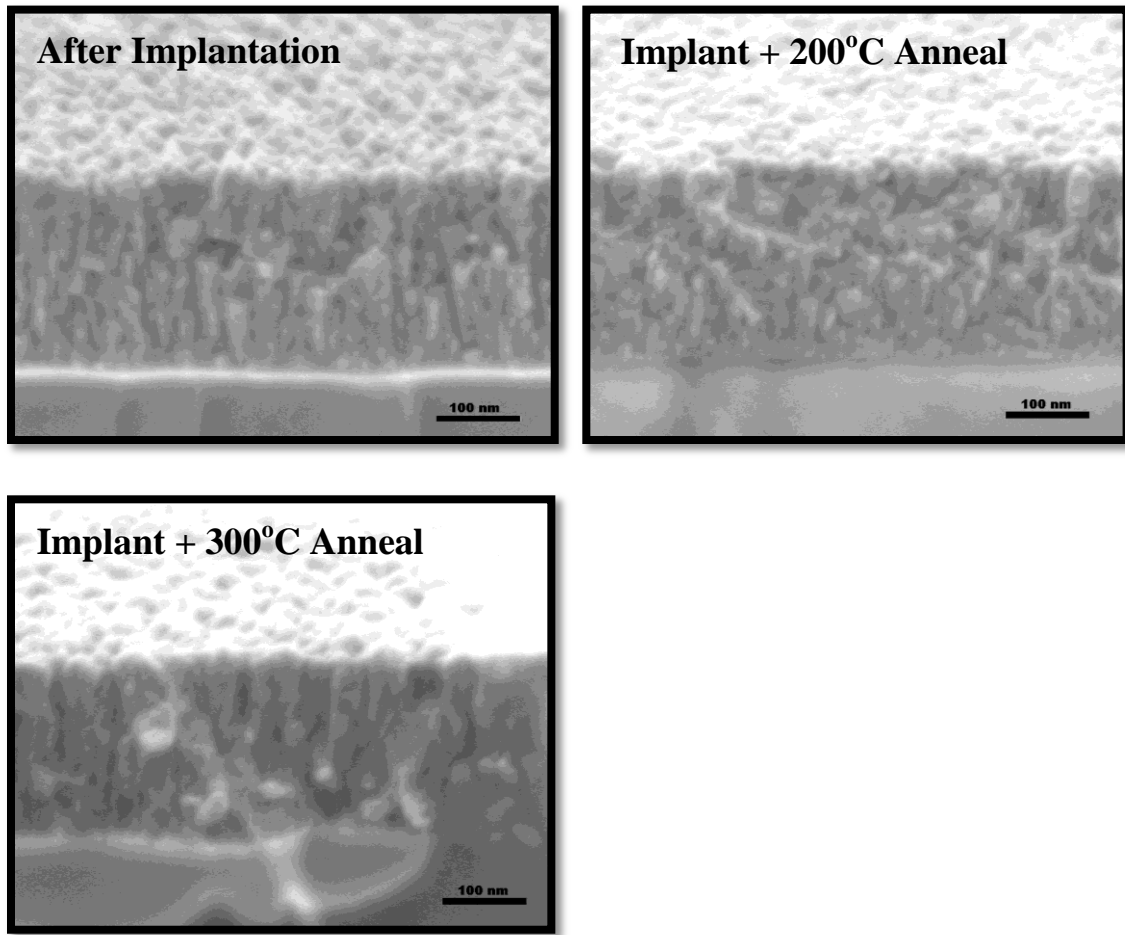


Figure 5-5: Cross-sectional SEM images of the (a) after implantation, (b) after implant + anneal at 200 °C, and (c) after implant + anneal at 300 °C.

A similar behavior was observed for another sample with a slightly lower starting resistivity ($0.1 \Omega \cdot \text{cm}$) and implanted/annealed under the same conditions (see Fig. 5-6). Even though the extent of change in resistivity and TCR are not the same, the overall results were similar – a beneficial TCR/resistivity combination. There were not any significant differences in the properties for different dose levels, and hence plots corresponding to only one dose level are shown for all the subsequent samples.

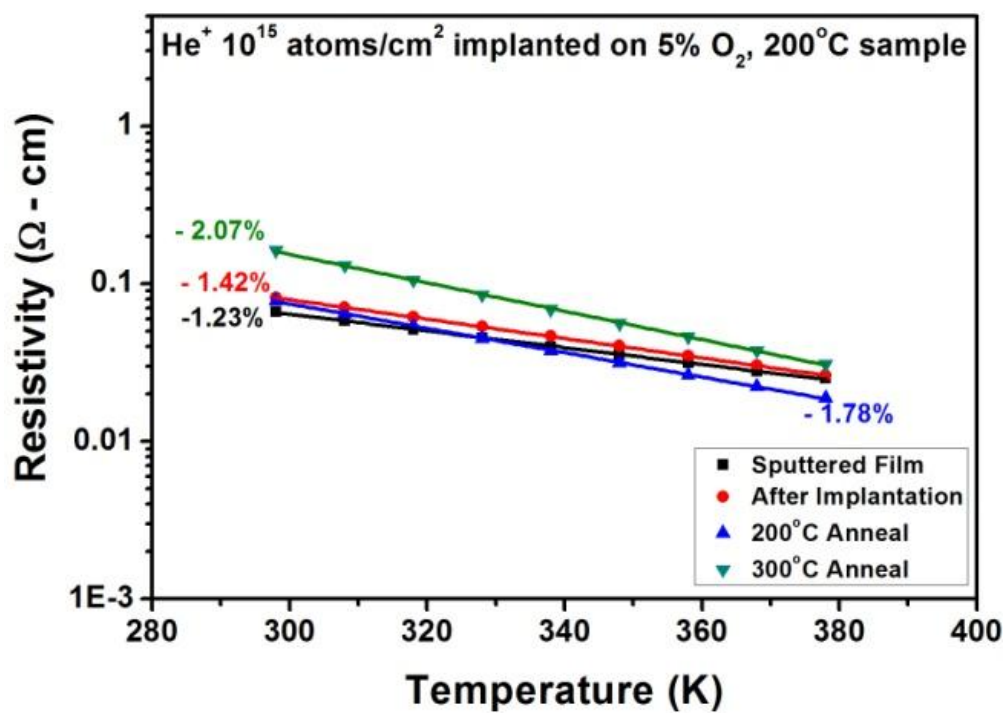
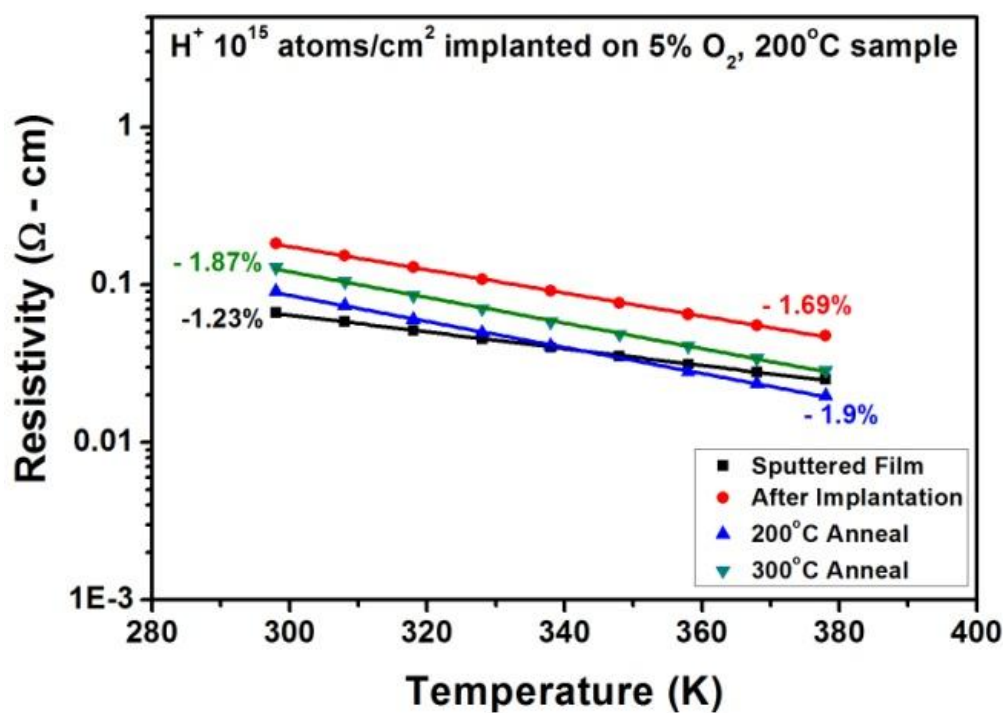


Figure 5-6: Variation of resistivity and TCR of a sample deposited with 5% O₂ at 200 °C after implantation with H⁺/He⁺ and annealing at various temperatures.

In higher resistivity as-deposited samples that received implantation, the 300 °C anneal revealed significant differences between the hydrogen and helium implants (Fig. 5-7 and 5-8). In the H^+ implanted samples, the resistivity decreased by half an order of magnitude and the TCR remained almost unchanged. But in the He^+ implanted samples, the resistivity dropped by several orders of magnitude, and the films became metallic-like with very low TCR values. The exact reason for this is not known, but we speculate it to be related to the extent of damage and subsequent changes in the electronic structure. X-ray diffraction spectra did not reveal any differences between the two films (Fig. 5-9).

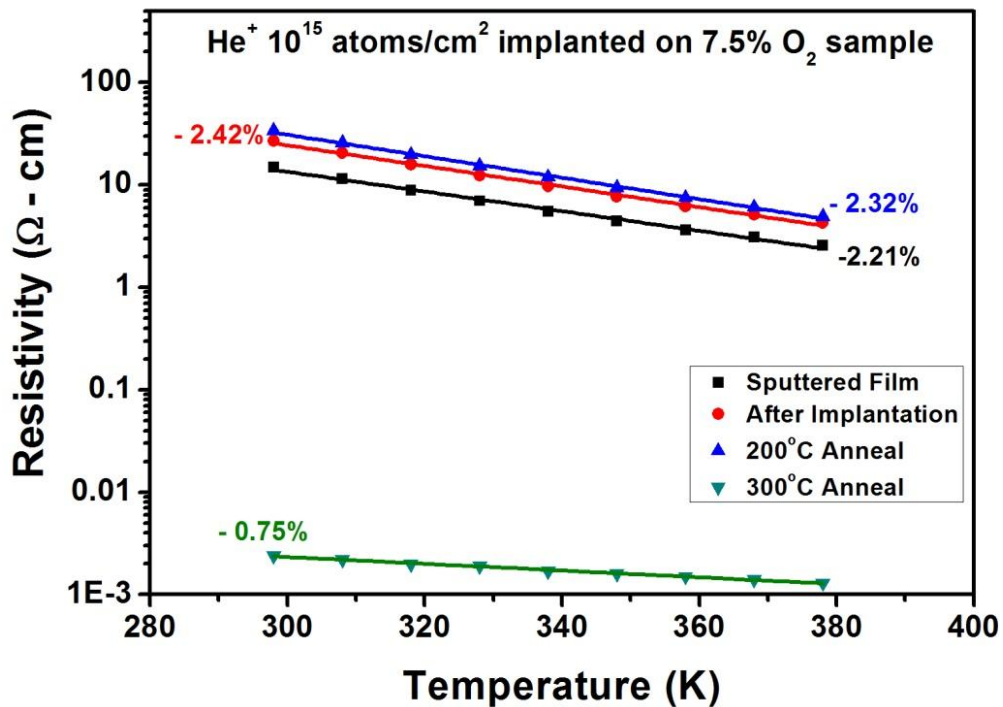
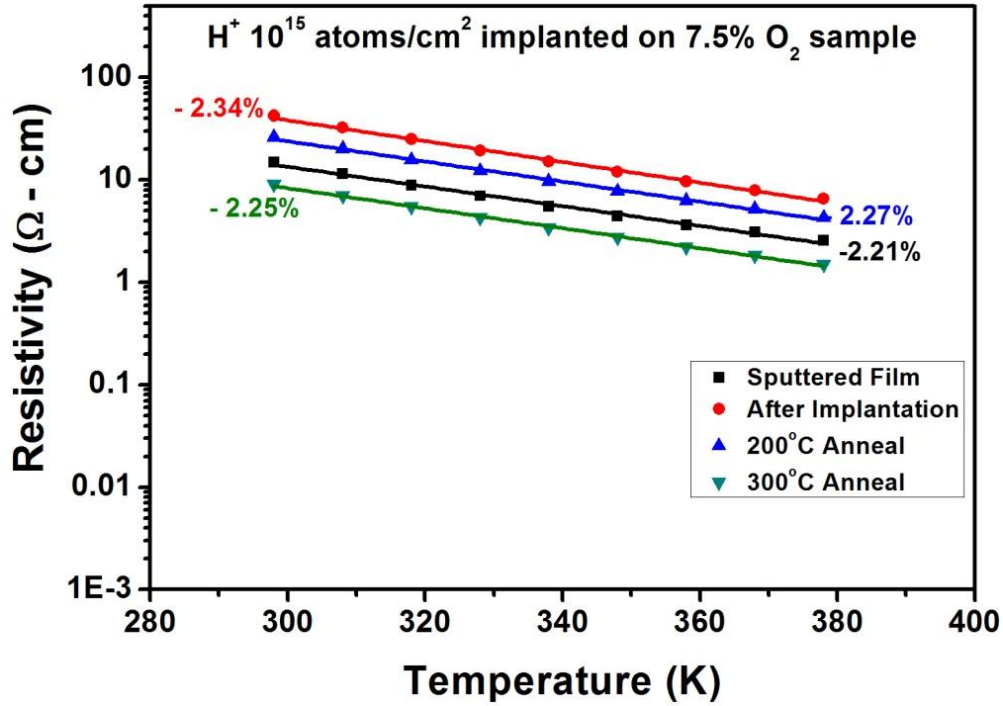


Figure 5-7: Variation of resistivity and TCR of a sample deposited at 7.5% O₂ after implantation with H⁺/He⁺ and annealing at various temperatures. We can clearly see the difference in behavior between the H⁺ and He⁺ implanted samples after the 300 °C anneal.

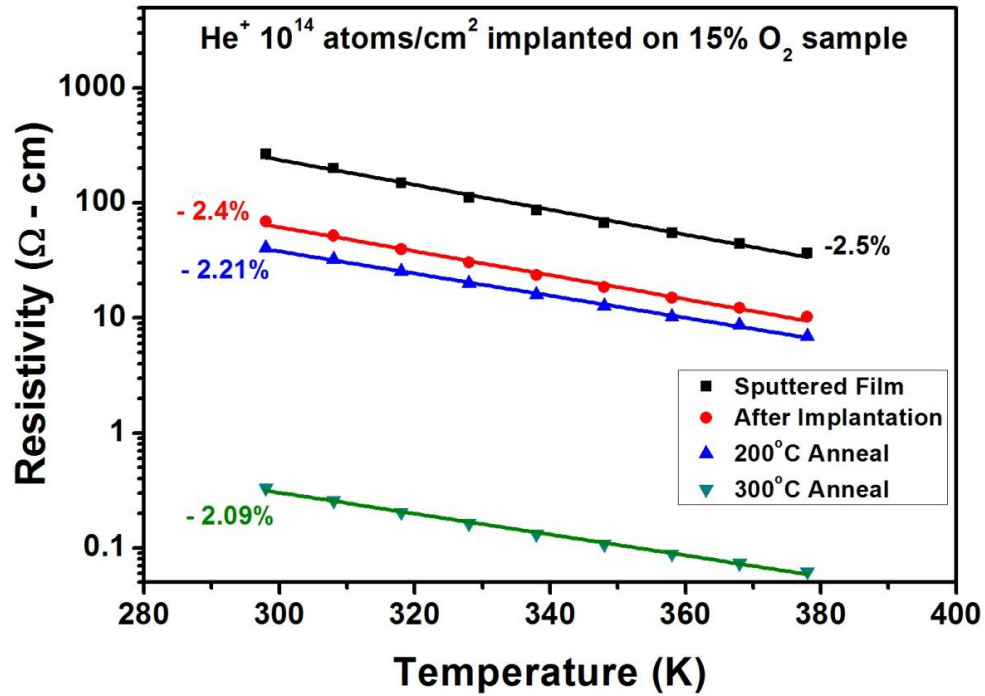
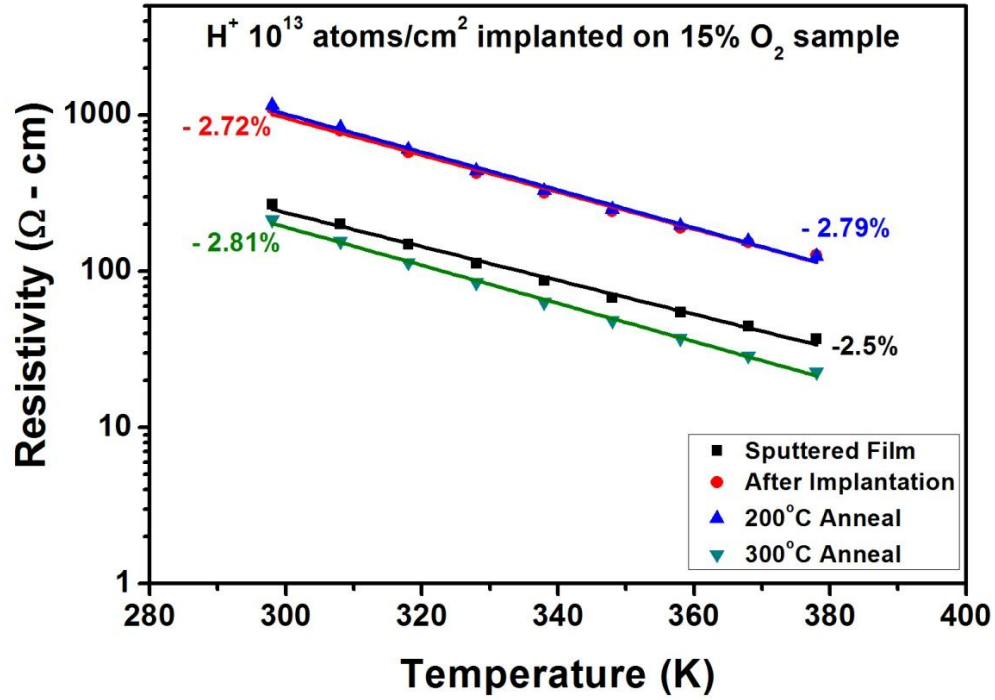


Figure 5-8: Variation of resistivity and TCR of a sample deposited at 15% O₂ after implantation with H⁺/He⁺ and annealing at various temperatures. Here again the difference in behavior between the H⁺ and He⁺ implanted samples after 300 °C anneal is observed.

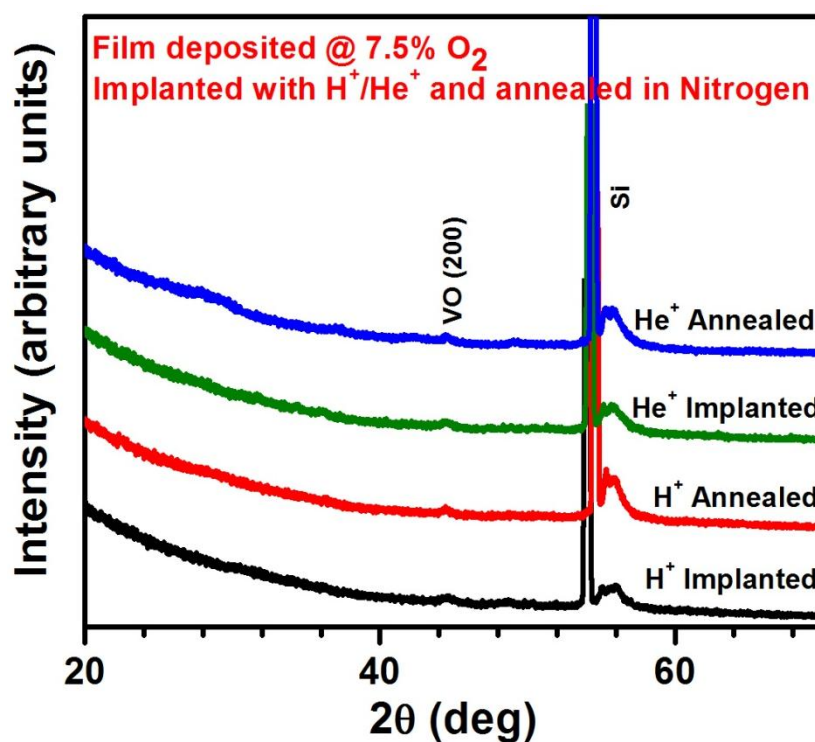


Figure 5-9: XRD spectra of sample deposited at 7.5% after implantation with H⁺/He⁺ and after subsequent annealing. No significant difference between the H⁺ and He⁺ implanted samples.

The summary of the changes in the electrical properties obtained as a result of ion implantation followed by annealing is shown in Fig. 5-10. It can clearly be seen that the improvement in TCR, for a given resistivity, is much more in this case as compared to just the annealed. And when the TCRs were recalculated as instantaneous values at room temperature using the activation energy method and compared to the industrial samples, they were on par, if not better than the best ones (see Fig. 5-11).

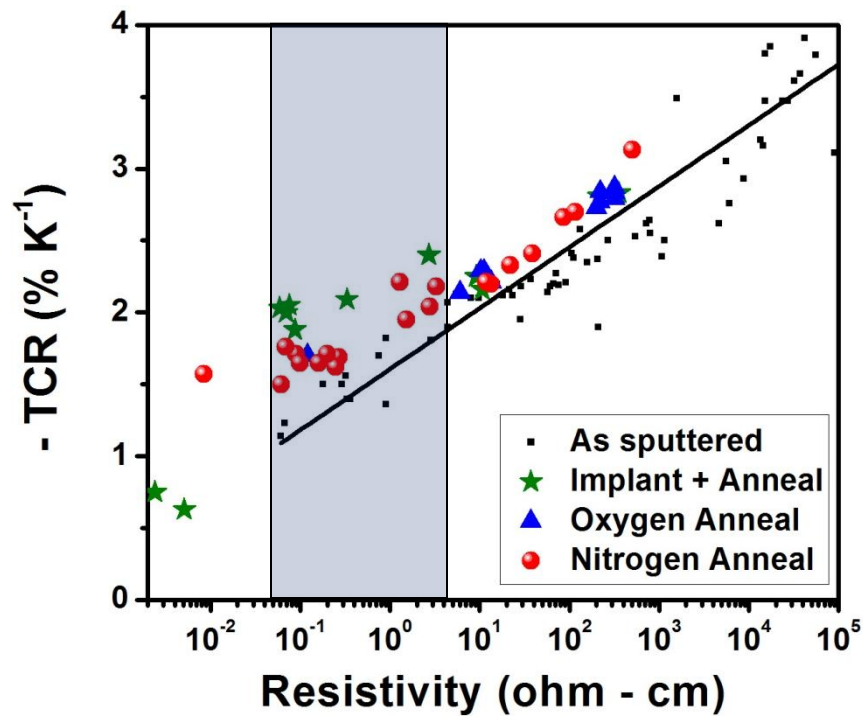


Figure 5-10: TCR values as a function of resistivity for the as-sputtered films, annealed films and the implanted/annealed films.

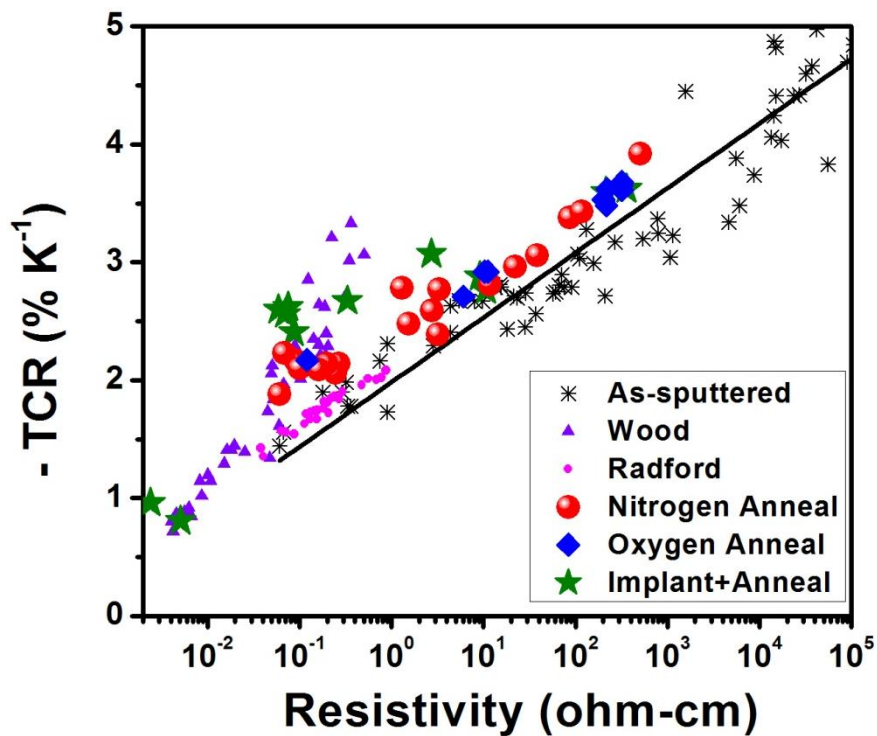


Figure 5-11: Comparison of TCR and resistivity of implanted and annealed samples with the industrial ion beam samples.

Chapter 6

Conclusion

Pulsed DC sputtering has been shown to be a viable method for depositing vanadium oxide thin films. Though the reactive sputtering process is inherently hysteretic, by proper choice of parameters, films with desired properties can be obtained. Films were deposited over a wide range of resistivity ranging from 0.05 to 10^5 Ω -cm and their TCR values were comparable to those of films deposited by ion beam deposition. It was found that the room temperature resistivity of the films increased with increase in the total flow rate as well as the oxygen partial pressure. Films deposited at low flow rates (~ 18 sccm) and low oxygen percentages ($\sim 5\%$) have resistivities in the range currently used by the microbolometer industry.

The process hysteresis characteristics were investigated by measuring the cathode (target) current under different total gas flow rates and oxygen-to-argon ratios. Approximately, 20-25 % change in the target current was observed as the target changed from an elemental metallic state to a stable oxidized state, and this change exhibited an hysteresis behavior between the forward (metallic to oxidized) and reverse (oxidized to metallic) directions. This hysteresis behavior was also reflected in the electrical and structural properties of the resultant films. And there was a direct correlation between the resistivity of the films and the associated cathode currents during deposition. Hence cathode current could be used as a metric for controlling the film properties.

GIXRD results indicated that most of the deposited films were x-ray amorphous. However, films deposited at low flow rates and low oxygen partial pressures did contain some crystalline peaks corresponding to the VO phase with FCC rock salt structure. But overall, GIXRD was not found to be an useful technique to detect small changes in the structure of these vanadium oxide films.

TEM images showed that the nano-crystallites were embedded in the bulk amorphous matrix, with some of them existing as twinned structures. There was also a lot of apparent porosity present in the films but it was not quantified. Films grown at low to moderate flow rates were found to be columnar as seen under FESEM, but at higher flow rates, the grains became equi-axed.

Raman spectroscopy showed that as the total amount of oxygen in the system increased, the ratio of the intensity of the high frequency mode (V-O stretching) to the low frequency mode (V-O bending) increased. This increase in relative ratio is most likely due to an increase in the Raman scattering cross-section of the films associated with increasing oxidation levels in the film. By far, this has been the most sensitive technique to detect subtle changes in the stoichiometry/chemical composition of VO_x films.

The resistivity and TCR of the films increased with increase in total flow rate as well as oxygen percentage. The higher the resistivity, the higher was the TCR. The TCR values were comparable to some of the data published on ion beam deposited samples.

Post deposition annealing was done in oxygen and nitrogen atmospheres at various temperatures in an attempt to improve the trade-off between TCR and resistivity. Beneficial results were obtained for both oxygen and nitrogen annealing. But most of the films that were annealed in oxygen were driven towards higher oxides of vanadium (mainly V_2O_5) which have a high resistivity at room temperature. Thus, even though they had a good TCR, their resistivity was too high to be useful for the current microbolometers and associated read-out circuitry. The most optimal results were obtained for films annealed at 300 °C in nitrogen. In certain cases, the resistivity dropped by an order of magnitude, without affecting the TCR much. As a result, for any given resistivity, we were able to obtain films with a much better TCR by annealing them in nitrogen. Structural analysis by XRD, RBS, Raman, SEM, TEM, and AFM did not reveal any significant changes between the annealed and the unannealed films. Hence the exact mechanisms

contributing to these changes are not understood at this time. It is speculated that the changes taking place are largely at the level of the electronic band spectrum, apparently not detectable by these structural techniques. One hypothesis is that some kind of rearrangement between the amorphous and the nano-crystalline phases, facilitated by annealing, leads to modification of the activation energies associated with conduction, and hence alteration of the conduction mechanisms operating at room temperature.

Ion implantation with H^+ and He^+ caused both the resistivity and TCR of the films to increase, possibly due to amorphization. When the implanted films were subsequently annealed in nitrogen, the resistivity dropped by over an order of magnitude while the TCR still remained high. Here again, the exact reason for the drop in resistivity is not clearly known, and is speculated to be due to some kind of ordering taking place between the amorphous and the nanocrystalline phases. Nevertheless, these TCR resistivity combinations were the best among all films deposited by magnetron sputtering. They were very much comparable to, if not better than, the best TCR values reported in literature.

However, the large change observed upon annealing make these magnetron sputtered films questionable for industrial bolometer applications. As deposited and even after they are annealed, they seem to contain a lot of porosity, and the resistivity and TCR change significantly with annealing. For example, if the films see temperatures anywhere close to 400 °C during subsequent processing or packaging steps, their properties would change dramatically. This might lead to issues associated with the long term stability of the material.

Future work

Though pulsed dc sputtering followed by ion implantation/sputtering has been shown to produce films with excellent TCR/ resistivity combinations, a few unanswered questions still

remain with respect to the processing conditions, microstructure and the electrical transport in these materials. All the experiments performed in this work were done at a fixed total pressure (5 mTorr), fixed target power (300 W) and fixed pulsed frequency (20 kHz). It would be interesting to see how the hysteresis behavior of the target and film properties change when these parameters are varied. For example, a lower pressure would lead to a higher mean free path in the plasma and hence fewer collisions between the atoms/ions, while a lower power would reduce the sputter rate of vanadium atoms, leading to a lower V:O ratio in the plasma and in the film. Changing the pulse duration and frequency would directly affect the rate at which the oxide layer is expelled from the target surface and thus gives us a potential handle to modify the range over which the hysteresis behavior is seen.

Another method to modify the plasma characteristics is by applying an rf or a dc-bias to the substrate during the sputtering process. It would introduce a new dimension to the process, by providing an additional force of attraction for the vanadium ions towards the substrate. At the same time, it could also cause loosely bound deposited material to be sputtered off from the substrate surface, leading to a denser final film. Some preliminary work done by our group shows that we are indeed getting denser films with slightly different microstructure when a bias to the substrate is applied during deposition.

Using an oxide target such as VO_2 or V_2O_3 in combination with pure V target in dual sputtering mode is yet another way to alter the ratio of vanadium to oxygen atoms in the plasma, and thus will provide an extra handle for controlling the film properties. But one needs to carefully evaluate how the presence of an additional target affects the hysteresis behavior of the V-target.

Post-deposition annealing done in this work was limited to oxidizing and inert atmospheres. Annealing in a reducing atmosphere, such as forming gas, might result in completely different trends with respect to the electrical and structural properties of the films, and

is worth investigating. Another issue to look at is the effect of a capping layer on the properties of the film. The industry currently uses a 30 nm silicon dioxide cap sputtered from a quartz target to protect the vanadium oxide layer during further processing steps. How this capping layer would impact the post-deposition processing steps like annealing and ion implantation still needs to be studied.

We have seen that ion implantation with H^+/He^+ followed by annealing has beneficial effects on the TCR and resistivity of the VO_x films for the microbolometer application. This can be taken one step further by implanting with O^- ions. Implantation with oxygen serves a dual purpose. Firstly, oxygen being an active species can modify the effective ratio of vanadium to oxygen in the films and hence the valence state of vanadium, thereby altering the structural and electrical properties of the film. And secondly, it can also increase the extent of amorphization in the films as it is a much heavier atom than hydrogen and helium. In the same line of reasoning, one could also implant vanadium atoms. However, implantation is not a viable industrial technique for modifying the films because of the relative cost of the process. It may, however be a valuable scientific tool to understand the optimal film for IR imaging applications.

A lot of work still needs to be done in order to understand the transport properties in this material. It is still unclear as to which phase (amorphous or nano-crystalline) really dominates the TCR and resistivity of the films, and is there an optimum ratio of these that would give a high TCR with lower resistivity. Though we found that post-deposition processing results in enhanced TCR/resistivity combination, the exact mechanism leading to this effect is not well understood. Further experiments such as detailed optical measurements in the IR region might throw light on the band structure /defect states present in the material, which could then be correlated to the conduction. Measuring the Seebeck coefficient is a useful method to determine the carrier type and concentration, but it may not be easy to make such a measurement in a material like VO_x where both carrier types might be present simultaneously.

An important property of the sensing material which was beyond the scope of this thesis is the materials' $1/f$ noise. It is a critical component to the functioning of the bolometer as it has a direct effect on the sensitivity. The noise of a material depends on its composition, microstructure and electronic band structure. It still remains to be seen how the noise of the sample is affected by annealing and ion implantation. Noise measurement facilities were recently setup up here at Penn State and now have the capability to compare normalized Hooge parameter across different samples. It would be interesting to study and understand the correlation between noise and the TCR and resistivity of these magnetron sputtered films and measurements are currently underway.

REFERENCES

- [1] A. Rogalski, "Infrared Detectors: status and trends", *Progress in Quantum Electronics*, 27 (2003) 59.
- [2] J. Caniou, "Passive Infrared Detection – Theory and Applications", Kluwer Academic Publishers, The Netherlands (1999).
- [3] P. W. Kruse, "Uncooled Thermal Imaging – Arrays, Systems and Applications", *SPIE* (2001).
- [4] A. Rogalski, "Infrared Detectors: an overview", *Infrared Phys. Technol.* 43 (2002) 187.
- [5] R. De Waard and E. M. Wormser, "Description and Properties of Various Thermal Detectors", *Proc. IRE* (1959) Paper 4.1.3.
- [6] R. A. Wood, "Monolithic Silicon Microbolometer Arrays", *Semiconductors and Semimetals* 47 (1997) 43.
- [7] B. Cole, R. Horning, B. Johnson, K. Nguyen, P. W. Kruse, and M. C. Foote, "High Performance Infrared Detector Arrays using thin film microstructures", *IEEE International Symposium on Applications of Ferroelectrics*, (1994) 653.
- [8] J. L. Tissot, "IR detection with uncooled sensors", *Infrared Phys. Technol.* 46 (2004) 147.
- [9] S. Sedky, P. Fiorini, M. Caymax, C. Baert, L. Hermans, and R. Mertens, "Characterization of bolometers based on polycrystalline silicon germanium alloys", *IEEE Electron. Device Lett.* 19 (1998) 376.
- [10] W. Radford, D. Murphy, M. Ray, S. Propst, A. Kennedy, J. Kojiro, J. Woolaway, and K. Soch, "320 x 240 silicon microbolometer uncooled IRFPAs with on-chip offset correction", *Proc. SPIE* 2746 (1996) 82.
- [11] J. B. Goodenough, "Metallic Oxides", *Prog. Solid State Chem.* 5 (1971) 145.
- [12] U. Schwingenschlogl and V. Eyert, *Ann. Phys. (Leipzig)* 13 (2004) 475.
- [13] C. H. Griffiths and H. K. Eastwood, "Influence of stoichiometry on the metal-semiconductor transition in vanadium oxide", *J. Appl. Phys.* 45 (1974) 2201.
- [14] T. Mitsuishi, "On the Phase Transformation of VO_2 ", *Jpn. J. Appl. Phys.* 6 (1967) 1060.
- [15] G. J. Hyland, "On the electronic phase transitions in the lower oxides of vanadium", *J. Phys. C* 2 (1968) 189.

- [16] C. D. Reintsema, "Improved VO₂ microbolometers for infrared imaging: operation on the semiconducting-metallic phase transition with negative electrothermal feedback", SPIE 3698 (1999) 190.
- [17] L. A. L. de Almeida, "Modeling and performance of vanadium-oxide transition edge microbolometers," Appl. Phys. Lett. 85 (2004) 3605.
- [18] M. D. Banus, T. B. Reed, and A. J. Strauss, "Electrical and Magnetic Properties of TiO and VO", Phys. Rev. B 5 (1972) 2775.
- [19] J. B. Goodenough, "Influence of Atomic Vacancies on the Properties of Transition-Metal Oxides – TiO_x and VO_x", Phys. Rev. B 5 (1972) 2764.
- [20] E. N. Fuls, D. H. Hensler, and A. R. Ross, "Reactively sputtered vanadium dioxide thinfilms", Appl. Phys. Lett. 10 (1967) 199.
- [21] G. A. Rozgonyi and D. H. Hensler, "Structural and Electrical Properties of Vanadium Dioxide Thin Films", J. Vac. Sci. Technol. 5 (6) (1968) 194.
- [22] E. Kusano, J. A. Theil, and J. A. Thornton, "Deposition of vanadium oxide films by direct-current magnetron reactive sputtering", J. Vac. Sci. Technol. A 6 (1988) 1663.
- [23] M. Ghanashyam Krishna, Y. Debaugé, and A. K. Bhattacharya, "X-ray photoelectron spectroscopy and spectral transmittance study of stoichiometry in sputtered vanadium oxide films", Thin Solid Films 312 (1998) 116.
- [24] S. D. Hansen, and C. R. Aita, "Low temperature reactive sputter deposition of vanadium oxide", J. Vac. Sci. Technol. A 3 (1985) 660.
- [25] M. Benmoussa, E. Ibnouelghazi, A. Bennouna and E. L. Ameziane, "Structural, electrical and optical properties of sputtered vanadium pentoxide thin films", Thin Solid Films 265 (1995) 22.
- [26] A. Lourenco, A. Gorenstein, S. Passerini, W. H. Smyrl, M. C. A. Fantini, and M. H. Tabacniks, "Radio-Frequency Reactively Sputtered VO_x Thin Films Deposited at Different Oxygen Flows", J. Electrochem. Soc. 145 (2) (1998) 706.
- [27] Y. J. Park, K. S. Ryu, N-G. Park, Y-S. Hong, and S. H. Chang, "RF-Sputtered Vanadium Oxide Films: Effect of Film Thickness on Structural and Electrochemical Properties", J. Electrochem. Soc. 149 (2002) A597.
- [28] E. E. Chain, "The influence of deposition temperature on the structure and optical properties of vanadium oxide films", J. Vac. Sci. Technol. A 4 (1986) 432.
- [29] E. E. Chain, "Effects of oxygen in Ion-beam sputter deposition of vanadium oxide", J. Vac. Sci. Technol. A 5 (1987) 1836.

- [30] S. B. Wang, S. B. Zhou, X. J. Yi, "Preparation of homogeneous VO_x thin films by ion beam sputtering and annealing process", *Vacuum* 75 (2004) 85.
- [31] C. V. Ramana, O. M. Hussain, B. S. Naidu, and P. J. Reddy, "Spectroscopic characterization of electron-beam evaporated V₂O₅ thin films", *Thin Solid Films* 305 (1997) 219.
- [32] A. D. Rata, A. R. Chezan, C. Presura and T. Hibma, "Electrical properties of epitaxially grown VO_x thin films", *Surface Science* 532 (2003) 341.
- [33] D. P. Partlow, S. R. Gurkovich, K. C. Radford, and L. J. Denes, "Switchable vanadium oxide films by a sol-gel process", *J. Appl. Phys.* 70 (1991) 443.
- [34] R. T. Rajendra Kumar, B. Karunagaran, D. Mangalaraj, Sa. K. Narayanadass, P. Manoravi, M. Joseph, and V. Gopal, "Pulsed laser deposited vanadium oxide thin films for uncooled infrared detectors", *Sensors and Actuators A* 107 (2003) 62.
- [35] J. A. Thornton, "Influence of apparatus geometry and deposition conditions on the structure and topography of thick sputtered coatings", *J. Vac. Sci. Technol.* 11 (1974) 666.
- [36] R. A. Wood, J. Carney, R. E. Higashi, T. Ohnstein, and J. Holmen, "Advances in uncooled silicon monolithic IR 2D arrays", *Proc. IRIS DSG* (1988).
- [37] R. A. Wood and E. Stelzer, "High Density Array Development", Final Report DAAB07-87-C-F024. NVEOD, Fort Belvoir, VA.
- [38] Jerominek, H., Picard, F., and Vincent D., "Vanadium oxide films for optical switching and detection", *Opt. Eng.* 32 (1993) 2092.
- [39] C-K. Chung, L-H. Wu, T-S Lee, "Fabrication of thin film vanadium oxide for microbolometer", *International Journal of Nonlinear Sciences and Numerical Simulation* 3 (2002) 299.
- [40] Y-H. Han, I-H. Choi, H-K. Kang, J.Y. Park, K-T. Kim, H-J. Shin and S. Moon, "Fabrication of vanadium oxide thin film with high temperature coefficient of resistance using V₂O₅/V/V₂O₅ multi-layers for uncooled microbolometers", *Thin Solid Films* 425 (2003) 260.
- [41] S. Chen, H. Ma, S. Wang, N. Shen, J. Xiao, H. Zhou, X. Zhao, Y. Li and X. Yi, "Vanadium oxide thin films deposited on silicon dioxide buffer layers by magnetron sputtering", *Thin Solid Films* 497 (2006) 267.
- [42] Y. Lv, M. Hu, M. Wu and Z. Liu, "Preparation of vanadium oxide thin films with high temperature coefficient of resistance by facing targets d.c. reactive sputtering and annealing process", *Surface Coat. Technol.* 201 (2007) 4969.

- [43] H. Wang, X. Yi, S. Chen, S. He, and X. Fu, "Reactive Ion Beam Sputtering of Vanadium Oxides Films for Uncooled Microbolometer", *International Journal of Infrared and Millimeter Waves* 26 (2005) 421.
- [44] A. D. Rata, A. R. Chezan, M. W. Haverkort, H. H. Hsieh, H.-J. Lin, C. T. Chen, L. H. Tjeng and T. Hibma, "Growth and properties of strained VO_x thin films with controlled stoichiometry", *Physical Review B* 69 (2004) 075404.
- [45] Y-H. Han, K-T. Kim, H-J. Shin and S. Moon, "Enhanced characteristics of an uncooled microbolometer using vanadium-tungsten oxide as a thermometric material", *Appl. Phys. Lett.* 86 (2005) 254101.
- [46] K. Sarakinos, J. Alami, C. Klever, and M. Wutting, "Process stabilization and enhancement of deposition rate during reactive high power pulsed magnetron sputtering of zirconium oxide", *Surf. Coat. Technol.* 202 (2008) 5033.
- [47] J. D. Petrilli, "Pulsed dc sputtering of vanadium oxide thin films", B. S. Thesis (2006).
- [48] N. Fieldhouse, "Vanadium Oxide Films Produced Through Pulsed DC Sputtering for Infrared Sensor Applications", B. S. Thesis (2007).
- [49] K. E. Wells, "Properties of pulsed DC sputtered vanadium oxide thin films using a V₂O₃ target for uncooled microbolometers", M. S. Thesis (2008).
- [50] N. J. Podraza, "Optical Properties of Nanocrystalline Vanadium Oxide Thin Films as Determined by Spectroscopic Ellipsometry", MURI Review Meeting (2008).
- [51] C. Venkatasubramanian, M. W. Horn and S. Ashok, "Ion implantation studies on VO_x films prepared by pulsed dc reactive sputtering", *Nucl. Instrum. and Methods Phys. Res. B* 267 (2009) 1476.
- [52] C. Venkatasubramanian, O. M. Cabarcos, D. L. Allara, M. W. Horn, and S. Ashok, "Correlation of temperature response and structure of annealed VO_x thin films for IR detector applications", *J. Vac. Sci. Technol. A* 27 (2009) 956.
- [53] N. Fieldhouse, S. M. Pursel, M. W. Horn and S. S. N. Bharadwaja, "Electrical properties of vanadium oxide thin films for bolometer applications: processed by pulse dc sputtering", *J. Phys. D* 42 (2009) 055408.
- [54] N. Fieldhouse, S. M. Pursel, R. Carey, M. W. Horn and S. S. N. Bharadwaja, "Vanadium oxide thin films for bolometric applications deposited by reactive pulsed dc sputtering", *J. Vac. Sci. Technol. A* 27 (2009) 951.
- [55] B. D. Gauntt, E. C. Dickey, and M. W. Horn, "Stoichiometry and microstructural effects on electrical conduction in pulsed dc sputtered vanadium oxide thin films", *J. Mater. Res.* 24 (2009) 1590.

- [56] S. S. N. Bharadwaja, C. Venkatasubramanian, N. Fieldhouse, S. Ashok, M. W. Horn, and T. N. Jackson, "Low temperature charge carrier hopping transport mechanism in vanadium oxide thin films grown using pulsed dc sputtering" *Appl. Phys. Lett.* 94 (2009) 222110.
- [57] E. V. Barnat and T-M. Lu, "Pulsed and Pulsed Bias Sputtering Principles and Applications", Kluwer Academic Publishers, Massachusetts, USA (2003).
- [58] J. A. Theil, E. Kusano, and A. Rockett, "Vanadium reactive magnetron sputtering in mixed Ar/O₂ discharges", *Thin Solid Films* 298 (1997) 122.
- [59] S. Berg and T. Nyberg, "Fundamental understanding and modeling of reactive sputtering processes", *Thin Solid Films* 476 (2005) 215.
- [60] R. A. Vaia, M. S. Weathers and W. A. Bassett, "Anomalous peaks in grazing incidence thin film X-ray diffraction", *Powder Diffraction* 9 (1994) 44.
- [61] M. Birkholz, "Exercises and Solutions of Thin Film Analysis by X-ray Scattering", Wiley-VCH, Weinheim (2006).
- [62] S. D. Jackson, P. C. Stair, L. F. Gladden, and J. McGregor, "Alkane Dehydrogenation over Vanadium and Chromium Oxides in *Metal Oxide Catalysis* ; Edited by S. David Jackson, Justin S. J. Hargreaves; Vol. 2", Wiley-VCH:Germany (2009).
- [63] O. M. Cabarcos, B. D. Gauntt, E. C. Dickey, D. L. Allara and M. W. Horn, unpublished results.
- [64] W. Meyer and H. Z. Neldel, *Tech. Phys.* 12 (1937) 588.
- [65] T. A. Abtew, M. Zhang, Y. Pan, D. A. Drabold, "Electrical conductivity and Meyer–Neldel rule: The role of localized states in hydrogenated amorphous silicon", *J. Non-Cryst. Solids* 354 (2008) 2909.
- [66] H. Overhof and P. Thomas, "The Statistical Shift Model for the Meyer-Neldel Rule", *Def. Diff. Forum* 192-193 (2001) 1.
- [67] S. K. Ram, S. Kumar, and P. Roca I Cabarrocas, "Normal and anti Meyer–Neldel rule in conductivity of highly crystallized undoped microcrystalline silicon films", *J. Non-Cryst. Solids* 354 (2008) 2263.
- [68] F. Abdel-Wahab and K. Shimakawa, "The Meyer-Neldel rule in non-metallic YBa₂Cu₃O_y films", *Philos. Mag. Lett.* 77 (3) (1998) 159.
- [69] J. Hubert, et al., "Micromachined uncooled VO₂-based IR bolometer arrays", *Proc. SPIE*, 2746 (1996) 60.
- [70] Y. Zhou, Z. Qiu, M. Lü, A. Zhang, and Q. Ma, "Preparation and characterization of V₂O₅ macro-plates", *Materials Letters* 61 (2007) 4073.

- [71] J. Li, B. D. Gauntt, and E. C. Dickey, "Microtwinning in highly nonstoichiometric VO_x thin films", *Acta Materialia* 58 (2010) 5009.
- [72] B. I. Shklovskii and A. L. Efros, "Electronic properties of Doped Semiconductors", Springer-Verlag, Berlin (1984).
- [73] N. F. Mott, *Phil. Mag.* 19 (1969) 835.
- [74] R. M. Hill, "Variable-Range Hopping", *Phys. Status Solidi A* 35 (1976) K29.
- [75] A. G. Zabrodskii, *Sov. Phys. Semicond.* 11 (1977) 345.
- [76] P.D. Townsend, J. C. Kelly, and N. E. W. Hartley, "Ion Implantation, Sputtering and their Applications", Academic Press, New York (1976).

VITA

Chandrasekaran Venkatasubramanian

Chandrasekaran Venkatasubramanian was born January 21, 1983 in Chennai, India. He graduated from the Indian Institute of Technology (IIT), Madras with a bachelors degree in Metallurgical and Materials Engineering in July 2004. Following his bachelor's degree, he entered the Doctoral program in Engineering Science and Mechanics at The Pennsylvania State University. His research work focused on the preparation and characterization of the sensor material used for infrared imaging.